DEVELOPMENT AND EVALUATION OF 3D-PRINTED CARDIOVASCULAR STENTS

A DISSERTATION IN
Pharmaceutical Sciences
and
Chemistry

Presented to the Faculty of the University of Missouri-Kansas City
in partial fulfillment of the requirements
for the degree of

DOCTOR OF PHILOSOPHY

by

HARI MANI KRISHNA VEERUBHOTLA

M.Sc. in Pharmaceutics (Distinction)
Rhodes University, Grahamstown, South Africa, 2016

Kansas City, Missouri
2022

DEVELOPMENT AND EVALUATION OF 3D-PRINTED CARDIOVASCULAR STENTS

Hari Mani Krishna Veerubhotla, Candidate for the Doctor of Philosophy Degree

University of Missouri-Kansas City, 2022

ABSTRACT

Biodegradable stents (BDS) could be a promising alternative to the conventional metallic stents for the treatment of atherosclerosis which is a coronary artery disease (CAD). Three-dimensional (3D) printing technique has offered easy and fast fabrication of BDS with enhanced reproducibility and efficacy. Therefore, the main aim of the current study was to develop 3D-printed biodegradable cardiovascular stents. A combination of 2-hydroxy ethyl methacrylate (HEMA) and methacrylate graphene oxide (MeGO) was used to enhance the mechanical properties and loaded with resveratrol (RSL) to efficiently recover endothelial cell function. The biocompatibility of the 3D-printed stent was evaluated using *in vitro* cell culture studies and zebrafish embryo model.

The percentage changes in volume of stents fabricated using HEMA and HEMA-0.35MeGO were 36.7±4.7% and 7.7±1.6%, respectively after 24 hr. The remaining fractions of 3D stents after 21 days and their corresponding first-order degradation rates were 95.9±0.5% and 0.30±0.10 x 10^{-4}/hr for HEMA, and 98.2±0.3% and 0.11±0.04 x 10^{-4}/hr for HEMA-0.35MeGO. The addition of MeGO significantly ($p<0.001$) enhanced the stiffness of hydrogel inks for 3D stents, indicating Young's moduli of 0.22±0.01x10^{-2} MPa and 0.41±0.01x10^{-2} MPa for HEMA and HEMA-0.35MeGO after 21 days. 3-(4,5-dimethylthiazol-2-yl)-5-(3-carboxymethoxyphenyl)-2-(4-sulfophenyl)-2H-tetrazolium (MTS) assay revealed that 3D stents loaded with RSL (~1 mM) exerted no cytotoxic effects on the human umbilical vein endothelial cells (HUVECs). The controlled release of RSL from the stent enhanced nitric

oxide (NO) production, lowered the levels tumor necrosis factor (TNF)-α, and alleviated H_2O_2-induced oxidative stress in HUVECs.

The RSL-loaded 3D stents displayed maximum viability of HUVECs in presence of oxidized low-density lipoprotein (ox-LDL) and resulted in similar NO production like control group (52.8±0.4 μM and 51.9±0.8 μM), whereas lipopolysaccharides (LPS) treatment (10 μg/mL) significantly displayed higher amounts of NO (82.4±1.2 μM). The amounts of TNF-α and interleukin (IL)-β released from zebrafish embryos (1.8±0.8 and 1.9±0.2) in the group treated with the RSL-loaded 3D stents were significantly lower (p<0.001) than those from the LPS alone treated group (8.1±2.3 and 23.8±3.8, respectively). It was found that stents with RSL at a dose of 1 mM indicated no mortality during the developmental stages, but stents at a dose of 2 mM resulted a lowered survival rate (93.3±3.3%), shorter length of larvae, pericardial and yolk sac edemas of 53.3±23.3% and 3.3±3.3%, respectively.

The 3D-printed biodegradable stent based on HEMA-MeGO and loaded with RSL displayed excellent biocompatibility and mechanical properties. RSL released from 3D cardiovascular stents efficiently recovered the endothelial function. The 3D-printed stents with the loading dose of 1 mM RSL displayed good biocompatibility in the zebrafish embryo toxicity studies. The RSL-loaded 3D stents efficiently downregulated the pro-inflammatory cytokines, while producing minimal developmental defects in zebrafish embryos. The RSL-loaded 3D stents displayed good biocompatibility in both Raw 264.7 cells and zebrafish embryo models, guaranteeing acceptable host response in clinical application. Overall, our results demonstrated that RSL-loaded stents protect an organism against oxidative stress, while limiting developmental defects in zebrafish embryos.

APPROVAL PAGE

The faculty listed below, appointed by the Dean of the School of Graduate Studies, have examined a dissertation titled "Development and Evaluation of 3D-Printed Cardiovascular Stents", presented by Hari Mani Krishna Veerubhotla, candidate for the Doctor of Philosophy degree, and certify that in their opinion it is worthy of acceptance.

<u>Supervisory Committee</u>

Chi H. Lee, Ph.D., Committee Chair
Division of Pharmacology and Pharmaceutical Sciences

J. David Van Horn, Ph.D., Co-Discipline Advisor
Department of Chemistry

Kun Cheng Ph.D.
Division of Pharmacology and Pharmaceutical Sciences

Gerald J. Wyckoff Ph.D.
Division of Pharmacology and Pharmaceutical Sciences

Russell B. Melchert Ph.D.
Division of Pharmacology and Pharmaceutical Sciences

CONTENTS

LIST OF ILLUSTRATIONS

xi

LIST OF TABLES

ACKNOWLEDGEMENTS

CHAPTER 1

INTRODUCTON

1.1.Overview

Atherosclerosis is linked to about 50% of the deaths in the western society [1]. In the year 2020, almost 805,000 people suffered from heart attack and 2 in 10 deaths happened in adults in less than 65 years old due to cardiovascular diseases [2]. It is majorly a chronic inflammatory disorder initiated by the deposition of low-density lipoproteins (LDL) in the arteries. The fat build-up leads to narrowing of the arterial wall and production of an inflammatory cascade [3–6]. The reduced blood flow to the downstream muscle cells resulting in heart attacks and is considered a principal reason for atherosclerotic cardiovascular diseases.

1.2. Pathophysiology of Atherosclerosis

The development of an atherosclerotic plaque is initiated by endothelial dysfunction. The elevated levels of cholesterol in the blood are considered one of the major triggers for endothelial damage [7]. Hypercholesterolemia results in modifications of endothelial permeability in the arterial wall, resulting in migration of LDL into arterial wall. The LDL particles can be oxidized in the presence of reactive oxygen species (ROS) such as superoxide, hydroxyl radicals from the surrounding cells [8]. The damaged endothelial cells express vascular adhesion molecule-1 to attract the circulating monocytes which consequently migrate to the sub-endothelial space (intima) through diapedesis [9]. The monocytes become macrophages and begin engulfing the oxidized LDL (ox-LDL) to convert into foam cells. The macrophages generate pro-inflammatory cytokines like tumor necrosis factor (TNF)-α and interleukin (IL)-β for reinforcement to facilitate the uptake of ox-LDL, leading to enhanced

1

levels of cytokines and a positive feedback mechanism is initiated [10]. The excessive formation of lipid-laden foam cells leads to necrosis, resulting the migration of smooth muscle cells (SMCs) to form a fibrous cap. The breakdown of collagen and death of SMCs destabilizes the atherosclerotic plaque, blocking the blood flow that subsequently leads to myocardial infarction as shown in Figure 1 [11,12].
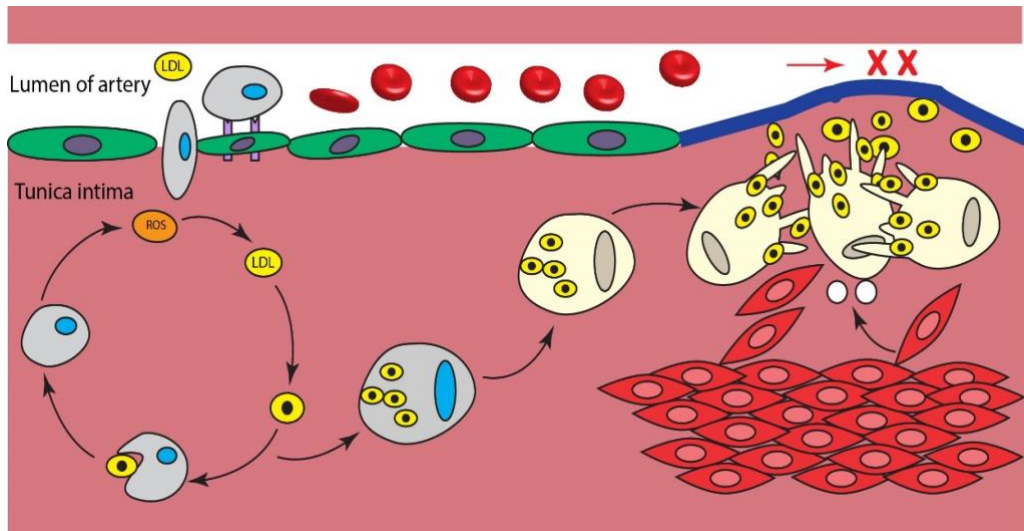
Figure 1. Pathophysiology of atherosclerotic plaque formation.

1.3. Statement of the Problems

Angioplasty with stent placement is routinely the first line of treatment against atherosclerosis. Drug-eluting stents (DES) have significantly enhanced the efficacy of atherosclerosis management due to their immediate action and mid-term safety [13]. Despite all the advancements in DES, there is a considerable risk of delayed endothelization, increasing the chances of mortality up to 30% [14]. Also, the enduring nature of the metallic struts may lead to constrained vessel movement and interference with non-invasive diagnostic techniques. Therefore, a new generation of novel biodegradable stents (BDS) that may reduce the possibility of long-term risks associated with the permanent nature of metallic stents would be an ideal alternative for therapeutic advances in the treatment of atherosclerosis.

Following the first reported successful trial with the biodegradable cardiovascular stent in 1980, several BDS have been under extensive investigation and clinical assessment [15]. The BDS provide sufficient mechanical strength to the damaged endothelium for 6 ~ 9 months and slowly degrade into inactive metabolites that excrete from the body [16]. These BDS typically do not require secondary surgery for their removal and may reduce the risk of in-stent restenosis and thrombosis.

The printability of hydrogels into two (2D) and three-dimensional (3D) structures have been extensively studied in a variety of biomedical applications, such as tissue engineering, organ printing, and cell-laden biological scaffold for regenerative medicine [17]. However, the design of hydrogel structures and printing parameters have not yet been extensively explored. The proposed approach is first of its kind which would be used for the development of cardiovascular stents with extensive studies related to its material safety, design pattern, structural integrity, and cellular responses for anti-proliferative and anti-inflammatory effects.

1.4. Hydrogel-based 3D Printing

The term 3D printing refers to additive manufacturing involving the development of complex structures using a layer-by-layer printing approach [18]. The 3D printing of hydrogels is routinely carried out through stereolithography (SLA), extrusion-based direct ink writing, and digital light processing. The 3D printing ink should possess desirable material properties such as printability, biodegradability, and possibility for surface modification with functional groups [19]. The printability of the ink depends on viscosity of the ink, ability to crosslink, size of the nozzle, and retainability of the 3D structure after printing [20].

The 3D shape stability is affected by rheological properties of the material, especially shear-thinning behavior of the ink in extrusion-based printing [21]. The efficacy of hydrogel inks is dependent on sol-gel transition during the manufacturing process, ensuring a smooth continuous flow of print filament without clogging the nozzle. The mechanical properties of hydrogels are influenced by the material category *i.e.* natural (*e.g.*, alginate) or synthetic (*e.g.*, poly-hydroxyethyl methacrylate) and the method of crosslinking *i.e.*, physical or chemical. The incorporation of tough particles (carbon nanoparticles) in the ink forms a strong hydrogel network with superior physical strength suitable for biomedical applications [22].

The use of 3D bioprinting technology would yield quick and accurate fabrication of structures with reproducibility and ease of manufacture. Considering patients' diseased condition and the size of atherosclerotic plaque, the length of the stent and the amount of drug loading can be tailored [23]. The low cost of 3D bioprinting makes repairs and upgrades of biomedical devices to be affordable. Biomimetic hydrogels produced through extrusion-based bioprinting would be biocompatible and would help produce flexible hydrogel stents with

sufficient mechanical strength that can withstand the dynamic environment of blood vessel.

The novel approach of BDS is introduced to minimize the immune responses and the biological and mechanical risks caused by a permanent implant. This hydrogel-based stent would plausibly limit the endothelial dysfunction, thus eliminating the occurrence of very late in-stent restenosis. However, the potential application of hydrogels as cardiovascular stents for the treatment of atherosclerosis has been rarely investigated.

1.5. Objectives

A 3D cardiovascular stent based on the hydrogel polymeric materials (alginate and 2-hydroxy ethyl methacrylate) loaded with an anti-oxidant drug, RSL, will be developed to enhance efficiency in recovery of endothelial cell function. A 3D stent model will be printed through the extrusion-based method and corresponding rheological properties of hydrogel inks, and the mechanical properties of 3D-printed stents will be examined.

The effects of drug-eluting stent on cell viability, nitric oxide (NO) production, and downregulation of oxidative stress in the human umbilical vein endothelial cells (HUVECs) will be evaluated using 3-(4,5-dimethylthiazol-2-yl)-5-(3-carboxymethoxyphenyl)-2-(4-sulfophenyl)-2H-tetrazolium (MTS), Griess, and 2', 7'- dichlorofluorescein diacetate (DCFDA) assays, respectively. We believe the controlled release of RSL from the stent would enhance the NO production, lowered TNF-α level, and alleviated H_2O_2-induced oxidative stress in HUVECs.

The objectives of this dissertation are:

1. To evaluate the influence of 3D printing process parameters on the development of hydrogel-based biodegradable stent

2. To develop and characterize RSL-loaded 3D-printed stents that help recover the endothelial cell functions

3. To study ROS scavenging efficacy and potential toxicity of RSL-loaded stents in the mouse macrophage cells and zebrafish model.

CHAPTER 2

PARAMETRIC OPTIMIZATION OF 3D PRINTING PROCESS

2.1. Rationale

In a typical atherosclerosis treatment, the size of the stent is governed by patient-specific variables such as their physiological conditions, age, and the size of the plaque [24]. A personalized stent would be ideal for healing the damaged endothelium and providing effective therapy for patient-specific needs [25,26]. 3D printing devices have served as efficient means to generate biomimetic organs or biological tissues [27]. The application of 3D bioprinting in the treatment of cardiovascular conditions has been well established and exemplified by polymeric cardiovascular stent [28,29], heart valves [30–32] and structural cardiac surgery in CAD [33]. When compared with traditional metallic stents, 3D printing can offer rapid and reproducible production of complex biological models [34].

The major obstacle encountered while using 3D printing in the cardiovascular field is to attain uniform dispersion of the active ingredient (*i.e.,* drug moiety) in the polymeric filament. In addition, during the 3D printing process, the extrusion of filament at high temperatures may cause degradation of the active ingredient and pose a significant risk of polymorph formation. Also, the choice of printable polymeric material having a suitable viscosity for the manufacture of cardiovascular stents is quite limited [35,36]. Naturally derived hydrogels are more advantageous than synthetic polymers due to their extracellular matrix with sufficient mechanical properties [37]. As hydrogels facilitate the printing of tailored scaffold structures at low temperatures [23,38], several studies have reported the 3D printability of hydrogel for biomedical applications including man-made biomimetic fibrillar hydrogels [39], the composition of bio-ink [40], reproducible printed structures [41], and

8

different fabrication techniques [42].

In order to improve the printability and mechanical properties of hydrogels, various approaches including adding functional end groups, using sliding crosslinks, and incorporating nanocomposites or microparticles, have been proposed and evaluated. A study reported exploration of a nano-composite hybrid with cysteine to reinforce the hydrogel system for optimal rheological properties. Cysteine, as an amino acid, naturally existing within biological systems, thus mimicking biological constructs and maintaining biocompatibility [43].

Alginate is known for its biocompatibility and biodegradation properties and has been widely applied to the biomedical fields including wound healing and tissue engineering [44]. Alginate belongs to the class of polysaccharides and is commercially available as the sodium salt of alginic acid composed of D-mannuronic acid and L-guluronic acid [45]. Sodium alginate (SA) forms ionic crosslinking upon exposure to the divalent cations [46]. In one of the studies, modified SA displayed its robust mechanical strength against the continuous, perfused fluid that mimicked the dynamic environment of the myocardium [43].

The storage modulus of 3D printable hydrogels can be regulated through reversible thiol–disulfide exchange within alginate hydrogel hybrid with cysteine that would allow for smooth extrusion and avoid blockage of nozzles during extrusion-based 3D printing process [47]. The modification of polymers with varying amounts of thiol content led to changes in shear modulus of hydrogel constructs including improved mucoadhesiveness, swelling ratio, and gelling properties [48,49].

The fibrous nature of nanofiber promotes the stiffness and other relevant dynamic requirements in the 3D-printed scaffolds. The latest investigations also demonstrated the numerous potential advantages of PLA-based nanofibers over chitosan- and collagen-based

nanofibers in enhancing the mechanical properties of hydrogels [50]. Therefore, the modification of alginate hydrogel with cysteine hybrid and PLA-nanofibers can lead to enhanced swelling ratio, biocompatibility, and biodegradability. This study aimed to evaluate the effects of manufacturing parameters involved with extrusion-based 3D printing of hydrogel-based stents, such as hydrogel's viscosity, printing distance, printing speed, and the nozzle size.

2.2. Materials and Methods

Materials

Sodium alginate (SA), 1-Ethyl-3-(3-dimethylaminopropyl) carbodiimide (EDC), cysteine hydrochloride monohydrate, Isopropyl alcohol (IPA), and resazurin were purchased from Sigma-Aldrich® (St. Louis, MO). Poly (L-lactic acid) with molecular weight (MW) of 140,000-160,000 Da was obtained from Polysciences® Inc. (Warrington, PA). Hexafluoro-2-propanol (HFIP) purchased from TCI® America, Inc. (Portland, OR). All reagents and solvents were of analytical grade.

Synthesis of Cysteine Conjugated Alginate

Cysteine conjugated alginate hydrogel inks were prepared as previously reported [43]. In brief, 200 mg of sodium alginate were dissolved in deionized (DI) water at 37 °C to form a clear solution. EDC (~383.4 mg) was added to the solution and incubated for 1 hr. Cysteine hydrochloride (100 mg) was added to the solution and kept overnight at room temperature under dark conditions. The solution mixture was purified using a dialysis membrane of 3500 molecular weight cutoff (MWCO) in 0.001 M HCl, followed by 1 % NaCl solution for 48 hr.

The final hydrogel solution was freeze-dried and kept at -20 °C for future usage.

Preparation of Poly-Lactic Acid (PLA) Nanofibers

The electrospinning technique was used to prepare PLA-nanofibers [43]. Briefly, 15%w/v PLA was dissolved in HFIP solvent. The mixture solution was loaded into a 5 mL syringe connected to a positive terminal (15 kV) and dispersed on a rotating cylinder with negative potential (-2.5 kV) with two systems separated by 12 cm distance. The nanofibers were electrospun at 0.5 mL/hr and kept in a vacuum dryer for 7 days to remove the solvent.

Preparation and Optimization of Hydrogel Inks

For hydrogel ink preparation, 10%w/v solution of SA powder in DI water at 37 °C was continuously stirred using a magnetic stirrer to form a homogenous hydrogel solution. Then, the freeze-dried alginate-cysteine sample was dissolved in DI water under dark and stirred steadily to obtain a 10%w/v clear solution. The solution was kept at room temperature overnight to eliminate any air bubbles. For the nanofiber hydrogel ink, 0.4%w/v of PLA-nanofibers were added to 10%w/v alginate-cysteine hydrogel solution and mixed gently. 3D structures were printed via layer-by-layer printing, as shown in the schematic presentation (Figure 2). Both alginate and modified alginate structures were printed directly onto a petri dish. A microscopic examination of the printed structures was performed to optimize the printing parameters for the 3D-printed hydrogel stents.
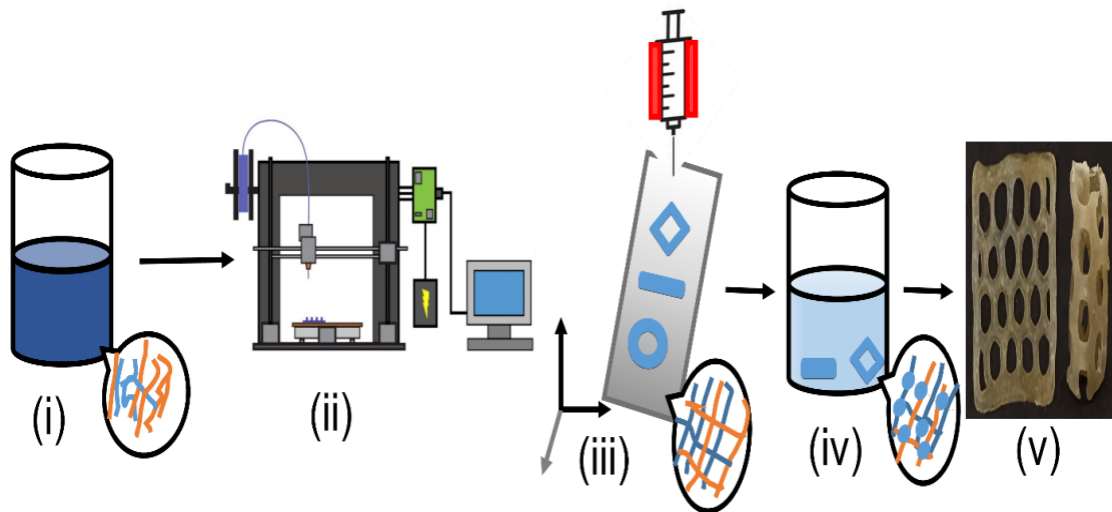
Figure 2. (i) Sodium alginate solution, (ii) Rate controlled extrusion of hydrogel ink using a syringe barrel equipped with an in-built software, (iii) Printing of 3D structures on a cooled platform using a heat jacketed syringe, (vi) Crosslinking of the 3D-printed stent layers using 2.5%w/v CaCl$_2$, and (v) Rolling stent layers into a cylindrical shape using a metallic rod.

Rheological Properties of Hydrogels

The rheological studies of alginate hydrogels were performed using Discovery Hybrid Rheometer (DHR3) (TA Instruments) with parallel-plate geometry (diameter 20 mm, gap 1 mm). The samples were equilibrated between the plates for 60 sec before the start of each experiment. Linear viscoelastic region (LVR) was determined by amplitude sweep study from 0.1 to 10 mN.m at a frequency of 1 Hz. A strain of 10% was selected from LVR, frequency sweeps were conducted with an angular frequency range of 0.1 to 100 rad/sec. The viscosity recovery studies were performed for 130 sec in three stages. During stage I, a shear rate of 0.1/sec was applied for 60 sec, followed by a high shear rate of 100/sec for 10 sec at stage II, and a low shear rate of 0.1/sec for 60 sec at stage III [51]. All measurements were performed thrice at 25 °C and shear viscosity was determined at a shear rate of 0.01 to 100/sec.

Optimizing Conditions of 3D Printing Process

Extrusion-based 3D printing is considered to be the most comprehensive and useful technique for bioprinting. As shown in the scheme of printing procedure (Figure 3), the stents were fabricated using a commercial 3D printer (Tissue Scribe®, 3D cultures, Delaware). TinkerCad® software was used to design the 3D mesh-like layer (10 x10 mm) to replicate the strut of the stent. The generated stereolithography (STL) files (.stl format) were sliced using the Cura® converter program to obtain a G-code file, which was then programmed to the 3D printer to produce the hydrogel ink-based stents.
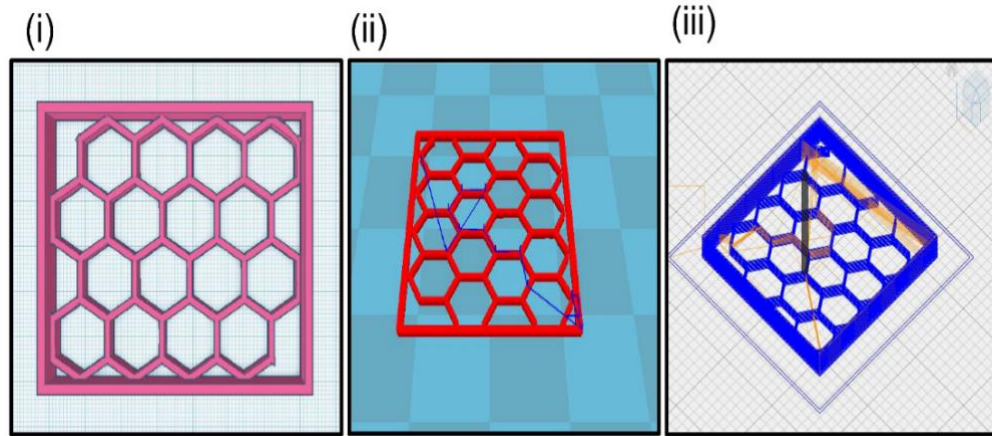
Figure 3. i) Design of the stent struts in TinkerCad®, (ii) Slicing the 3D model (.stl file) in Cura® program, (iii) Pre-examination of G-code on NC viewer v1.1.3.

Becton Dickinson (BD) syringe was loaded with the hydrogel inks (~5 mL) and subsequently stored in the extrusion cavity. Three types of the formulations were printed by varying the composition of hydrogels (10%w/v sodium alginate (SA), 10%w/v cysteine-sodium alginate (SA-CYS), and 10%w/v cysteine-sodium alginate with 0.4%w/v PLA-nanofibers (SA-CYS-NF)) using a 22G print head nozzle of 0.41 mm diameter attached to the syringe. The piston was moved downwards, and ink was extruded through the nozzle, which was 0.33 mm above the fixed printer bed of 120x120 mm area.

Two layers of mesh lattices were 3D printed with 5 mm/sec speed and 100% infill density. The syringe inside the extruder was heated up to 37 °C, and the collector plate was kept at a lower temperature for solidification of the printed structure. After solidification, the gel was crosslinked with 5%w/v $CaCl_2$ for 12 hr. The obtained structure was washed with 0.01 M phosphate-buffered saline (PBS) pH 7.4. A cylindrical tube-like stent was obtained by rotating the mesh like stent layer around the metallic rod of 10 mm length and 0.15 mm outer diameter. Later, the hollow hydrogel structures were dried under vacuum for 4 hr and stored for future use. 3D-printed stents were further characterized for their mechanical strength, morphology, and biodegradability.

Assessment of Swelling Ratios

The initial weight of vacuum-dried stent (S_o) was recorded, and the stent was immersed in 0.01 M PBS pH 7.4 at room temperature for 72 hr. At pre-determined time intervals, the swelled stent (S_1) weight was measured after gentle removal of the surface water using Kim-wipes. The swelling ratios were calculated using the following equation:

$$\text{Swelling ratio }(\%) = \frac{S_1 - S_o}{S_o} * 100 \qquad (1)$$

Study the Surface morphology of 3D Stents

Scanning Electron Microscopy (SEM) was performed to study the surface morphology of 3D stents. The mesh-like stent was cut into rectangular strips, loaded onto a carbon stub, and coated with gold-palladium under vacuum for 15 min using a sputter-coater (Leica® EM SCD050, USA). The coated samples were then visualized using a Field-Emission Environmental SEM Philips XL30 (Leica®, USA) at a voltage of 5 kV.

Assessment of Mechanical Strength

The mechanical strength of stents against the shear stress stemming from the blood flow was tested using an in-house perfusion chamber. Each stent was placed in a Tygon® tube that was perfused with 2% fetal bovine serum (FBS) at a flow rate of 60 mL/min using a peristaltic pump (Mini-pump variable flow, Fisher Scientific®, Waltham, MA). At pre-determined time intervals, the weight of the stent was measured, and the percentage changes in the weight were calculated based on the difference between initial weight (W_o) and final weight (W_1) of the stent.

$$\text{Weight change} (\%) = \frac{W_1 - W_o}{W_o} * 100 \qquad (2)$$

Assessment of the Degradation Rate of 3D Stents

In vitro degradation rates of stents were examined in 0.01 M PBS pH 7.4 at 37 °C. The stents were individually placed in a Tygon® tube that was perfused with buffer solution at 60 mL/min. At pre-determined time intervals, the stent was taken out and dried completely and weighed. The percentage changes in the weight were calculated as described in Equation 2.

The degradation rates were measured by fitting the following linear regression equation [52]

$$\left(\frac{F_t}{F_o}\right)^{\frac{1}{2}} = 1 - k_d.t \tag{3}$$

F_t and F_o are the fraction of remaining weight of hydrogel at time t and initial time point, respectively, and K_d is first-order degradation constant.

Statistical Analysis

All experiments were carried out in triplicate and expressed as mean±SEM. For multiple-group comparisons, one-way analysis of variance (ANOVA) followed by Tukey's HSD analysis was performed. All statistical analyses were carried out using SPSS® software (IBM® Corp. Armonk, NY). p-values represent different levels of significance: *$p < 0.05$, **$p < 0.01$, and ***$p < 0.001$.

2.3. Results and Discussion

Optimization of Loading Volume and Rheology of Alginate Hydrogel

The concentration of alginate in the hydrogel is an integral factor for optimizing the fluidity and/or rigidity of 3D printing ink that can be measured through microscopic images. The spreadability of the hydrogel, its ability to remain on the printer bed, and the thickness of the printed material was affected by the concentration of alginate. When selecting the optimal amounts for the overall research design, we assessed the viscosity as well as swelling ratios of the hydrogel formulations in three aspects: 1) 3D manufacturing process (the rate of release from the nozzle and 3D figure production), 2) stability of the resultant formulation *i.e.*, 3D cardiovascular stent, and 3) biodegradability of the formulation. Due to the three-stage assessment process, the selection of the optimized dose requires multi-step experimental

17

designs.

The hydrogel formulated using 10%w/v SA and 0.4%w/v PLA-nanofibers (SA-CYS-NF) was chosen based on the favorable outcomes of the 3D printing processes and formulation assessment. It was also demonstrated from our previous work [43] that the engineered hydrogels (*i.e.* hydrogels composed of 0.4%w/v nanofibers) had requisite mechanical properties and long-term biocompatibility. It was revealed that alginate hydrogels displayed shear-thinning flow behavior (*i.e.*, non-Newtonian fluid) where its viscosity is linearly correlated with the shear rate of 0.01-100/sec (Figure 4).

At a constant shear rate, SA hydrogel showed higher viscosity than SA-CYS and SA-CYS-NF. The modification of SA with cysteine and the addition of nanofibers further influenced the viscosity of the hydrogel at lower shear rates. This finding could be attributed to several factors, such as poly-electrolytic nature, rigid intramolecular and intermolecular hydrogen network, and changes in cohesiveness, affecting the polymer volume [53] and high molar mass polymer chains [54].

As thiolated sodium alginate tend to form disulfide bonds with two thiol groups, SA-CYS exhibited sol-gel transitional viscous behavior under varied shear stress. In the FTIR spectra (Figure 5), the characteristic peak for thiol group at 2551 cm^{-1} in L-cysteine sample was not detected from SA-CYS sample, verifying the presence of disulfide bonds.
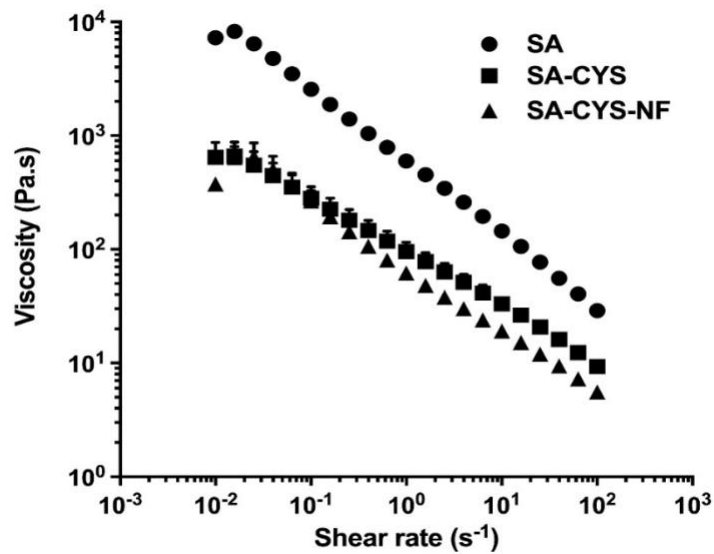
Figure 4. A plot of viscosity versus. shear rate, depicting non-Newtonian fluid (shear thinning) behavior of hydrogel inks.
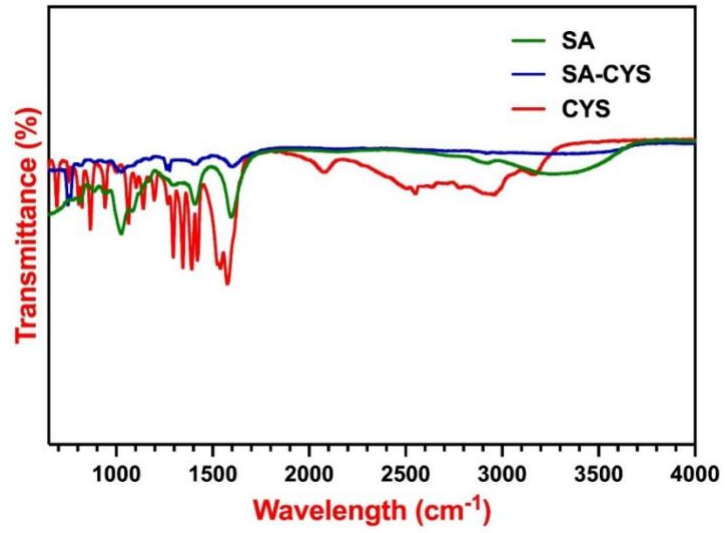
Figure 5. FTIR spectra for hydrogel composites sodium alginate (SA), cysteine (CYS), and cysteine conjugated alginate (SA-CYS).

The content of free amino groups in the SA-CYS indicates the presence of unreacted cysteine not separated from the polymer during dialysis with the low value, implying that free cysteine was nearly absent from the lyophilized polymer [55]. The presence of negligible amount of remaining primary amino groups and numerous thiol moieties is evidence of formation of amide bonds between alginate and cysteine.

The potential self-condensation of cysteine can be further avoided by designing the order of addition for carbonyls with no α-hydrogen atoms. The relationship between nanofiber adsorbent and functional performance was closely related to the composition and chemistry of polymers (*i.e.*, for the polymer stent) or heavy metals (*i.e.*, for the metal stent) [43,56].

Due to advanced merits such as the simplicity of the process, renewable sources, ease of availability, and the additional favorable properties including the fiber size, relative non-toxicity, and biodegradability, a thermoplastic aliphatic polyester, polylactic acid (PLA), has been widely explored as a fabrication base for nanofibers [57–59]. PLA has functional groups, such as –OH and –CH in its chain, which make it feasible to chemically bind with amine groups (*i.e.*, aminolyzed-dispersing hydrogels) in addition to other groups such as maleic and succinic anhydrides, oxazoline and epoxide [60].
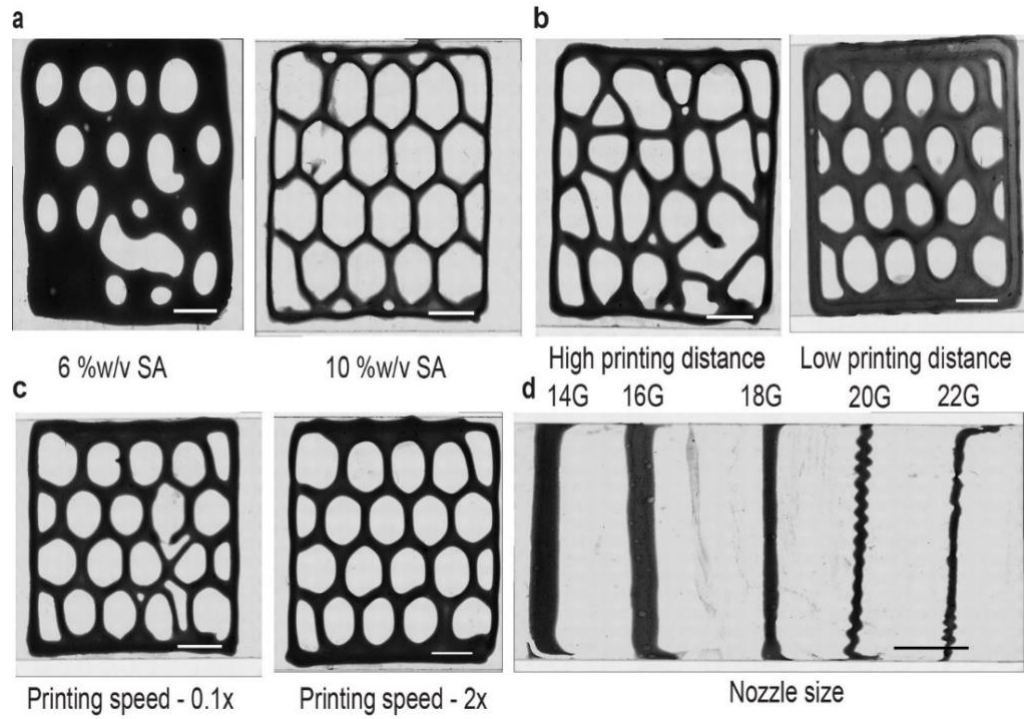
Figure 6. Optical microscopic images depicting changes in stent layers produced by varying material and process parameters; (a) 6%w/v SA and 10%w/v SA, (b) Printing distance above and below 0.33 mm, (c) High (50 mm/sec) and low (2.5 mm/sec) printing speeds, (d) Different nozzle sizes yielding varying thickness (scale bar indicates 5 mm).

The molecular arrangement of material varied with respect to the oscillation speed and direction of the plate rotation. An increase in the shear rate leads to a decrease in the viscosity due to the temporary destruction of the molecular structure [61]. The higher the viscosity of alginate, the stronger it resists spreading when printed on the substrate. As shown in Figure 6a, 3D-printed structure containing 6%w/v alginate hydrogel spreads out, whereas those containing a higher concentration (10%w/v) of alginate produced a uniform strut structure. The non-Newtonian fluid behavior could be quantified using the power-law equation:

$$\eta = K \, \dot{\gamma}^{\,1-n} \qquad\qquad (4)$$

where η is viscosity, K is consistency index, $\dot{\gamma}$ is a shear rate, and n is the power-law index.

The power-law or rate index (n), demonstrates the flow behavior of the fluid, where n>1 denotes shear-thickening, n<1 indicates shear-thinning, and n=1 shows a Newtonian behavior. The alginate hydrogels showed n-value of 0.34±0.01 for SA, 0.48±0.01 for SA-CYS, and 0.46±0.02 for SA-CYS-NF. The results of rate-index confirmed the shear-thinning behavior of pure and modified alginate hydrogel samples. The slight decrease in the rate index values could correspond to the lowering of the viscosity values of 632.4±40.8 pascal-second (Pa·s) of SA, 108.8±21.6 Pa·s of SA-CYS and 66.0±2.0 Pa·s of SA-CYS-NF, at low shear rates.

The viscosity recovery studies showed that SA ink recovered its viscosity value to 62.4±6.2% of initial value, SA-CYS to 80.3±8.9% and SA-CYS-NF to 77.8±7.7% in 10 sec as shown in Figures 7a, 7b, and 7c. The viscosity recovery studies simulate the 3D printing process, by applying a low shear rate (0.1/sec) for 60 sec, representing the ink in syringe cartridge, a high shear rate (100/sec) for 10 sec, mimicking the ink passing through a narrow nozzle, and a low shear rate for 60 sec, exhibiting the recovery stage. The modified alginate

hydrogel (SA-CYS and SA-CYS-NF) achieved greater than 75% of initial viscosity recovery within 10 sec after experiencing a high shear rate, satisfying the printability conditions. As the ink passes through the extrusion stage, the reduced viscosity of hydrogel material may prevent the clogging of the nozzle and help recover its original stability and maintain the 3D-printed structure before crosslinking.

The frequency sweep plots as shown in Figures 8a, 8b, and 8c display the storage and loss modulus as a function of angular frequency in the range of 100 to 0.1 rad/sec. In the pure alginate hydrogels, elastic modulus is dominated property (G'>G") than the viscous modulus throughout the studied range. However, in SA-CYS and SA-CYS-NF hydrogels, the particles were strongly associated with loss modulus (G'<G") at low frequency, while storage modulus (G'>G") dominated at a higher frequency.

As previously stated, SA-CYS and SA-CYS-NF exhibited sol-gel transition via disulfide bond formation. When G" (the loss modulus) becomes larger than G' (the storage modulus representing the elastic solid like behaviour), the applied mechanical force overtakes the molecular or inter particles forces and the material starts to yield (or flow) (*i.e.*, the crossover). The crossover moduli for SA-CYS and SA-CYS-NF were found to be 354±0.39 Pa and 309±0.51 Pa, respectively.
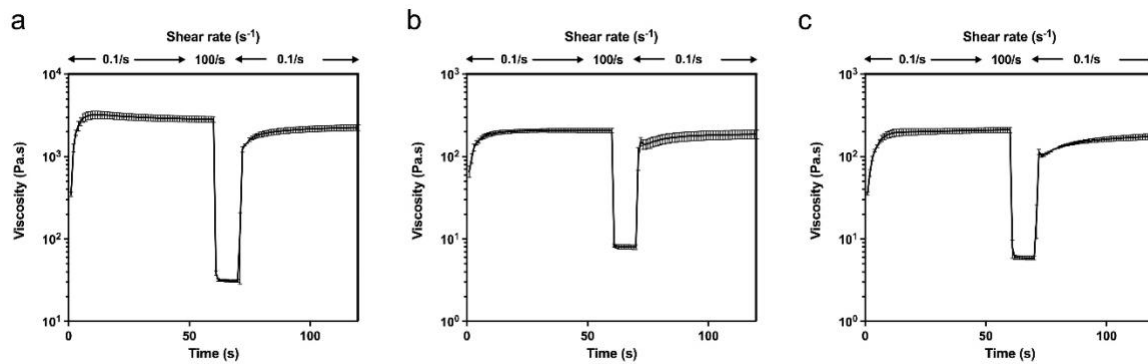
Figure 7. Viscosity recovery and shear rate for (a) SA, (b) SA-CYS, and (c) SA-CYS-NF hydrogel inks as a function of time.
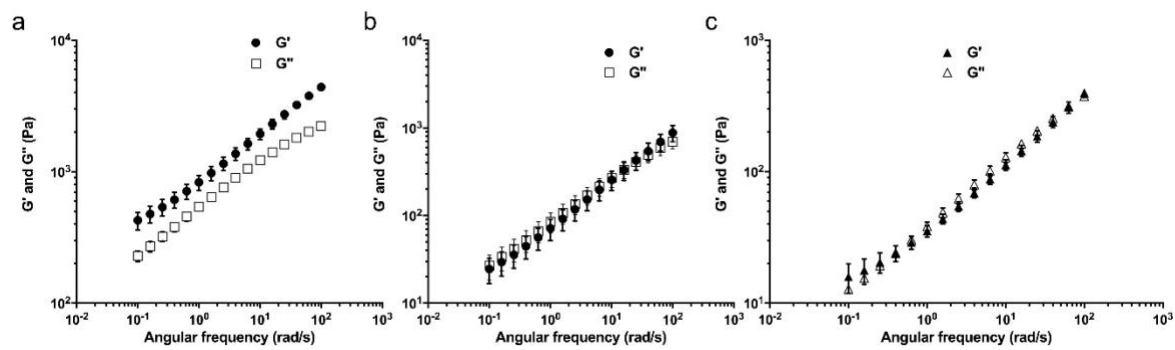
Figure 8. Viscoelastic behavior of hydrogels (a) SA, (b) SA-CYS, and (c) SA-CYS-NF, displaying storage modulus, G', and loss modulus, G'', as a function of angular frequency.

Effects of Printing Distance on Printing Outcomes

The height (z-level) between the nozzle and the printer bed is one of the critical parameters that needs to be optimized for the superior quality of 3D-printed stents. The printed structures may not stay on the bed when the height is too high, whereas reducing the height below the optimum level may lead to structural deformation, as the nozzle disrupts the printed structure and prevent the material from being extruded from the nozzle. When the distance between the nozzle and bed was above 0.33 mm, the hydrogel did not stay on the bed and produced overlapped layers. At lower heights, the nozzle touched the printed structure and compressed it, resulting in grooves and loose structures (Figure 6b).

The auto-bed-leveling was performed to optimize the distance between the printer nozzle and bed. With other parameters being kept constant, such as alginate composition (%), nozzle size, and printing speed, the touch probe technique was carried out to find the optimum height. The syringe with the nozzle was fitted to the extruder cavity to produce a single layer of rectangular mesh on the bed. Based on visual examination of the printed layer, the height was measured and adjusted accordingly. It was observed that maintaining a distance of 0.33 mm between the nozzle and bed during the printing process was necessary to yield the desired 3D structure.

Effects of Printing Speed on 3D-Printed Product

The printing speed is directly related to the combined movement of extruder and printer bed. It has been reported that higher printing speeds may cause inaccurate printed shape, as the increased movement of the syringe-handling and dispensing system influences the printing quality by adversely affecting geometrical precision [62]. In the case of extrusion-based

printing, the force to extrude the material may vary during the process, depending on the mobility of the motion platform [63].

A decrease in the printing speed from 50 to 2.5 mm/sec resulted in thick and loose stent struts, as depicted in Figure 6c. This may be attributable to the fact that excess material deposition happened at the pre-designed sites of the stent during the printing process. At higher printing speeds, the hydrogel spreads out to unintended sites of stent design, forming stretched struts. It was clear that the printing speed is a critical factor in the formation of 3D-printed stents.

Effects of Nozzle Size on 3D-Printed Product

The mechanism of extrusion-based printing is complex to be elucidated due to the presence of numerous critical factors on the process control. The resolution of the printed stent is greatly influenced by the diameter of the printing nozzle. During the process, blocking of nozzle may happen due to the accumulation of material inside the nozzle, leading to poor printability and surface roughness [64]. In addition, small diameter nozzles may be integral due to high extrusion pressure needed to dispense the hydrogel through a narrow orifice. A decrease in the nozzle size could be counterbalanced with the flowability of the hydrogel and loss of the resolution performance [65].

The structures of 3D-printed stents produced by varying nozzle diameters ranging from 0.4 mm to 1.6 mm were characterized for comparison. Larger diameter nozzles yielded wide and rough struts, while the smaller ones caused difficulty in separation and resolution, as represented in Figure 6d. The thickness of the first layer of 3D-printed structure could be the same as that of the nozzle diameter, as previously reported [66]. It was found that the optimum

nozzle diameter was close to that of the printing distance (0.33 mm), as the diameter of the nozzle (0.41 mm) ensured the hydrogel to stay on the printer bed and maintain the layers stacked on top of each other.

Optimization of the 3D Printing Conditions

The conditions used for the 3D printing process were optimized to ensure the production of uniform and reproducible hydrogel-based stents. The alginate concentration of 10%w/v was sufficient to provide the required consistency to the ink which could also stay on the bottom of the plate without losing its structural integrity. The printing speed to maintain the shape of the stents was set at 5 mm/sec and the hydrogel was dispensed using a 22G nozzle placed at 0.33 mm above the platform. The strut thickness of the stents was found to be 339±29 µm, 263±15 µm, and 237±15 µm for SA, SA-CYS, and SA-CYS-NF, respectively.

Assessment of Swelling Ratios

The swelling ratios were calculated by dividing the initial mass with the final mass upon absorption of the surrounding fluid. Most hydrogels contain a 3D network of interconnected pores mostly occupied by the physiological fluids that may cause swelling or shrinking of hydrogels. In the presence of water, alginate hydrogels swell and crosslink with di- or multivalent ionic solutions, forming an integrated network of polysaccharide molecules [67]. An ideal 3D-printed stent should maintain a consistent inner diameter against the constant blood flow, especially at the initial exposure stage that induces not only turbulent blood flow but also an immune response [68]. Thus, the swelling profiles of three types of alginate formulations were evaluated in PBS at room temperature for 72 hr.

As shown in Figure 9a, the swelling ratio of all three types of stents (SA, SA-CYS, and SA-CYS-NF) increased by as much as 20% of the initial ratio within the first 30 min of exposure in PBS. After 1 hr, the swelling ratio of alginate formulations linearly decreased, which could be correlated with the loss of hydrogel mass. The swelling ratios of SA and SA-CYS displayed similar values, $i.e.$, 23.1±2.4% and 22.0±2.4%, respectively, at 30 min, which decreased to 13.7±0.8% and 8.6 ±1.0% at 72 hr. The addition of nanofiber to the alginate stent (SA-CYS-NF) had significantly enhanced the swelling ratio to 38.8±2.9% at 30 min, and slowly reduced to 29.7±3.1% after 72 hr. This could be attributed to the presence of nano-porous networks of nanofibers that can be filled with water [69].

After 6 hr, there were no significant changes in the swelling ratios for both SA and SA-CYS stents. These findings supported that all three types of stents displayed structural integrity, maintaining the volume and diameter, even though SA-CYS-NF had a greater swelling ratio than the other two due to a distinctive porous structural network, as depicted in Figure 9b. These results were in good agreement with the SEM images for all three formulations, as shown in Figure 9c. It was reported that core factors controlling the fluid flow through the nano-porous networks are the large/small features of pore structure as well as their connectivity [70]. The images were generated at higher magnification (8000x), resulting in a square-shaped mass of crosslinked alginate hydrogels. The nano-porous structures were not distinctively visible in the SEM images, suggesting that the distinction between pore bodies could be less influential than connected pore elements in determining the swelling ratios [70].
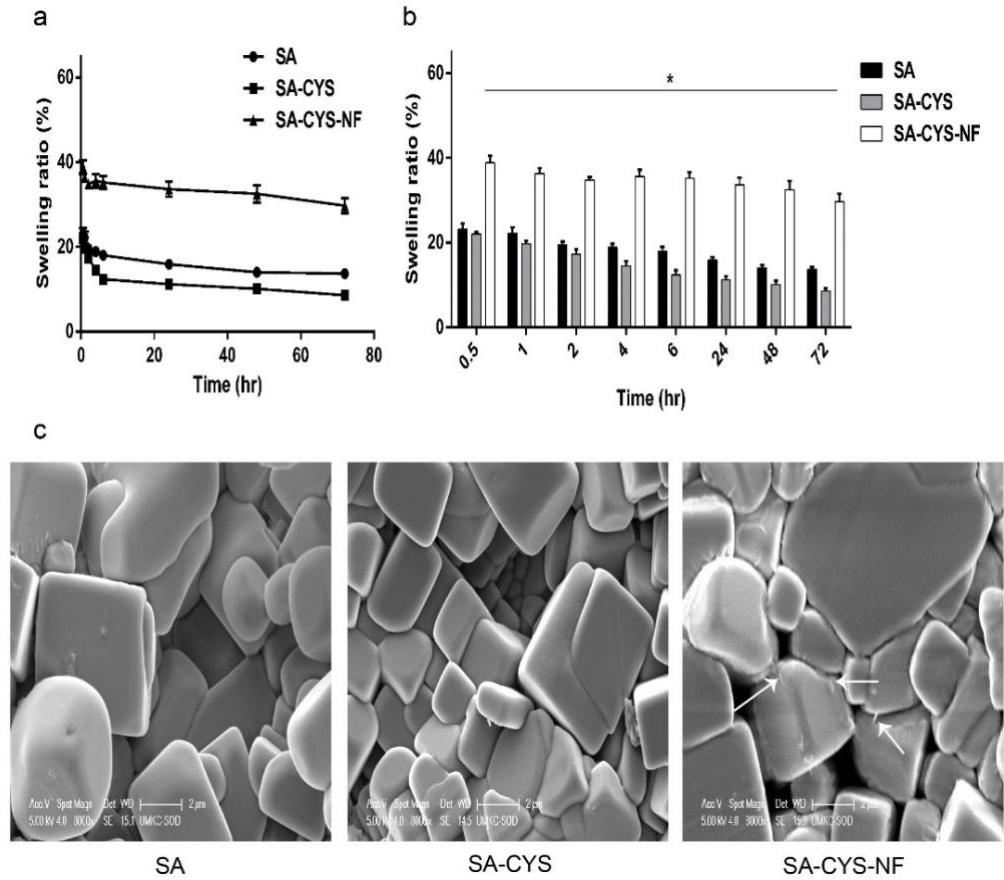
Figure 9. a) The swelling ratio of hydrogel formulations at 72 hr, (b) Percentage swelling ratio versus time, and (c) SEM micrographs for porous structure of SA, SA-CYS, and SA-CYS-NF (arrows highlighting the gaps and spaces in the SA-CYS-NF hydrogels). *$p<0.05$ based on one-way ANOVA followed by Tukey's HSD analysis.

Assessment of the Mechanical Strength

In vitro perfusion studies were performed to determine the mechanical strength and structural integrity of the cardiovascular stents. The wall shear stress (WSS) on the stent, which is a frictional force between endothelium and blood, may cause the changes in its mechanical property and performance [71]. It was previously reported that the mass loss of cardiovascular stent made of poly-L-lactide (PLLA) was closely correlated with the mechanical properties of bioabsorbable PLLA fibers [72]. In this study, the percentage changes in the stent weight were found out to be closely associated with the crosslinking density of polymer and its mechanical behavior.

An in-house perfusion chamber was set-up under the expedited condition to evaluate the mechanical stability against shear stress. As the biodegradability depends on the conditions where the chemical reaction takes place, 3D formulations degrade faster when subjected to factors that accelerate degradation, such as fluid exposure, flow speed, temperature, pH, and radiation. The stent-induced flow disturbance had a significant role in maintaining hemodynamic behavior in coronary arteries that can subsequently influence the endothelial functions for an extended period [73]. The perfusion chamber simulated physiological WSS in cylindrical vessels that were quantified based on the Poiseuille flow equation:

$$WSS = 4\mu Q/\pi r^3 \tag{5}$$

where μ is the viscosity, Q is the flow rate, r is the radius of the cylindrical vessel [74].

A pseudo-physiological WSS of 30 dyne/cm^2 was imposed on the hydrogel-based stents having an internal diameter of 1.5 mm with a viscosity of 9.8×10^{-4} Pa.s at 37 °C, even though WSS under clinical conditions after stent insertion would be significantly lower [43]. As the atherosclerotic plaque transforms to stenosis, the WSS increases, especially at the

entrance of the stenotic region. It was suggested that an increase in WSS could reduce the fibrous cap of the plaque through apoptotic process, causing destabilization and rupture of vulnerable plaques. An enhanced WSS could also deteriorate the stability of an externally added stent. Thus, a pseudo-physiological WSS was utilized to mimic expedited experimental conditions.

As shown in Figure 10, an in-house perfusion chamber was designed to simulate the internal variables of blood vessels including wall shear. The constant flow of 2% fetal bovine serum (FBS) at 1 mL/sec was applied to the tube mimicking striated vessels. Unlike curved or branched vessels, the magnitude of flow disturbance in the straight tubes largely influences the mechanical strength of the stent [75], but the formulated 3D stent maintained its stability during the experiment.

The mechanical strength of all three types of stents was maintained against WSS for 72 hr. A constant flow of the medium caused the stents to swell by 20% of their initial weight in the first 2 hr (Figure 11a). The results were in good agreement with the swelling studies previously reported. The swelling ratio of SA-CYS-NF was significantly greater than those of SA and SA-CYS ($p<0.05$ at 72 hr), confirming that the addition of nanofibers in alginate-hydrogel enhanced capacity to retain water.

The degradation rates were estimated by extrapolating the *in vitro* experimental results to analyze the degradation pattern and shelf life of the 3D cardiovascular stents. These findings indicated that the hydrogel-based stents have sufficient stability, elasticity, and ability to maintain hemodynamic behavior in coronary arteries.
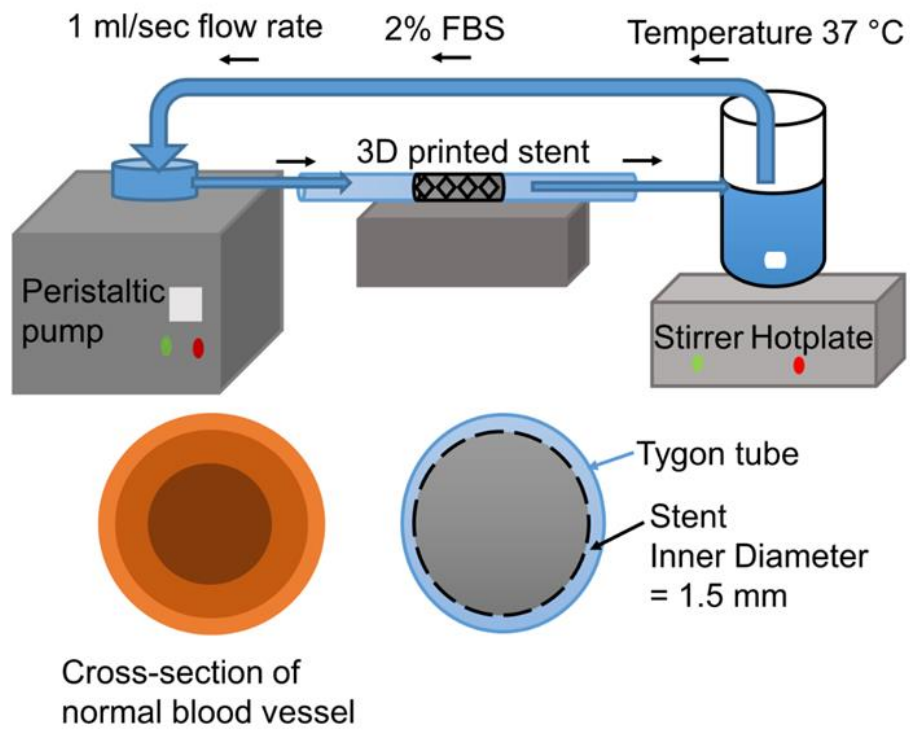
Figure 10. In-house perfusion chamber set-up to evaluate the mechanical stability against wall shear stress.
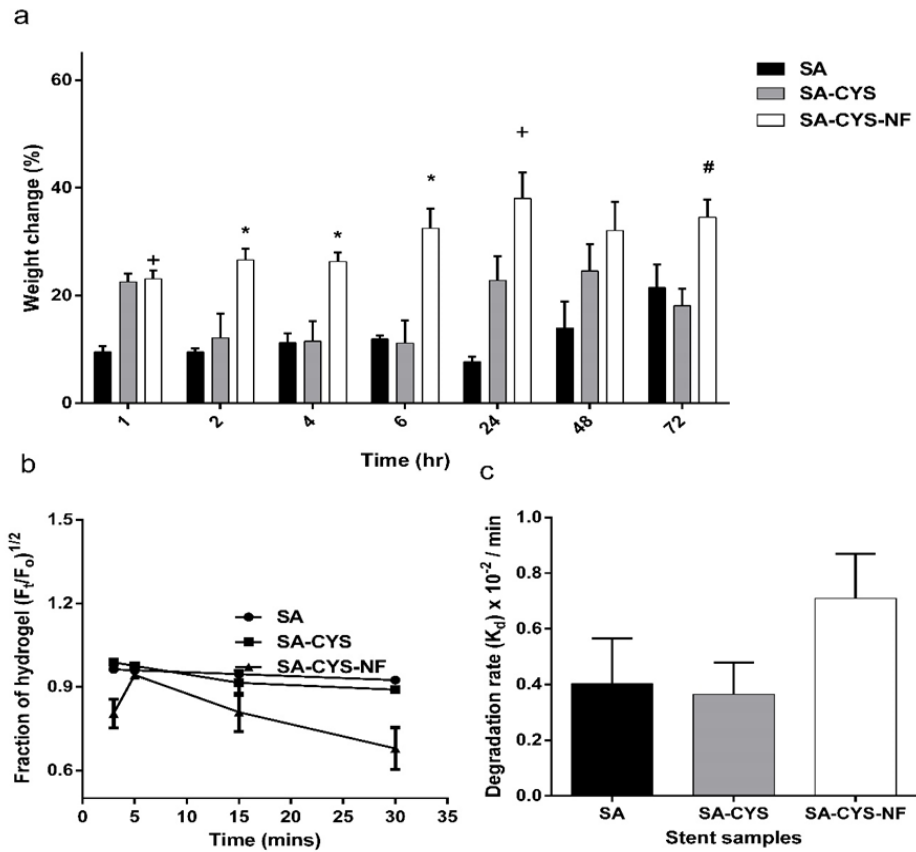
Figure 11. Assessment of the mechanical strength (a) Percentage weight change of stent formulations over a period of 72 hr, + indicates significance (p<0.05) difference between SA and SA-CYS-NF, # indicates significance (p<0.05) difference between SA-CYS and SA-CYS-NF, and * indicates significance (p<0.05) difference between SA, SA-CYS, and SA-CYS-NF, (b) *In vitro* degradation profiles of hydrogel-based stents, and (c) The degradation rate (K$_d$) of the stents.

Assessment of Degradation Rates of the 3D Stents

The degradation rate of stents in PBS at pH 7.4 was calculated based on the weight of remaining hydrogel in the in-house perfusion chamber. Alginate hydrogels undergo degradation in the presence of components such as divalent ions (Mg^{2+}), monovalent ions (Na^+), and calcium chelators (phosphates). The alginate dissolves, as it loses divalent cations which are replaced by monovalent ions in the culture medium [76].

The effects of the blood exposure on the disintegration rate of polyelectrolyte-behavior hydrogel stents were evaluated in PBS to determine the duration required for them to be completely biodegradable. The obtained data were fitted to the rate equation to establish a relationship between the fractions of hydrogel weights $(F_t/F_o)^{1/2}$ versus time t (Figure 11b). It was demonstrated that SA and SA-CYS had similar degradation profiles to each other, whereas SA-CYS-NF showed a higher degradation rate (K_d); 0.40×10^{-2}/min, 0.37×10^{-2}/min, 0.71×10^{-2}/min for SA, SA-CYS, and SA-CYS-NF, respectively, as shown in Figure 11c. Higher degradation rate for SA-CYS-NF could be due to greater water retention and the presence of thiol groups, which when exposed to the surrounding medium are susceptible to polymeric chain breakdown [77].

The local structure formed between the alginate chains and divalent ions provides enhanced mechanical strength to the stents, but this could be compromised due to the exchange of divalent ions with surrounding monovalent ions in the medium [78]. These results are also in good agreement with the previous studies where SA-CYS-NF showed a higher swelling ratio in the PBS medium. The results of this study clearly demonstrated that 3D-printed hydrogel-based stents offered required stability against shear stress and gradually degraded in the physiological fluid.

2.4. Conclusion

This study delineated the optimization process of hydrogel-based 3D printing of cardiovascular stents. Alginate hydrogels were robust and displayed sufficient strength against shear stress. The addition of nanofibers resulted in substantial enhancement of their swelling properties. It was evident that parameters such as the viscosity of the material, printing speed, and printing distance had an enormous impact on the 3D-printed shape and structure. Furthermore, the modification of alginate largely influenced the degradation rate of 3D-printed stents. This work can serve as a proof-of-concept for development and evaluation of 3D-printed stents with optimal mechanical integrity and biodegradation profiles for personalized cardiovascular stents that would promote better clinical outcomes.

CHAPTER 3

EVAULATION OF BIODEGRADABLE 3D-PRINTED CARDIOVASCULAR STENTS

3.1. Rationale

Metallic stent-induced vascular injuries cause endothelial cell impairment, leading to oxidative stress conditions, apoptosis in endothelial cells, and delayed re-endothelialization [6,79]. A BDS with controlled degradability within a given period can address the above-mentioned issues while providing the necessary strength and environment for healing the damaged endothelium. 3D printing techniques make it feasible to design a customized BDS used for an efficient atherosclerotic treatment. The most widely used 3D printing technique is the extrusion-based method wherein the base material is extruded through a narrow nozzle to produce printed devices on a support platform [80].

Hydrogel polymeric composites would be an ideal base for the cardiovascular stent owing to its nanoporous structure that suitably mimics the extracellular matrix and easily connects with the vascular system [81]. Poly(2-hydroxyethyl methacrylate) (pHEMA), a biodegradable and photo-curable polymer, has been frequently used for drug delivery [82,83], contact lenses [84,85], and tissue engineering applications [86,87]. Despite its various advantages, including biocompatibility and tunable mechanical properties, pHEMA has not been extensively explored for its application to cardiovascular scaffolds, mainly owing to its water-like viscous behavior. Poly-vinyl pyrrolidine (PVP) was added as a viscosity aid to the hydrogel ink to enhance the printability of pHEMA [88]. However, due to its low elastic modulus and lack of self-supporting nature, it primarily requires a support bath until UV light cures the printed material [89].

It was demonstrated that polymers like polyacrylic acid polymers (Carbopol) [90,91],

gellan gum [92], gelatin microspheres [93], agarose slurry [94], and pluronic-nanoclay polymeric matrix [95,96] could be used as support materials for 3D printing of various scaffolds. Based on the feasibility of the printing method and rheological properties of the product, Carbopol 974P NF (Lubrizol®, Cleveland, OH) polymer dissolved in 0.05 mM NaOH was selected as a support bath to fabricate a pHEMA hydrogel composite for a 3D-printed cardiovascular stent. Among the different fillers, nanocarbon materials including graphene oxide sheets have been frequently used owing to their highest aspect ratio which improve the mechanical properties of the hydrogels [97]. To reinforce the Young's modulus of the hydrogel stent, methacrylate graphene oxide (MeGO) was chosen to covalently link with the pHEMA hydrogel [98–100].

Resveratrol (RSL) is a polyphenolic compound found in red grapes and naturally produced in response to the injury [101]. Several studies have reported its inhibitory effects on oxidative stress-induced endothelial apoptosis [102], promotion of re-endothelialization [103], reduction of TNF-α inflammatory gene expression [104], and attenuation of H_2O_2-induced oxidative stress [105]. It was shown that there were dose-dependent increases in cerebral blood flow from RSL at concentrations of 5.65 and 14.4 ng/mL (0.025 and 0.061 μM) [106], offering upstream effectors against cardiovascular diseases [107,108].

RSL enhances NO production in endothelial cells ranging from 0.1 to 1 μM [35] through a G α-protein-coupled mechanism, leading to the upregulation of endothelial NO synthase (eNOS) expression [110,111]. As the enhanced levels of ROS in the coronary arteries significantly contributes to endothelial dysfunction [112], an adequate supply of NO in the vascular endothelium would maintain vasodilation [113], prevent platelet adhesion [114], and recover endothelial dysfunction [115]. Hence, the RSL-eluting stent would appropriately

alleviate the oxidative stress damage on the endothelium, thus improving the efficacy of the cardiovascular stent.

The objective of this study was to develop and evaluate 3D-printed cardiovascular stents based on pHEMA hydrogel that can be applied to recover endothelial cell functions. Addition of a nanofiller to the hydrogel ink can facilitate its 3D printability by affecting the pore size and reducing the swelling nature of hydrogel [116]. 3D cardiovascular stents based on the combination of pHEMA-MeGO and loaded with RSL will be evaluated and characterized for mechanical strength, degradability, swelling, and cytotoxic behavior in human umbilical vein endothelial cells (HUVECs).

3.2. Methods and Materials

Materials

Potassium permanganate ($KMnO_4$), sulfuric acid (H_2SO_4), phosphoric acid (H_3PO_4), hydrogen peroxide (H_2O_2), hydrochloric acid (HCl), 3-(trimethoxysilyl)propyl methacrylate (TMSPM), 2-hydroxyethyl methacrylate (HEMA), poly-vinyl pyrrolidine (PVP), phenylbis(2,4,6-trimethylbenzoyl)phosphine oxide (PBPO), and 2′,7′-dichlorofluorescin diacetate (DCFDA) were purchased from Sigma-Aldrich (St. Louis, MO). Isopropyl alcohol (IPA) was purchased from Oakwood Chemical (Estill, SC). Ethylene glycol dimethacrylate (EGDMA) and resveratrol (RSL) were purchased from TCI® America, Inc. (Portland, OR). Graphite flakes (Nano19) were a gift from Ashbury Carbons (Asbury, NJ). Raw 264.7 cells (mouse macrophages), Dulbecco's modified eagle's medium (DMEM), and penicillin-streptomycin solution were purchased from ATCC (Manassas, VA). Fetal bovine serum (FBS) was purchased from Atlantic Biologicals Corp. (Atlanta, GA). Human umbilical vein

endothelial cells (HUVECs), endothelial cell basal medium-2 (EBM-2), and endothelial cell growth medium BulletKit were purchased from Lonza (Mapleton, IL). All reagents and solvents were of analytical grade.

Preparation of Graphene Oxide (GO)

Graphene oxide (GO) was synthesized using the modified Hummer's method [117,118]. Briefly, 0.15 g of graphite was dispersed in 20 mL mixture of H_2SO_4 and H_3PO_4 (9:1). The mixture was stirred for a few minutes, and 0.9 g of $KMnO_4$ was slowly added to the mixture placed in an ice bath. The reaction mixture was kept at 50 °C for 12 hr, and 0.5 mL of 30% v/v H_2O_2 was added. It formed a dark-green solution upon the exothermic reaction. The solution was allowed to cool down and washed with hydrochloric acid (2M) and deionized (DI) water thrice at 12,000 rpm for 20 min and finally freeze-dried to obtain the final product in powdered form.

Preparation of Methacrylate Graphene Oxide (MeGO)

The dried GO (0.1 g) was added to 100 mL of anhydrous isopropyl alcohol (IPA). The solution was sonicated until GO was completely dispersed in the solution. Then, 5 mL of TMSPM was added to the solution under an inert atmospheric condition [52]. The mixture was stirred for 12 hr at 50 °C to allow TMSPA to react with hydroxyl groups of GO. Then, the contents were centrifuged using Sorvall® ST16R (ThermoScientific®, MA, USA) at 12,000 rpm for 20 min and washed thrice with IPA. The pellet was resuspended in DI water and freeze-dried for further characterization.

Rheological Properties of Hydrogel Inks

To characterize the rheological properties of hydrogel inks, strain-controlled Discovery Hybrid Rheometer 3 (DHR3) (TA Instruments®) attached with a 20 mm parallel plate at a gap of 1 mm was used at a temperature of 25 °C. The samples were equilibrated between the plates for 60 sec before the start of each experiment. An amplitude sweep study from 0-10% strain at a constant frequency of 1 Hz was performed to determine the linear viscoelastic region (LVR). At 1% of the strain selected from LVR, frequency sweeps were conducted with an angular frequency range from 0.1 to 100 rad/sec. Shear viscosity and flow behavior of the hydrogel inks were determined at a shear rate of 0.01 to 100/sec. The viscosity recovery studies were performed for 130 sec in three stages. In the stage I, the shear rate of 0.1/sec was applied for 60 sec, followed by a high shear rate of 100/sec for 10 sec in the stage II, and a low shear rate of 0.1/sec for 60 sec in the stage III [119].

Three-dimensional (3D) Printing Process of Cardiovascular Stents

The concentrations of PVP and MeGO were chosen based on the outcomes of our preliminary studies on rheological and formulation properties. All hydrogel inks were prepared from pHEMA based ink containing 15%w/v PVP dissolved in 1 mL of pHEMA with 1%w/v EGDMA and 2%w/v PBPO. For the pHEMA-0.35MeGO ink, 0.35%w/v of MeGO was added to pHEMA ink.

A 3D-printed cardiovascular stent (4 mm diameter and 6 mm length) was designed using Tinkercad® software, converted to a .gcode file using Cura® 15.04.6 slicing program (Figure 12a). The 3D printing was carried out using an extrusion-based 3D printer (Tissue Scribe®, 3D cultures, Delaware) and the process took ~25 min for each stent.

A slurry of Carbopol polymer (1.2%w/v) dissolved in NaOH (5 mM) was loaded onto a petri plate to hold the 3D-printed structure. As illustrated in Figures 12b and 12c, the printing process was conducted in the Carbopol support bath at a speed of 2 mm/sec with a layer height of 0.16 mm, 100% infill density. The 3D-printed stent was crosslinked using a 380 nm UV-light (Anker® Bolder LC 40) of 27 mW/cm^2 at a 3 cm distance for 60 mins. After curing with UV radiation, the final products were obtained and gently washed with 0.1 M PBS buffer for 15-20 min to remove the excess amount of Carbopol and any unreacted monomer sticking to the stent (Figure 12d). The final product was vacuum-dried and used for further studies.

Characterization of 3D-Printed Stents made of pHEMA or pHEMA-0.35MeGO

The presence of principal components in pHEMA or pHEMA-0.35MeGO stents were verified using a Fourier transform infrared (FTIR) spectrometer (ThermoScientific® Nicolet® IS® 10). Potassium chloride pellets were prepared with GO and MeGO (1-2 mg) for the FTIR measurements. Smart iTR® attenuated total reflectance (ATR) sampling accessory was used to collect spectra of pHEMA hydrogel inks. Each sample was scanned in the range of 4000 to 400 cm^{-1} for 64 scans at a resolution of 4. An X-ray diffractometer (Rigaku® Miniflex®) was used to determine the basal spacing (d-space) of raw graphite, GO, and MeGO. The diffractometer was prepositioned with CuK radiation ($\lambda = 1.54059$ A°) at a voltage of 15 kV, 35 mA, step size of 0.05°, step time of 3 sec, scan angle from 5° to 65° and the data were collected using Jade® version 8.5. The basal spacing (d-space) of the materials was determined using Bragg's equation;

$$\lambda = 2d \sin(\Theta) \tag{6}$$

Where d is the interlayer distance, λ is the wavelength of the radiation, and Θ is the diffraction

angle.

The surface morphology of 3D stents was also examined using SEM. The stents were cut into rectangular strips, loaded onto a carbon stub and coated with gold-palladium under vacuum for 15 min using a sputter-coater (Leica® EM SCD050, USA). The coated samples were then visualized using a Field-emission environmental SEM Philips XL30 (Leica®, USA) at a voltage of 5 kV.
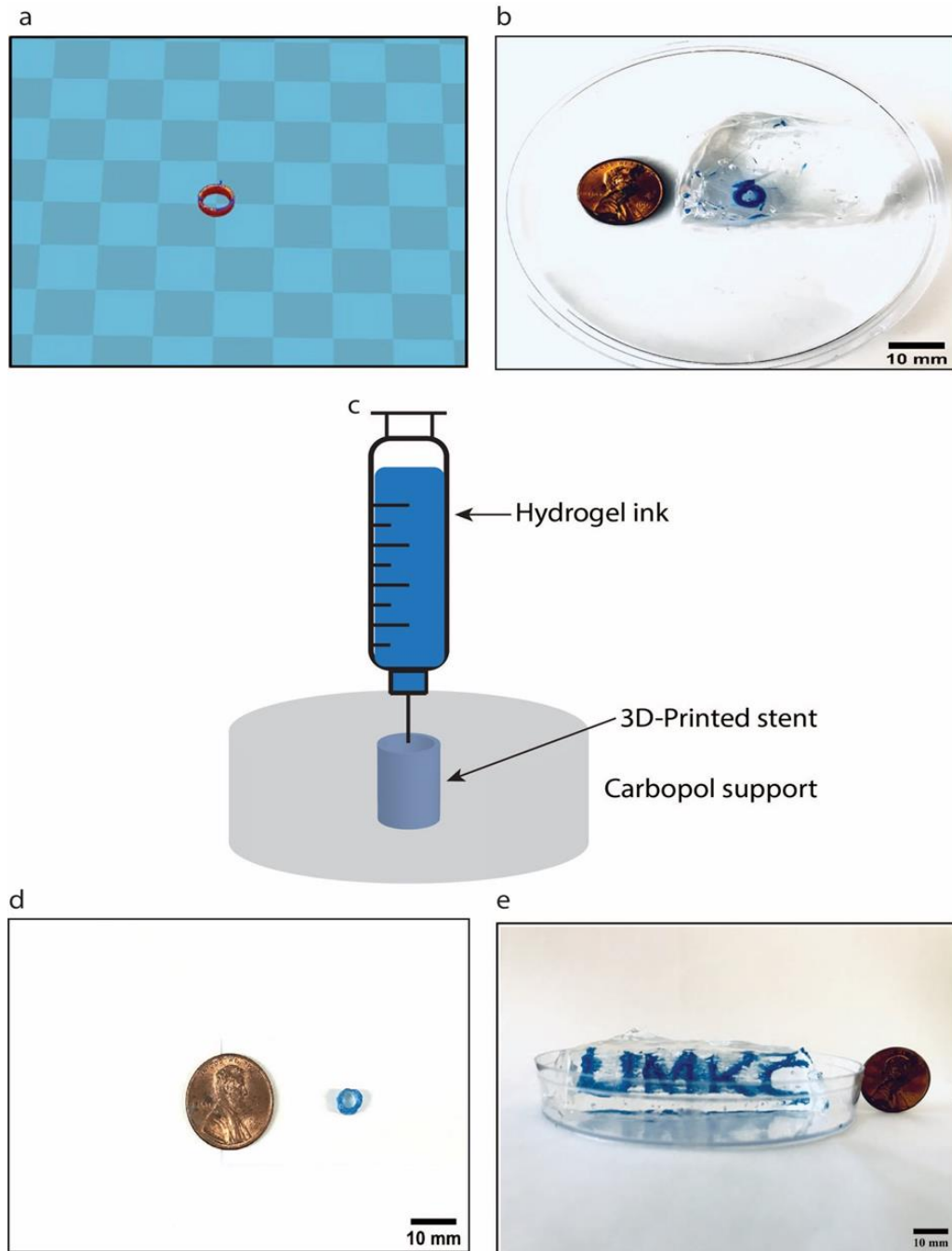
Figure 12. Schematic diagram of the 3D-printed stent (a) Slicing of the 3D model (.stl file) in Cura® program, (b) pHEMA stent printed in the Carbopol support bath (top view), (c) 3D printing of hydrogel-based stent in a support bath, (d) Top view of pHEMA stent after UV-crosslinking, and (e) "UMKC" printed in Carbopol support bath (blue dye was added for visualization purposes).

Assessment of Swelling Ratios of Hydrogel

Swelling ratio refers to the fractional increase in the weight of the hydrogel due to water absorption. A vacuum-dried stent with an initial volume of V_o was placed in 0.01 M PBS pH 7.4 at 37 °C for 72 hr. The swelled stent volume (V_1) was determined at predetermined time intervals after gently removing the surface water using Kim-wipes. The swelling ratios were calculated using the following equation:

$$\text{Swelling ratio } (\%) = \frac{V_1 - V_o}{V_o} * 100 \qquad (7)$$

Assessment of Degradation Rates of 3D Stents

To evaluate the effects of the 3D printing process on the degradation rate, stents were immersed in 0.01 M PBS (1 mL) pH 7.4 at 37 °C, and were taken out at predetermined time intervals and thoroughly dried. The difference in the weights between initial and dried stents was recorded. The degradation rates were determined by fitting the data to the following linear regression equation 3 [52].

Assessment of Mechanical Properties of Stents

To determine the mechanical strength of stents, compression studies were carried out using a twin column Bose® ElectroForce 3220 system (TA Instruments, ElectroForce Systems Group, MN, USA). Compressive-strain cycle loads of 10, 20, 30, 40, and 50% were applied to the 3D stents in a sequence [120]. The stent specimens were compressed at 1 mm/min speed using a 225 N load cell. A pre-load of 0.3-0.4 N was applied to the specimen before testing. The compressive stress and strain values were determined by dividing the load with the cross-sectional area (72.35 mm^2) and displacement with initial sample height (2 mm), respectively.

At predetermined time intervals, stents were taken out from 0.01 M PBS (1 mL) pH 7.4 at 37 °C, the surface water was removed, and the stents were vacuum dried. The stiffness (Young's modulus) of the stent was measured using stress vs. strain curves.

Assessment of RSL Release from 3D Stents

The *in vitro* drug release studies were performed under pseudo-physiological conditions. The optimal loading dose of RSL was chosen based on previous studies that have thoroughly examined 1) the amount of RSL released from the hydrogel formulations and 2) therapeutic effects of RSL through *in vitro* cell culture studies. Therefore, a multi-step experimental design was employed to select the final dose *i.e.*, 1 mM of RSL which was added to the hydrogel ink prior to the printing process.

To determine the release rate of RSL, the 3D stent loaded with RSL (1 mM) was placed in 1 mL of 0.01 M PBS pH 7.4 containing 10%v/v ethanol at 37 °C. Since RSL is poorly soluble in water, ethanol was added to the medium to maintain sink conditions. The concentration of RSL was analyzed at 316 nm using a UV-visible spectrometer (Molecular Devices® Spectramax 190, Hampton, NH, USA). At each time point, the whole release medium was removed and replaced with fresh medium. The amount of RSL released was measured at predetermined intervals and fitted to the mathematical models to determine the release kinetics of RSL from 3D stents.

Cell Viability Study on HUVECs

To evaluate the effects of 3D stents on the viability of HUVECs, *in vitro* cell viability studies were conducted using the MTS assay. Metabolically active cells convert the reagent

used in the assay into a colored formazan product whose absorbance can be measured at 490 nm. The HUVECs were cultured in the EBM-2 BulletKit (Lonza®, Morristown, NJ) containing bovine brain extract (BBE), ascorbic acid, hydrocortisone, human epidermal growth factor (hEGF), FBS, gentamicin/amphotericin-B (GA). The viability of HUVECs (passage 2-5) upon exposure to 3D-printed stents (4 mm diameter and 6 mm length) loaded with RSL (~1 mM) was examined by cell proliferation assay (Promega®, San Luis Obispo, CA).

Briefly, 10,000 cells (100 µL) per well were seeded and incubated overnight. On the following day, the medium was replaced with 100 µL of fresh medium and incubated at 37 °C with 5% CO_2. Culture medium without 3D stent samples containing RSL was used as a negative control. After the predetermined time intervals, MTS solution (20 µL) was added to each sample, and absorbance values were recorded at 490 nm using a multimode detector (Molecular Devices® Spectra max 190, Hampton, NH, USA).

Live-Dead Cell Viability Assay

Samples of 3D stents were placed in EBM-2 medium (1 mL) for 24 hr at 37 °C and 5% CO_2. After 24 hr, 100 µL of cell suspension (10^6/mL) was added to the 3D stent samples and incubated for another 24 hr. The cell viability was examined using acetomethoxy-calcein (Calcein AM), propidium iodide (PI) staining solution (Biotium®, Fremont, CA). The viability of cells on the stent surface was examined using fluorescence microscopy BZ-X800 (Keyence®, Itasca, IL). Red fluorescence represents dead cells due to the binding of ethidium homodimer to the nucleic acids, whereas green fluorescence represents live cells due to the cleavage of calcein-AM.

Assessment of the Amount of NO Produced

To assess the amount of nitrite produced in the cell culture supernatant upon exposure to 3D stent samples containing RSL (~1 mM), Griess assay was performed. The Griess reagent was prepared by mixing of 0.2%w/v solution of N-(1-naphthyl)ethylenediamine dihydrochloride (NED) in DI water and 2%w/v sulfanilamide dissolved in 5%v/v phosphoric acid solution.

Briefly, 10,000 cells (100 µL) were seeded in each well and 3D stent samples were loaded and allowed for attachment. The medium was replaced on the following day. After the specific time intervals, 100 µL of the medium in the plate was transferred to fresh 96-well plate and 50 µL of 2%w/v sulfanilamide solution and 50 µL of 0.2%w/v NED solution was added to each sample, and absorbance values were recorded at 540 nm using a multimode detector (Molecular Devices® Spectra max 190, Hampton, NH).

Effects of 3D-Printed Stents on HUVEC Apoptosis

To assess the antiapoptotic effects of RSL, the HUVECs were incubated with the 3D stent samples for 2 hr followed by treatment with or without 100 µM H_2O_2 for 24 hr. The protective nature of the drug-eluting stent from H_2O_2-induced apoptosis was evaluated using Annexin V-FITC/PI Apoptosis Detection kit (Cayman® Chemical, Ann Arbor, MI) that allows fluorescent detection of annexin V bound to apoptotic cells. The percentage of live cells, early/late apoptosis, and necrosis were quantitatively determined using BD FACS Canto II flow cytometer equipped with BD FACS Diva software (BD Biosciences®, San Jose, CA).

Assessment of Pro-inflammatory Cytokine Levels in Raw 264.7 Cells

To examine the biocompatibility of 3D stents, the production of pro-inflammatory

cytokine (TNF-α) upon exposure to the 3D stent samples was determined using an enzyme-linked immunosorbent assay (ELISA) (e-Biosciences® San Diego, CA). Raw 264.7 cells (Monocyte/macrophage-like cells) were grown in Dulbecco's modified eagle's medium (DMEM) containing 100 units/mL penicillin and 100 μg/mL streptomycin supplemented with 10%v/v FBS at 37 °C and 5% CO_2. Briefly, 20,000 cells (100 μl) per well were seeded and pretreated with the samples of 3D stent samples containing RSL (~1 mM) and DMEM media for the test and control group, respectively. 100 μM H_2O_2 was added to both the groups and incubated for 24 hr. Then, the supernatant medium of the cells was transferred into a new 96-well plate and quantified for TNF-α levels as per the manufacturer protocol.

Effects of 3D-Printed Stents on Intracellular Reactive Oxygen Species (ROS) Levels

To evaluate the intracellular ROS levels in HUVECs, DCFDA, a fluorescent dye, was used. Initially, 10,000 cells per well (100 μL) were seeded and pretreated with the 3D stent samples containing RSL (~1 mM) for 2 hr, followed by incubation with 100 μM of H_2O_2 for 24 hr. After incubation, the cells were washed with PBS and treated with 20 μM of DCFDA dye at 37 °C for 20 min. The fluorescent images were collected at 10X magnification using fluorescent microscopy BZ-X800 (Keyence®, Itasca, IL). The fluorescence intensity was quantified using ImageJ software [121].

Statistical Analysis

All experiments were carried out in triplicate unless otherwise specified, and expressed as mean±SEM. A Student's *t*-test was used to compare the two groups, whereas one-way analysis of variance (ANOVA) followed by Tukey's HSD analysis was used to compare

multiple groups. All statistical analyses were carried out using SPSS® software (IBM® Corp. Armonk, NY). p-values represent different levels of significance: *p<0.05, **p<0.01, and ***p<0.001.

3.3. Results and Discussion

Characterization of GO and MeGO

Graphene oxide (GO) was synthesized from graphite powder using modified Hummer's method. The schematic representation of GO modification with methacrylate groups to form MeGO and subsequent crosslinks with EGDMA is shown in Figures 13a and 13b. As shown in Figure 14a, there was a distinctive peak at 230 nm and a shoulder peak at 298 nm corresponding to the π–π* and n−π* transitions related to C=C and C=O groups, respectively [52].

As shown in Figure 14b, the FTIR spectra of GO and MeGO had the low-intensity peaks at 3330, 1720, and 1619 cm^{-1} for O–H, C=O, and C=C stretching vibration modes, respectively [122]. In addition, the spectral peaks (Figure 14d) corresponding to the functional groups at 1062 cm^{-1} (Si-O), 1386 cm^{-1} (Si-C) in MeGO, and hydroxyl peak with lowered intensity confirmed the conjugation of methacrylate groups on GO [52].

X-ray diffraction (XRD) analysis was used for crystallographic structure characterization based on the interlayer spacing (d) between the graphene layers in GO and MeGO was per was performed. A solid peak at 26.5º (2Ө) corresponding to pristine graphite was observed at d-space of 0.34 mm (Figure 14c). In the GO diffraction curve, the peak was shown at 13º with a d-space of 0.68 nm. The addition of oxygen-containing functional groups on the sheets was reported to enhance the d-spacing of graphene layers [123]. Accordingly,

GO modification shifted the peak to 12º with a d-space of 0.74 nm, confirming the covalent

bonding between the methacrylate and hydroxyl groups.
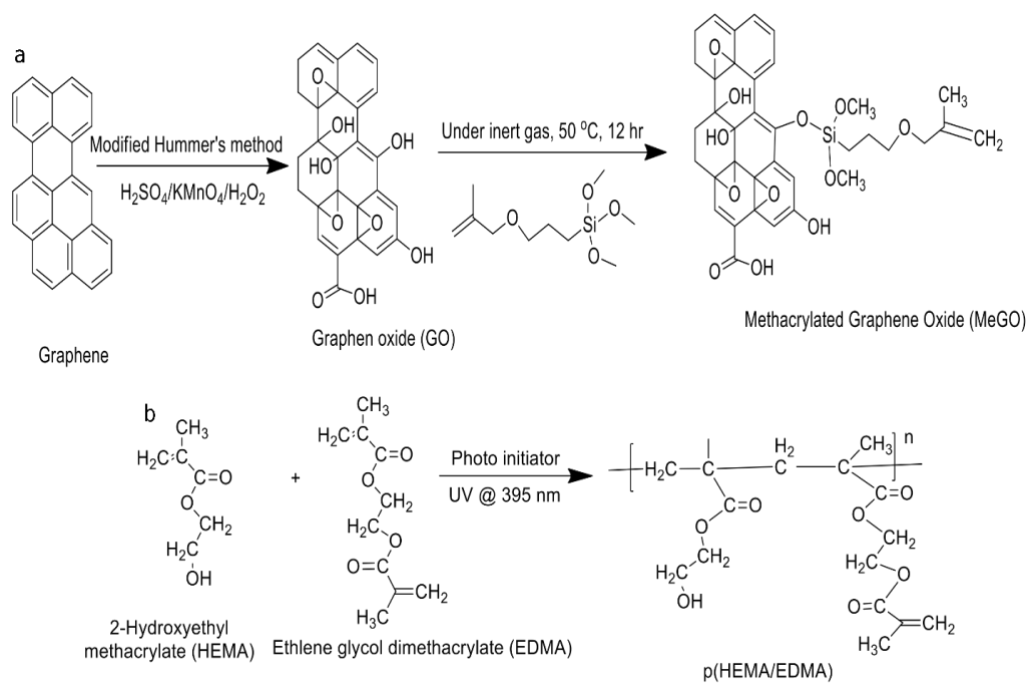
Figure 13. Schematic diagrams for (a) synthesis of MeGO and (b) crosslinking between HEMA and EDGMA.
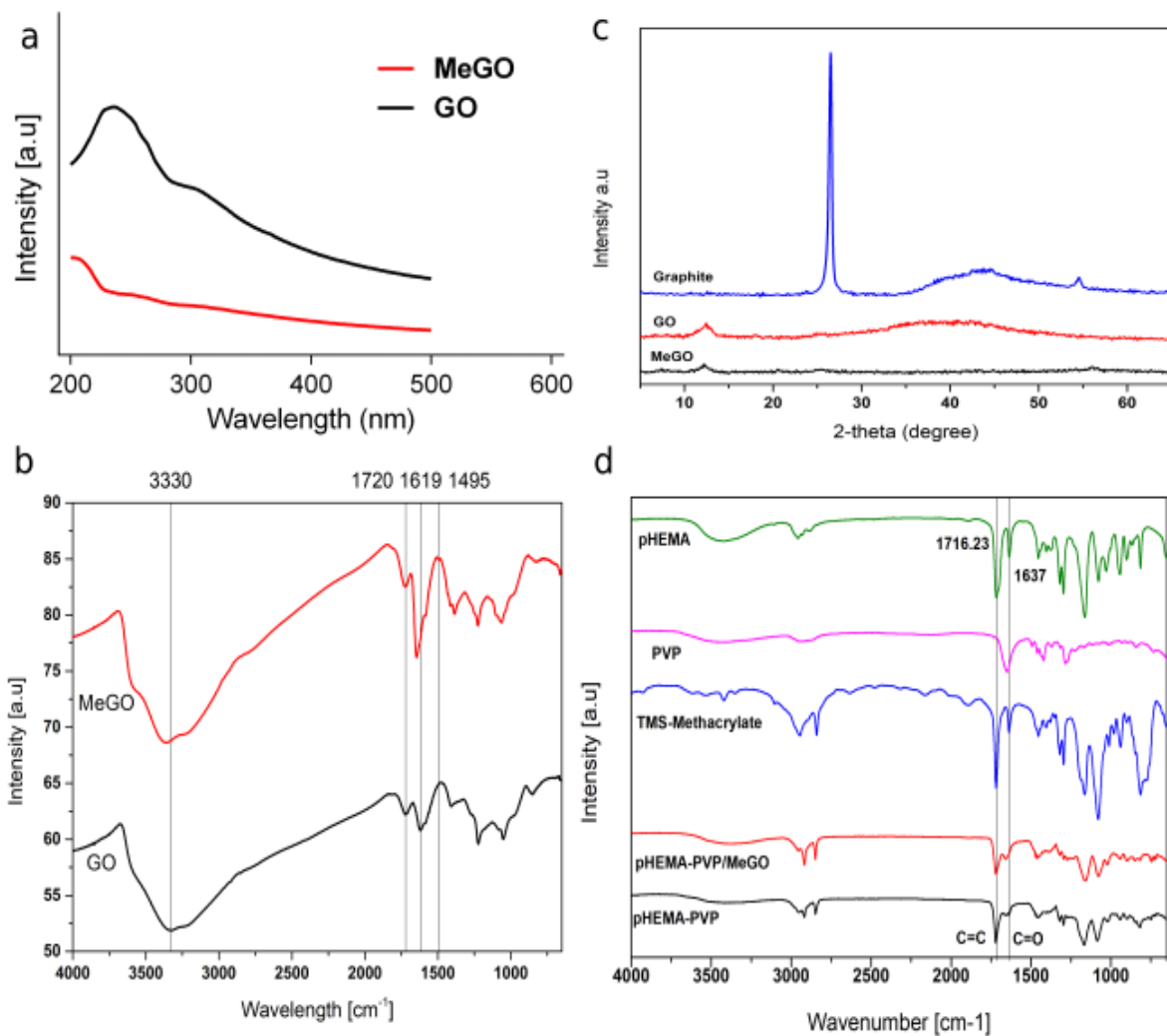
Figure 14. (a) UV-Visible absorption spectra of GO and MeGO, (b) FTIR spectra of of GO and MeGO, (c) XRD spectra of graphite, GO and MeGO, and (d) FTIR spectra of pHEMA hydrogel stents.

Rheological Properties of Hydrogel Inks

The rheological behavior of the hydrogel inks provides information about the material stability and shear-thinning properties during the printing process. As the 3D ink is subject to shear stress while flowing through the narrow orifice, the material's polymeric microstructure and subsequently its ability to retain the 3D structure will be changed. Two types of flow measurements, namely rotational and oscillational, were conducted to examine the viscosity, creep recovery, flow behavior, and LVR.

The changes in the storage modulus (G') and loss modulus (G") for Carbopol and the two hydrogel inks (pHEMA and pHEMA-0.35MeGO) are shown in Figures 15a, 15b, and 15c. In the case of support bath, the elastic nature of the material was more dominating property than its viscous nature. The linear viscoelastic behavior of the support bath was observed up to 1% strain (tested range of 0.1-10%). As the strain increases, the material becomes more likely to break its microstructure and begins to flow. However, at lower strain values, G" was more significant than G', indicating that liquid behavior predominates over the solid behavior.

In the frequency sweep test conducted at a constant amplitude, the value of G' should be directly related to the network structure of the polymeric material. As shown in Figures 15d and 15e, the frequency sweep of G' and G" were presented as a function of angular frequency. In the case of support bath samples, G' was higher than G" at lower frequencies, but it slowly decreased and G" gradually increased at higher frequencies. A dynamic equilibrium between the solid and liquid nature of the material could assist hydrogel inks in preserving the 3D structure (*i.e.*, the forming and breaking of the polymeric intermolecular bonds) during and after the printing process [124].
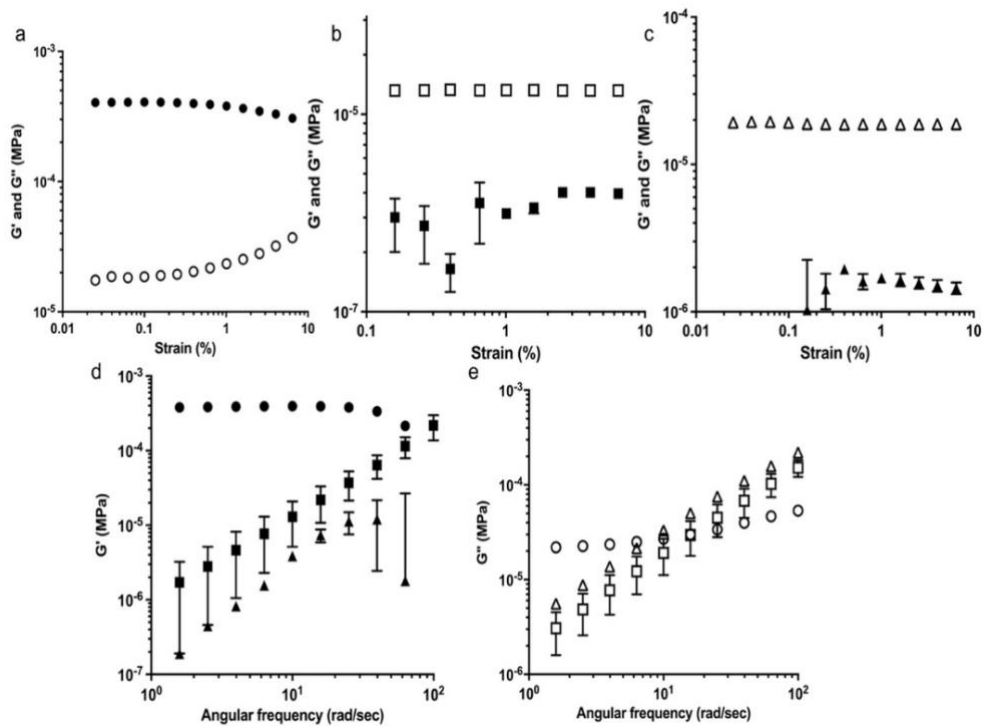
Figure 15. Rheological properties of Carbopol and hydrogel inks. Amplitude sweep plots of (a) Carbopol, (b) pHEMA, and (c) pHEMA-0.35MeGO hydrogel inks. (d) displaying storage modulus (G') and (e) loss modulus (G") of Carbopol, pHEMA, and pHEMA-0.35MeGO as a function of angular frequency. Symbol legend: circles, Carbopol; squares, pHEMA; triangles, pHEMA-0.35MeGO. Corresponding error bars are also displayed for all cases (in many instances, the errors are too small to be visible). The data are presented as mean±SEM (N=3).

The apparent viscosities of the hydrogel samples at varying shear rates are shown in Figures 16a, 16b, and 16c. The viscosities of all hydrogel materials were inversely proportional to their shear rates. The rationale behind this behavior could be because the polymeric intermolecular bonds are tangled and build-up resistance, requiring more torque to rotate the top plate.

The flow curves of the samples between the shear rate and shear stress are depicted in Figures 16d, 16e, and 16f, demonstrating that they display a non-Newtonian nature with shear-thinning behavior. The Carbopol followed a Bingham plastic flow, whereas the hydrogel inks displayed a pseudoplastic behavior. In Bingham fluids, the material has yield stress – a critical value of stress below which the material does not flow. As the external stimuli lower the yield stress, the solid nature continues to dominate, absorbing the stress-energy without flowing. However, when the applied stress exceeds the yield stress, the structure of the material collapses and it begins to flow.
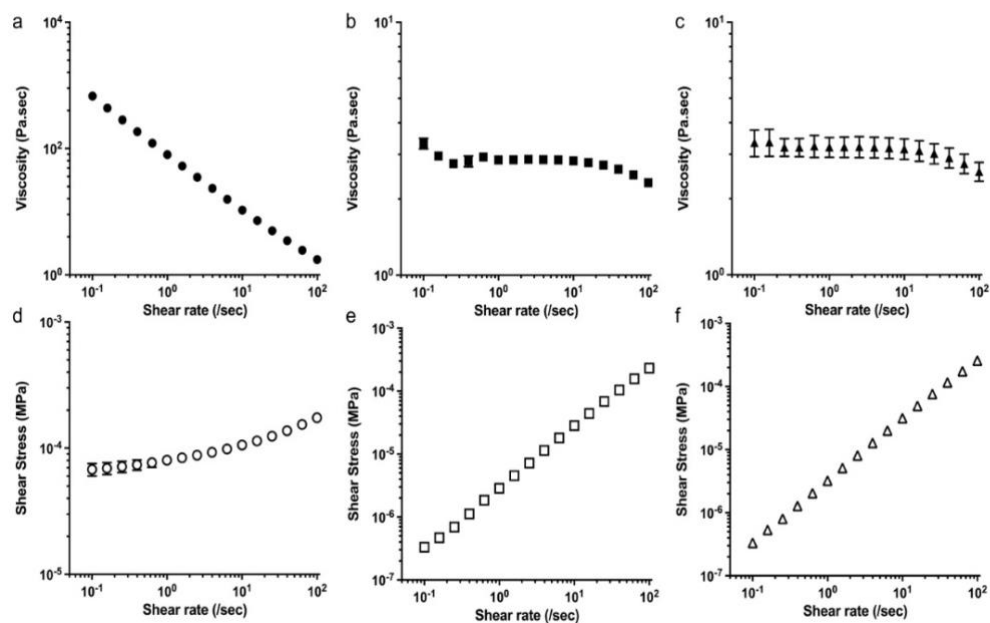
Figure 16. Characterization of the flow behavior of Carbopol and hydrogel inks. Viscosity (Pa . sec) *versus*. shear rate (/sec) plots for (a) Carbopol, (b) pHEMA, and (c) pHEMA-0.35MeGO). Flow curves – shear rate versus. shear stress plots for (d) Carbopol, (e) pHEMA, and (f) pHEMA-0.35MeGO. The data are presented as mean±SEM (N=3).

The Herschel-Bulkley model for Bingham fluids with yield stress was applied to quantify the non-Newtonian behavior using the equation given below.

$$\sigma = \sigma_o + K \dot{\gamma}\, n \tag{8}$$

Where $\dot{\gamma}$ is shear rate, K is the consistency, σ and σ_o are shear stress and yield stress, respectively. The value n is the power-law index denoting the flow behavior, where n=1 is considered Newtonian fluid, whereas n<1 and n>1 indicate shear-thinning and shear-thickening fluid types, respectively [125]. The yield stress and the power-law index of the support bath were $59 \pm 10 \times 10^{-6}$ and $0.39 \pm 0.04 \times 10^{-6}$ MPa, respectively.

Due to the Bingham fluid nature of Carbopol, it behaves as an elastic-solid, allowing it to hold the 3D structure of the hydrogel inks. The addition of MeGO to the hydrogel inks did not alter the power-law index of the inks (pHEMA - 0.89 ± 0.01 and pHEMA-0.35MeGO - 0.89 ± 0.02), maintaining a shear-thinning property that could minimize the flow resistance through the needle at high extrusion rates during the 3D printing process.

The shear thinning property of hydrogel inks were further examined by the degree of viscosity recovery. The shear rate ($\dot{\gamma} = 73$/sec) experienced by the fluid during extrusion was calculated by the following equation [126]

$$\dot{\gamma} = 8V/d \tag{9}$$

Where V is the printing speed (2 mm/sec) and d is the diameter of the needle (0.22 mm).
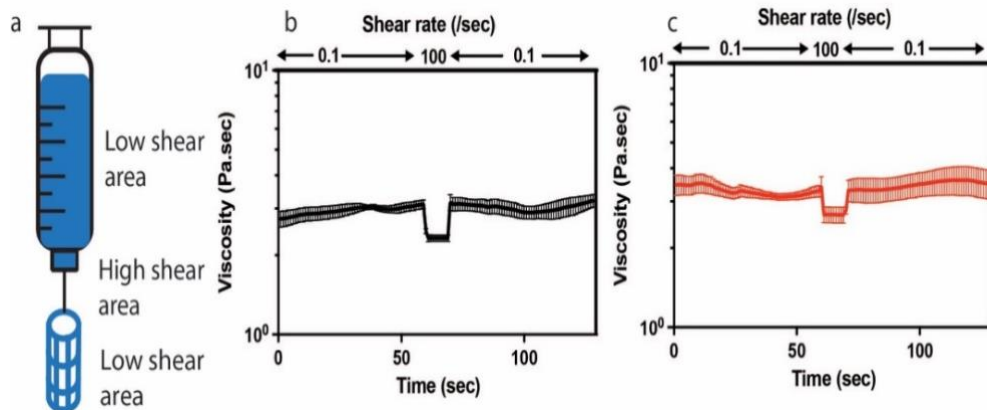
Figure 17. Changes in viscosity as a function of time at various shear rates. (a) Schematic representation of the high shear area and low shear area when extruding from the syringe, and viscosity recovery plots of (b) pHEMA and (c) pHEMA-0.35MeGO. The data are presented as mean±SEM (N=3).

To simulate the 3D printing process, a low shear rate (0.1/sec) for 60 sec, representing the ink in syringe cartridge, and a high shear rate (100/sec) for 10 sec, mimicking the ink passing through a narrow nozzle, were applied. Finally, a low shear rate (0.1/sec) for 60 sec, denoting the recovery stage, was applied. As shown in Figures 17a, 17b, and 17c both hydrogel inks returned to their original viscosity during the recovery stage, minimizing the layer spreading of the printed material after extrusion.

Assessment of Swelling Ratio of 3D Stents

To assess the absorption of the surrounding fluid by the porous networks in the polymeric hydrogels, the swelling ratios were calculated based on the volume change of the stents. As shown in Figure 18a, the volume change of 3D stents immersed in 0.01 M PBS at 37 °C for 2 hr were determined as 26.0±3.1% and 1.0±1.0% for pHEMA and pHEMA-0.35MeGO stents, respectively. These values increased to 39.2±5.3% and 7.7±1.6%, respectively, after 72 hr. The addition of MeGO to the pHEMA stent not only significantly (p<0.01) lowered the swelling ratio, but also kept the swelling ratio constant after 24 hr. The addition of MeGO to the hydrogel resulted in effective dense crosslinking of hydrogels, reducing the swelling ratios, and maintaining the structural integrity of 3D stents.

It has been reported that pH controls the swelling rate of the base polymer and drug release rate is in turn controlled by the swelling rate. The degree of crosslinking and varying water solubility of loaded drug with the external pH also affect the swelling rate and drug release rates from the system [127].

Polymeric system used to formulate drug loaded cardiovascular stents should not be too crosslinked in a manner that it prevents the diffusion of drug from the system. As this

system is intended to be implanted in the coronary artery, where the pH is 7.4, the system should exhibit less swelling and exert lower drug release rate. Thus, rigidity of the system is maintained, and drug release period can be elongated. For pHEMA hydrogels used in this study, as pH increased from 2 to 7, the swelling ratio and drug release rate decreased (since the monomer ratio increased) [128,129]. These are the various reasons for the selection of this polymer which has the potential to demonstrate optimal efficacy.

The surface morphology and internal structure of the stents were examined through SEM studies. As shown in Figure 18b, the pores with irregular random sizes were distinctively discovered in the pHEMA stent. The presence of MeGO particles in the MeGO-pHEMA stents resulted in a tight network through covalent conjugation in the hydrogel, removing most pores and reducing the swelling ratios of the 3D stents. The MeGO particles were uniformly dispersed in the pHEMA hydrogel ink. Upon polymerization, the MeGO particles were evenly entrapped into the polymeric network of hydrogels [52,130].
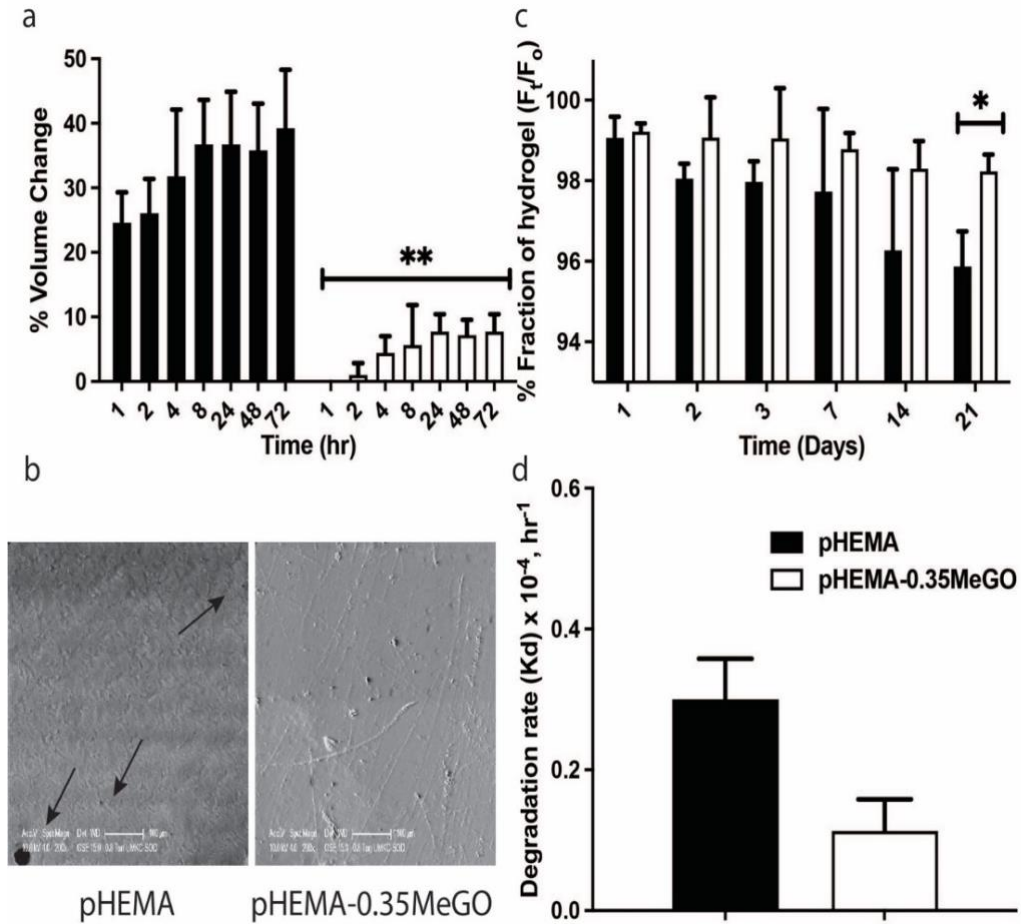
Figure 18. Evaluation of swelling and degradation rates of the 3D stents. (a) The changes in the volume of the hydrogel stent as a function of time, (b) SEM micrographs of pHEMA (arrows indicate porous structures) and pHEMA-0.35MeGO, (c) The degradation kinetics of the stents, and (d) The first-order degradation rate (K_d) of 3D stents. The data are presented as mean±SEM (N=3). *p<0.05 and **p<0.01 based Student's *t*-test.

Assessment of the Degradation Rate of 3D Stents

To determine the duration required for the stents to be completely biodegradable, the effects of polyelectrolyte medium (0.01 M PBS pH 7.4) on the degradation rate of hydrogel stents were evaluated based on the percentage fraction of weight remaining [119]. As shown in Figure 18c, the remaining fractions of 3D stents after 21 days were determined to be 95.9±0.5% and 98.2±0.3% for pHEMA and pHEMA-0.35MeGO stents, respectively.

The obtained data were fitted to the rate equation to establish a relationship between the fractions of hydrogel weight $(F_t/F_o)^{1/2}$ *versus* time. As shown in Figure 18d, the degradation rates (K_d) were determined as $0.30\pm0.06\times10^{-4}$ /hr and $0.11\pm0.04\times10^{-4}$ /hr for pHEMA and pHEMA-0.35MeGO, respectively. The addition of MeGO did not significantly change the degradation rates of 3D stents, indicating that the physical association of MeGO in pHEMA stent had a little effect on the degradation rate. The results of this study demonstrate that 3D-printed hydrogel-based stents are gradually biodegradable upon exposure to the polyelectrolyte medium.

Assessment of Mechanical Properties of 3D Stents

To evaluate the fundamental mechanical strength and the internal deformations of hydrogel-based stents, cyclic compression studies which involve the application of an enhanced strain to the stent in each cycle were performed (Figure 19a). The plot between the maximum displacement of the sample measured after each cycle is shown in Figure 19b. In addition, Young's moduli were determined from the slope of the elastic region in the stress-strain curve (Figure 19c).
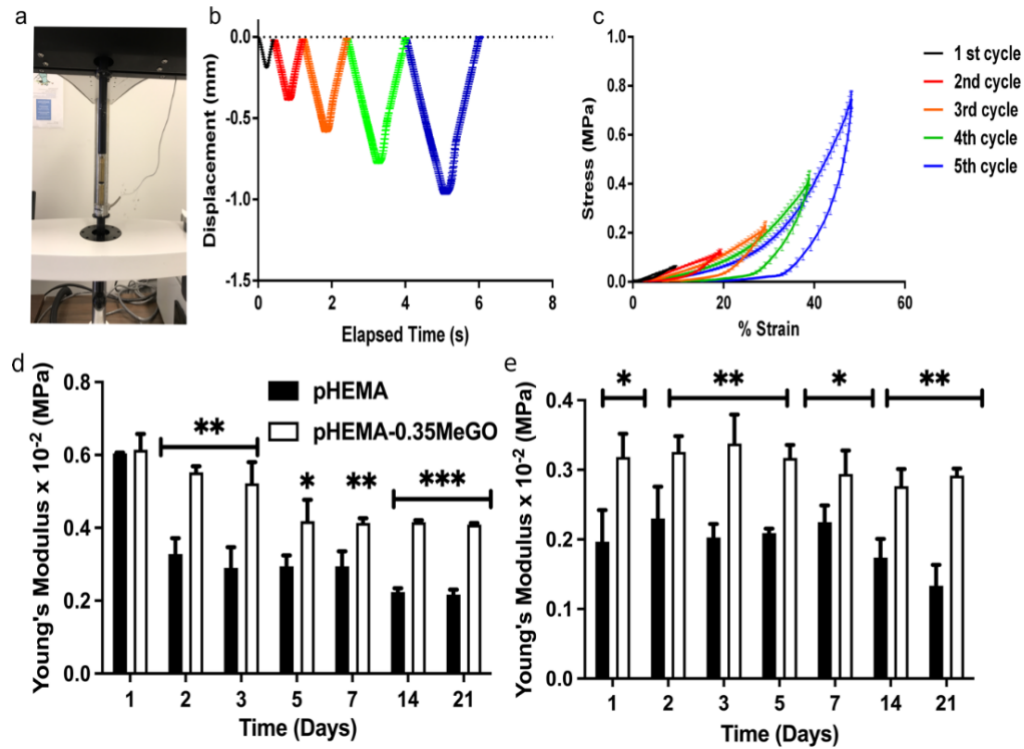
Figure 19. Cyclic compressive testing of hydrogel stents. (a) Representative image of compression testing set-up, (b) Displacement *versus*. time plot, and (c) Stress vs. strain curves of pHEMA stent. Changes in Young's moduli of pHEMA and pHEMA-0.35MeGO in (d) First cycle and (e) Fifth cycle. The data are presented as mean±SEM (N=3). *$p<0.05$, **$p<0.01$, and ***$p<0.001$ based Student's *t*-test.

As shown in Figure 19d, Young's modulus of pHEMA stent decreased from $0.60\pm0.01\text{x}10^{-2}$ MPa to $0.22\pm0.01\text{x}10^{-2}$ MPa after 21 days. In the case of a pHEMA-0.35MeGO stent, Young's moduli of $0.61\pm0.02\text{x}10^{-2}$ MPa and $0.41\pm0.01\text{x}10^{-2}$ MPa were obtained on day 1 and day 21, respectively. As shown in Figure 19e, the Young's modulus of pHEMA after five cycles on day 21 was $0.13\pm0.02\text{x}10^{-2}$ MPa, whereas the addition of MeGO significantly enhanced the elastic stiffness of the stent to $0.29\pm0.01\text{x}10^{-2}$ MPa ($p<0.01$). Approximately a two-fold increase in Young's modulus was observed in pHEMA-0.35MeGO stents, indicative of excellent rigidity and stiffness. The presence of MeGO reinforced against internal deformative properties of 3D stents and enhanced load-bearing efficiency during the multiple loading-unloading compression cycles. These results demonstrated that the addition of MeGO enhanced the mechanical strength of the hydrogel-based stents. Further *in vitro* drug release and cell culture studies were carried out on 3D stents made of pHEMA-0.35MeGO.

Assessment of RSL Release from 3D Stents

As shown in Figure 20a, the amount of RSL released from 3D stents displayed a sustained-release pattern with no initial burst release. Furthermore, the presence of MeGO in the stents did not affect the amount of RSL released from the stents when compared with those made of pHEMA alone. The cumulative percentages of RSL released from 3D stents after day 1 were 15.3 ± 1.2 and 14.9 ± 0.7 from pHEMA and pHEMA-0.35MeGO stent, respectively, whereas those after day 7 were 37.8 ± 1.7 and 32.3 ± 2.8, respectively. The addition of MeGO produced smaller pores in the hydrogel network and influenced drug diffusion due to the steric hindrance effects, leading to slower, but not significantly different, release rate of RSL [131].

The conditions in which we conducted drug release studies closely mimic those in the

blood. It was reported that the drug release rate from the stents was mainly governed by diffusion-controlled mechanism rather than degradation of the polymeric matrix network. In the light of mechanical properties of pHEMA-0.35MeGO stent, it would display excellent product stability in the compression cycle and offer therapeutically effective diffusion-controlled release rates.

The release profiles of RSL were fitted to mathematical models such as zero-order, first-order, Korsmeyer-Peppas, and Higuchi models to describe the release kinetics. As shown in Table 1, the highest correlation coefficient of the release profile is obtained from the Higuchi model, indicative of a diffusion-controlled release mechanism. Thus, the results of this study warranted further studies on the effects of the controlled release behavior of RSL from the stents on providing adequate NO supply essential for preventing smooth muscle cell migration and platelet aggregation.
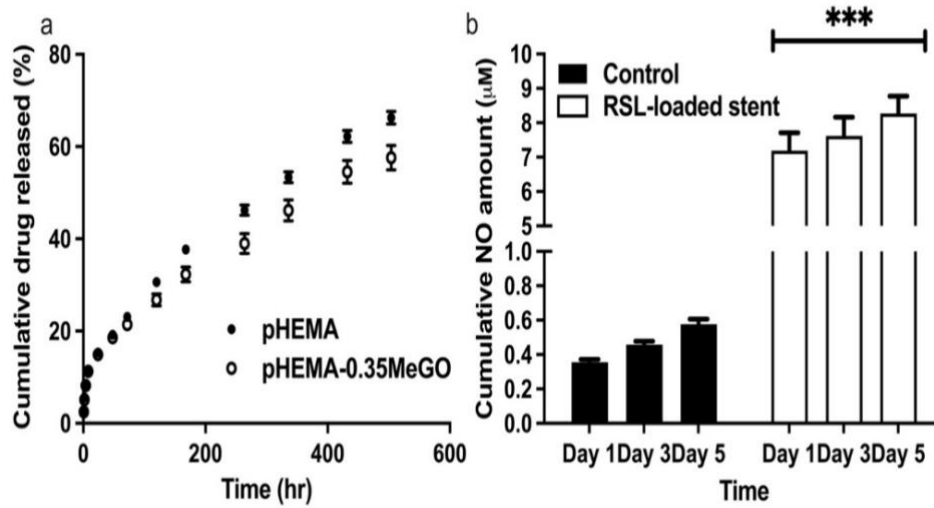
Figure 20. (a) *In vitro* drug release profiles of 3D stents and (b) Effect of 3D stent samples containing RSL on the production of NO from HUVECs. The data are presented as mean±SEM (N=3). ***p<0.001 based Student's *t*-test.

Model	R² value	
	pHEMA	pHEMA-0.35MeGO
Zero-order	0.9566	0.9541
First-order	0.6813	0.6728
Koresmeyer-Peppas	0.9769	0.9751
Higuchi	0.9952	0.9927

Table 1. Correlation coefficients for tested mathematical models.

Assessment of the Amount of NO Produced

To assess the amount of NO produced from 3D stent samples containing RSL (~1 mM), the Griess assay was performed. As shown in Figure 20b, the cumulative amounts of NO produced were 0.47 ± 0.22 µM and 7.19 ± 0.52 µM after day 1 and 1.44 ± 0.01 µM and 8.27 ± 0.51 µM after day 5 for control and 3D stents, respectively. There was a significant difference ($p < 0.001$) in NO production between the control and 3D stents. This study demonstrated that the 3D stents containing RSL promoted NO release from HUVECs that could suppress platelet adhesion and activation. The outcomes of this study could provide insights into the beneficial effects of RSL on recovering endothelial functions.

Effects of 3D-Printed Stents on Cell Viability

As shown in Figure 21a, the MTS assay showed no significant differences in the absorbance values between the control and 3D stent exposure groups, indicating that 3D stents containing RSL exerts no cytotoxic effects on the viability of HUVECs. When working with biomedical devices which would be in a direct contact with the cells, it is necessary to study whether cell viability is influenced upon being exposed to the stent surface. To minimize the complexity, a simple protocol was designed to allow HUVECs to be attached to the stent surface at least for 24 hr. Most cells seeded on top of the stent surface remained viable even after being exposed to 3D stents containing RSL (Figures 21b and 21c). These results from the Live-Dead assay are in good agreement with those from the MTS assay.
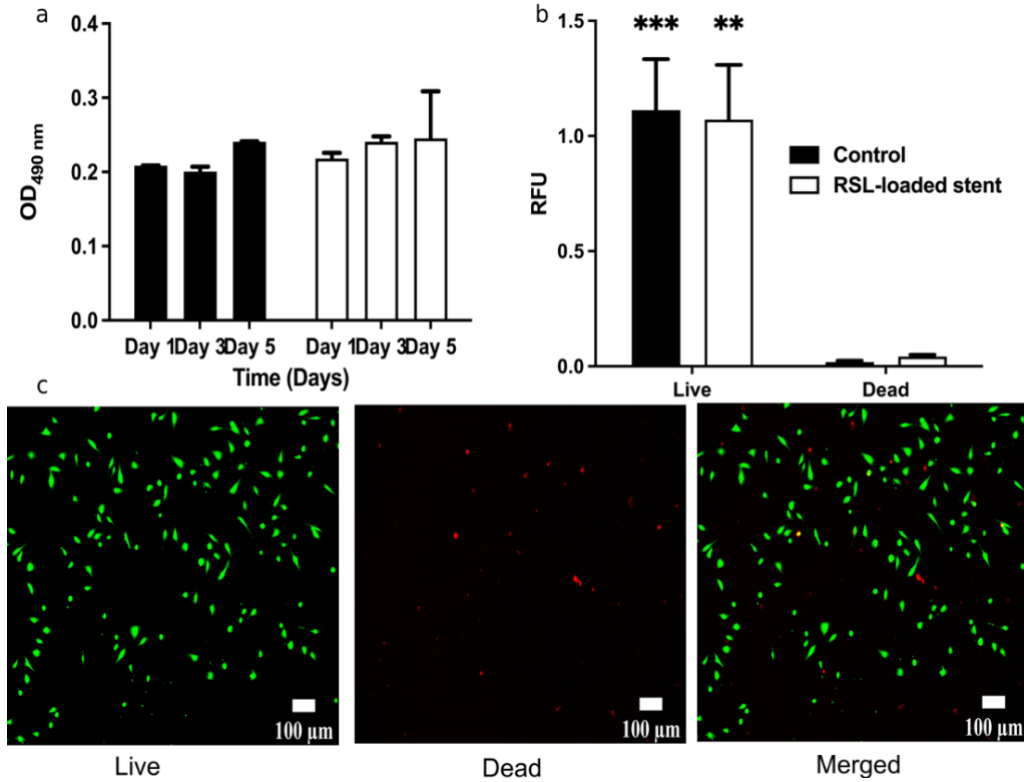
Figure 21. Effects of 3D-printed stents on cell viability (a) Effect of 3D stent samples containing RSL on the viability of HUVECs at varying exposure periods, (b) Relative fluorescence units (RFU) from the HUVECs treated with control and 3D stent samples containing RSL, and (d) Fluorescent images of HUVECs denoting live (green) and dead (red) fluorescence. The data are presented as mean±SEM (N= 3). **p<0.01 and ***p<0.001 based on Student's *t*-test.

Effects of 3D-Printed Stents on Cell Apoptosis

Programmed cell death was evaluated by Annexin/PI staining solutions. As shown in Figures 22a and 22b, the H_2O_2-treated group (*i.e.*, the positive control) had $31.9\pm1.1\%$ of apoptotic cells, while the group exposed to 3D stents reduced the apoptotic cells to $7.3\pm1.5\%$, achieving a five-fold decrease in cell apoptosis. We found that the H_2O_2-induced oxidative stress enhanced the population of apoptotic cells, whereas pre-treatment with RSL produced cardio-protective activities on the HUVECs. 3D stents containing RSL displayed protective effects against cell death and may have major benefits to cardiovascular therapy in the future.
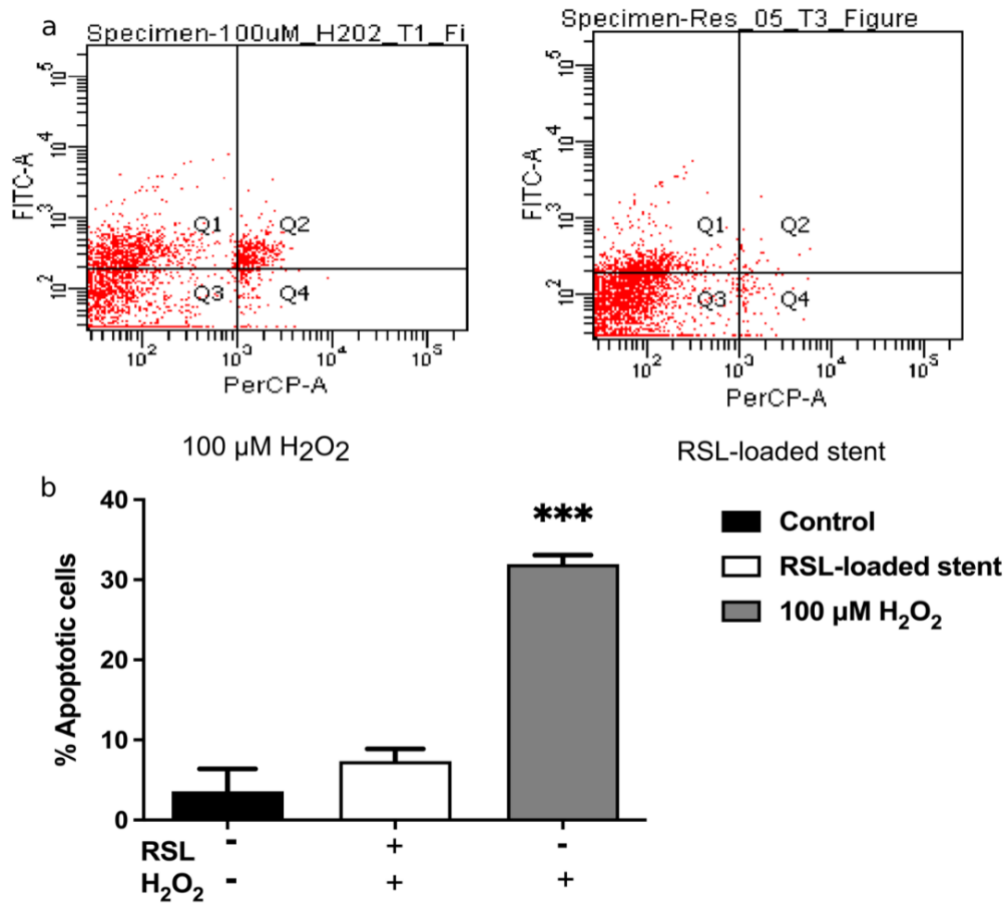
Figure 22. Effects of 3D-printed stents on cell apoptosis (a) Apoptosis of HUVECs after 24 hr incubation with 3D stents containing RSL. The y-axis indicates Annexin-V, whereas the x-axis indicates PI. Q1: the cells in early apoptosis; Q2: the dead/apoptotic cells; Q3: the live cells and Q4: Necrosis and (b) Plot indicating 3D stent samples containing RSL. The data are presented as mean±SEM (N = 3). ***p<0.001 based on one-way (ANOVA) followed by Tukey's HSD analysis.

Assessment of Pro-inflammatory Cytokine Levels in Raw 264.7 Cells

As shown in Figure 23a, the amount of TNF-α released from the group treated with the samples of 3D stents containing RSL was significantly lower ($p<0.01$) as compared to the group treated with H_2O_2 alone. This study demonstrated that the RSL-eluting 3D-printed stent could down-regulate the pro-inflammatory cytokine secretion and can be further explored for the treatment against atherosclerosis.

Effects of 3D-Printed Stents on Intracellular Reactive Oxygen Species (ROS) Levels

As an excessive production of ROS could lead to oxidative stress conditions in most cells, the levels of intracellular ROS were examined using DCFDA dye. As shown in Figure 23b and 23c, the group treated with only H_2O_2 (100 µM for 24 hr) had significantly ($p<0.05$) higher fluorescence intensity (8.3 ± 1.0 RFU) than those treated with both RSL containing 3D stent and H_2O_2 (5.0 ± 1.0 RFU), indicating that RSL-eluting stent could attenuate H_2O_2-induced ROS and help recover endothelial cell functions.
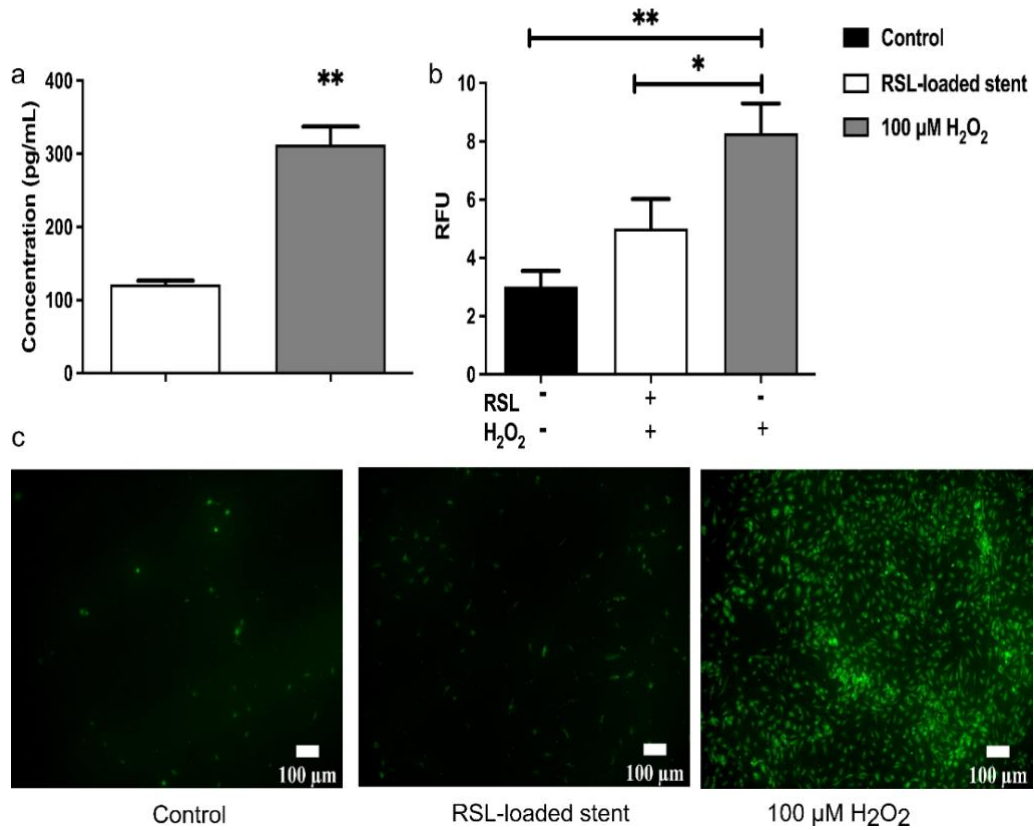
Figure 23. Effects of 3D-printed stents on the intracellular reactive oxygen species (ROS) levels (a) TNF-α expression in Raw 264.7 cells, (b) Quantification of fluorescence from DCFDA assay using ImageJ software, and (c) Representative fluorescent images of HUVECs stained with DCFDA. The data are presented as mean±SEM (N= 3). (a) **p<0.01 based unpaired Student's *t*-test. (b) *p<0.05 and **p<0.01 based on one-way (ANOVA) followed by Tukey's HSD analysis.

3.4. Conclusion

This study outlined the development and characterization of a hydrogel-based 3D-printed cardiovascular stent to improve endothelial cell functions. The hydrogel composites possessed desired shear-thinning property which is a pre-requisite for 3D printability. The addition of MeGO into hydrogel composites improved stiffness, produced stable printed structures, and minimized the changes in the volume of the stents. An enhanced NO production from RSL-loaded 3D-printed stents lead to suppression of platelet aggression and adhesion. These stents exerted no cytotoxic effects on HUVECs and lowered TNF-α expression levels. In conclusion, 3D-printed stents were biocompatible and displayed great potential in recovering endothelial function.

CHAPTER 4

ASSESSMENT OF BIOCOMPATBAILITY OF 3D-PRINTED CARDIOVASCULAR

STENTS

4.1. Rationale

Coronary artery disease (CAD) is caused by blockage of coronary arteries owing to plaque buildup [119,132] stemming from oxidation and conversion of LDL to oxidized-LDL (ox-LDL) in the presence of ROS [133]. The consumption of ox-LDL by macrophages results in lipid infiltration and extracellular lipid expansion, leading to plaque instability [134,135]. The presence of intrinsic inflammation could alter the physiological function of the leukocytes by attenuating the expression of ATP-binding cassette, sub-family A (ABCA1), a key transporter in cholesterol efflux [136,137] promoting the progression of CAD [138].

Cardiovascular stents have been used to treat narrowed or blocked coronary arteries resulting from CAD [26]. Biodegradable polymeric materials are promising candidates in the manufacture of stents, due to their nanoporous structure that can facilitate systemic connection of the stents with the vascular network of the patients [139]. In our previous work, poly(2-hydroxyethyl methacrylate) (pHEMA) was utilized as a base polymer for 3D printing of biodegradable stents [140]. The addition of MeGO into the pHEMA-based printing ink enhanced the mechanical strength of the biodegradable stents which, when loaded with the drug RSL, demonstrated excellent performance in recovering endothelial cell function [140].

The 3D printing strategy can be applied to provide patients with customized biomedical devices based on their individual physiological conditions. The active ingredient/drug in the 3D-printed device should be able to elicit the necessary therapeutic effects in the host with little/no immune reaction. Even though it has been previously reported that pHEMA is a photo-

curable polymer with excellent biocompatibility, there is lack of information about toxicity when it is applied to biomedical devices including cardiovascular stents [6,141,142].

The biocompatibility of raw materials used in biomedical devices could be dependent on the concentration of the active material, physical properties, and the duration of the treatment [143,144]. The toxicological assessment of the biomedical products including 3D-printed cardiovascular stents could provide critical insights into post-treatment strategies to minimize the material-related adverse effects and reduce the associated risks in patients during their clinical application [145], subsequently facilitating the regulatory pre-approval process [146].

Several studies have evaluated the biocompatibility of the 3D-printed products through cell culture and/or zebrafish embryo-based assays [147–150]. As an adult zebrafish can produce over 100 eggs in a day and their transparent nature aids in reliable high-throughput screening of chemical toxicity [151], zebrafish embryos have been frequently utilized for the assessment of developmental toxicology in the field of drug discovery [152,153].

This study aimed to evaluate the biocompatibility of the 3D-printed cardiovascular stents using zebrafish embryos. It has been previously demonstrated that the 3D-printed parts, produced from STL and the fused-deposition method (FDM), could induce phenotypic changes in zebrafish embryos [154,155]. In this study, the effects of RSL-loaded 3D stents on the viability of endothelial cells, NO production from Raw 264.7 cells, and downregulation of oxidative stress in zebrafish larvae were evaluated using MTS, Griess, and DCFDA assays, respectively. To evaluate the effects of RSL-loaded 3D stents on the pro-inflammatory cytokine expression in zebrafish larvae was examined using reverse transcription-quantitative polymerase chain reaction (RT-qPCR). The endpoints of toxicity of the RSL-loaded 3D stents

were examined based on the appearance of developmental defects in the zebrafish larvae.

The developmental abnormalities due to oxidative stress were evaluated using zebrafish embryos treated with RSL-loaded 3D stents (0.5, 1, and 2 mM) in the presence of H_2O_2 (3 mM). Subsequently, zebrafish embryos were evaluated for their survival, hatching rate, and developmental defects (reduced length, yolk sac edema, pericardial edema, and spinal flexure) at 72 hours post fertilization (hpf). The outcomes of this study can help establish safe and effective conditions by selecting optimal doses of RSL to avoid potent cytotoxicity of RSL-loaded 3D stents during their clinical application.

4.2. Materials and Methods

Materials

Lipopolysaccharides (LPS), dimethyl sulfoxide (DMSO), and 2′,7′-dichlorofluorescin diacetate (DCFDA) were purchased from Sigma-Aldrich (St. Louis, MO). Ethylene glycol dimethacrylate (EGDMA) and resveratrol (RSL) were purchased from TCI® America, Inc. (Portland, OR). Raw 264.7 cells (mouse macrophages), Dulbecco's modified eagle's medium (DMEM), and penicillin-streptomycin solution were purchased from ATCC (Manassas, VA). Fetal bovine serum (FBS) was purchased from Atlantic Biologicals Corp. (Atlanta, GA). Human umbilical vein endothelial cells (HUVECs), endothelial cell basal medium-2 (EBM-2), and endothelial cell growth medium BulletKit were purchased from Lonza (Mapleton, IL). All the reagents and solvents were of analytical grade.

3D Printing Process of Cardiovascular Stents

The RSL-loaded 3D stents (pHEMA-0.35MeGO) were fabricated as described in the previous chapter. Cardiovascular stents (4 mm diameter and 6 mm height) loaded with varying

concentrations of RSL (0.5, 1, and 2 mM) were printed using an extrusion-based 3D printer as previously described and used for further studies.

Effects of the ox-LDL on HUVEC Viability

To evaluate the effects of ox-LDL on the viability of HUVECs, *in vitro* cell viability studies were conducted using the MTS assay. The viability of HUVECs (passage 2-5) upon exposure to ox-LDL (100 μg/mL) in the presence of 3D-printed stents (4 mm diameter and 6 mm length) loaded with RSL (~1 mM) was examined by cell proliferation assay (Promega®, San Luis Obispo, CA).

Briefly, each well was seeded with 10,000 cells (100 µL) and incubated overnight. On the following day, the media was replaced with 100 µL of fresh media and incubated at 37 °C with 5% CO_2. A culture medium without RSL-loaded 3D stents was used as the negative control. After the pre-determined time intervals, MTS solution (20 µL) was added to each sample, and absorbance values were recorded at 490 nm using a multimode detector (Molecular Devices® Spectra max 190, Hampton, NH, USA).

Assessment of the Amount of NO in Cultured Cells

The amount of NO, produced from Raw 264.7 cells upon exposure to RSL-loaded 3D stents (~1 mM), was quantified as an index of defense mechanism against damage to vascular endothelial tissues using the Griess assay [119].

Briefly, each well was seeded with 10,000 cells (100 µL) and loaded with RSL-loaded 3D stents. Each well was replaced with the fresh media on the following day and the cells were incubated for 24 hr. After 24 hr, 100 µL media in the plate was transferred to a fresh 96-well

plate and 50 µL of 2% sulfanilamide solution and 50 µL of 0.2%w/v NED solution were added to each sample. The absorbance was measured at 550 nm using a multimode detector (Molecular Devices® Spectra max 190, Hampton, NH, USA).

Assessment of the Pro-inflammatory Cytokines

The yolk in zebrafish larvae were micro-injected with 2 nL each of 0.01 M PBS pH 7.4 and LPS (0.5 mg/mL) at 48 hpf [156]. Total RNA was extracted from the larvae at 72 hpf using TRIzol reagent (Invitrogen®, Carlsbad, CA) according to the manufacturer's instructions. Primers were purchased from Integrated DNA Technologies (IDT®, Coralville, IA). The mRNA expression of pro-inflammatory cytokines (TNF- α and IL-1β) were studied using zebrafish specific forward and reverse primer sequences (5'-3'); ATGGATGAGGAAATCGCTG, ATGCCAACCATCACTCCCTG for β-actin, GCTG GATCTTCAAAGTCGGGTGTA, TGTGAGTCTCAGCACACTTCCATC for TNF-α, and TGGACTTCGCAGCACAAAATG, GTTCACTTCACGCTCTTGGATG for IL-1β [156].

Raw 264.7 cells ($1x10^6$ cells) were seeded in a 6-well plate and subsequently treated with RSL-loaded 3D stent samples along with 10 ng/mL of LPS for 24 hr. The samples without treatment served as negative controls. The total RNA from macrophages was extracted from each group and relevant expressions were measured using macrophage-specific forward and reverse primer sequences (5'-3'); AGAGGGAAATCGTGCGTGAC, CAATAGTGATGACCTGGCCGT for β-actin, GACCCTCACACTCAGATCATCTTCT, CCTCCACTTGGTGGTTTGCT for TNF-α, and GTATGACTCTACCCACGGCAAGT, TTCCCGTTGATGACCAGCTT for IL-1β. Reverse transcription reactions were carried out according to the manufacturer's protocol for iTaq Universal one-step RT-qPCR kit (Bio-Rad®,

Hercules, CA) with an initial denaturation at 95 °C for 5 min, 95 °C for 10 sec, and 60 °C for 30 sec. All reactions were performed in triplicate for 40 cycles using a CFX96 Dx real-time PCR system (Bio-Rad®, Hercules, CA).

Assessment of Oxidative Stress in the Zebrafish Model

The intracellular ROS levels in zebrafish larvae were examined for the assessment of the oxidative stress. Approximately, 30 embryos (48 hpf old) were incubated with the RSL-loaded 3D stents (~1 mM) in the presence of 100 µM to 3 mM H_2O_2 for 24 hr. After incubation, the embryos were treated with 20 µM of DCFDA dye at 37 °C for 20 min. The fluorescent images were collected and quantified using a DCFDA fluorescent probe as previously described.

Zebrafish Animal Husbandry and Experimental Design

All the experiments were performed on embryos collected from natural crosses of adult wild-type *AB strain zebrafish (16-18 months old). In-house environmental study facilities (14 hr light and 10 hr dark cycle at 28 ± 0.5 °C) were used to conduct all the experiments [157,158]. All the animal procedures were carried out in accordance with the Institutional Animal Care and Use Committee (IACUC, University of Missouri-Kansas City #1707-02). For each set of experiments, approximately 10 embryos per condition were randomly selected and placed into each well of a 6-well plate containing 5 mL of E3 media (0.99 mM $MgSO_4 \cdot 7H_2O$ 0.15 mM KH_2PO_4, 0.04 mM Na_2HPO_4, 1.30 mM $CaCl_2 \cdot 2H_2O$, 0.50 mM KCl, and 14.97 mM NaCl).

Embryos were either exposed to varying concentrations of RSL (raw drug: 10 µM, 50 µM, 100 µM, and 150 µM) or RSL-loaded 3D stents (containing 0.5, 1, and 2 RSL) under

different oxidative stress conditions from 4 to 72 hpf (hours post-fertilization). The embryos exposed to 0.15%v/v DMSO were used as a control. For the assessment of developmental toxicity, embryos were treated with 1 mM RSL-loaded 3D stents in the presence of 3 mM H_2O_2. Embryos were examined for their survival, hatching rate, and developmental defects (reduced length, yolk sac edema, pericardial edema, and spinal flexure) at 72 hpf. Dead embryos, if any, were counted and removed from the plate every 24 hr before replacing the wells fresh E3 medium (containing the appropriate control or experimental treatment).

To prevent the intrinsic movement of zebrafish larvae during fluorescent imaging, 0.2%w/v tricaine (Western® Chemical Inc, Redmond, NE) was added prior to image acquisition. Images were collected using a Zeiss Axio Zoom V.16 fluorescent dissecting microscope with a Zeiss Axiocam 506 color camera and Zen software. Image processing and analysis were conducted using FIJI ImageJ software [159]. After the imaging processes, all larvae were euthanized according to the established procedures.

<u>Statistical Analysis</u>

All experiments were carried out in triplicate unless otherwise specified. The data were expressed as mean±SEM. One-way analysis of variance (ANOVA) followed by Tukey's HSD analysis was used to compare multiple groups. All statistical analyses were carried out using SPSS® software (IBM® Corp. Armonk, NY). p-values represent different levels of significance: *$p < 0.05$, **$p < 0.01$, and ***$p < 0.001$.

4.3. Results and Discussion

Assessment of Ox-LDL on HUVECs

Ox-LDL initiates damage of endothelial cells, leading to the activation of various signaling pathways involved in the development of CAD [160]. To investigate the effect of the RSL-loaded 3D stent (~1 mM) on viability *in vitro*, endothelial cells were treated with 100 μg/mL of ox-LDL. As shown in Figure 24a, treatment with ox-LDL alone significantly lowered the viability of endothelial cells (p<0.001). On the contrary, exposure to the RSL-loaded stents resulted in good viability of HUVECs in presence of ox-LDL, demonstrating the protective action of RSL-loaded stent against ox-LDL-induced endothelial cell damage.

The findings from this study are in good agreement with those from previously published reports, in which RSL treatment upregulated the expression of sirtuin 1 (SIRT1) and promoted the degradation of ox-LDL via the autophagy-lysosomal pathway in HUVECs [161,162]. It was recently demonstrated that RSL has inhibitory effects against endothelial dysfunction, suggesting its potential application in the treatment of CAD [163].

Assessment of NO produced from Raw 264.7 Cells

The levels of NO produced by macrophages were examined to assess the anti-inflammatory activity of RSL-loaded 3D stents. NO is a short-lived gaseous molecule with multiple functional properties, such as neurotransmission and vasodilation, and it acts as one of the primary effectors against inflection [164]. Excessive production of NO is indicative of a defense mechanism against vascular endothelial tissue damage [165].

The addition of LPS (10 μg/mL), a pro-inflammatory agent [166], produced a significantly greater amount (p<0.001) of NO (82.4±1.2 μM) in Raw 264.7 cells than the group

treated with RSL-loaded 3D stents (52.8±0.4 µM), whose levels were close to those of the control group (51.9±0.8 µM) (Figure 24b). These results demonstrated that the RSL-loaded 3D stents exerted an anti-inflammatory action on macrophages. The results of this study are in a good agreement with those from the previous study in which RSL significantly lowered the expression of inducible NO synthase (iNOS) at inflammation sites through downregulation of nuclear factor-kB (NF-kB) activation [167].
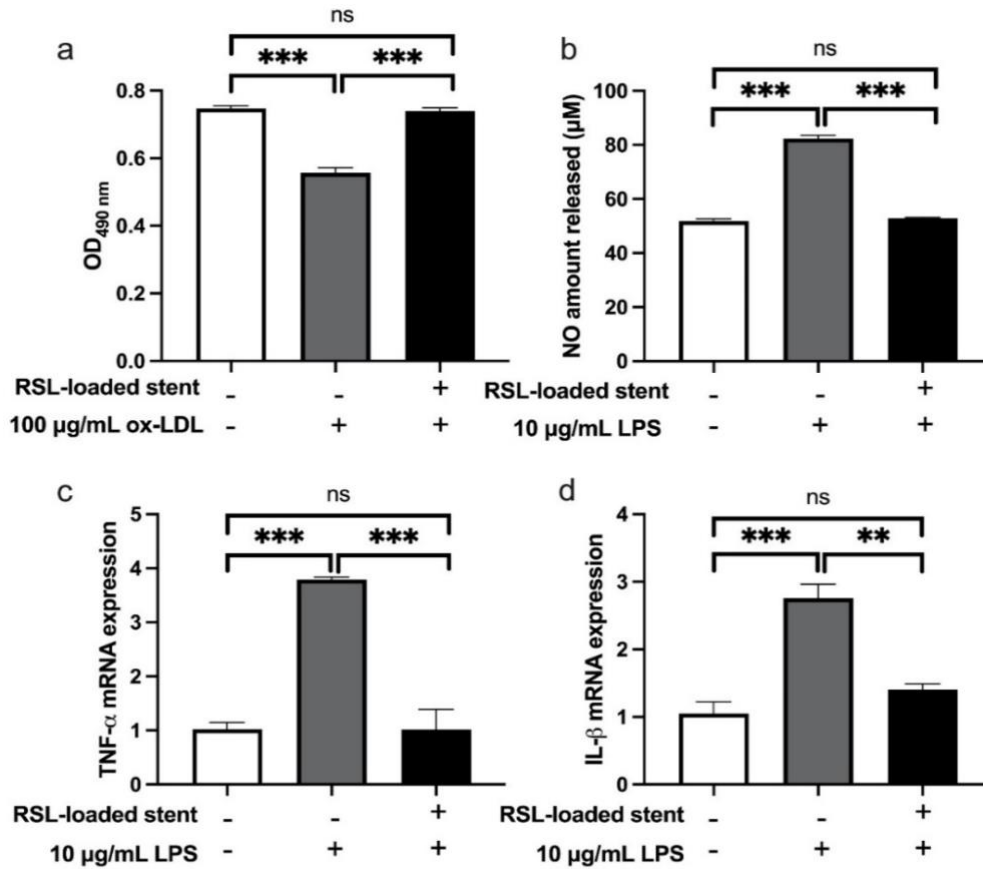
Figure 24. Effects of RSL-loaded 3D stents on a) the viability of HUVECs in presence of ox-LDL, (b) the production of NO in Raw 264.7 cells in presence of LPS (10 μg/mL), (c) TNF-α expression in Raw 264.7 cells in presence of LPS (10 μg/mL), and (d) IL-1β expression in Raw 264.7 cells in presence of LPS (10 μg/mL). The data are presented as mean±SEM (N= 3). ***p<0.001 based on one-way (ANOVA) followed by Tukey's HSD analysis.

<u>Assessment of Pro-inflammatory Cytokines (RT-PCR) Studies</u>

As shown in Figures 24c and 24d, the levels of TNF-α and IL-β expressed by Raw 264.7 cells in the group treated with RSL-loaded 3D stents (1.0±0.4 fold and 1.4±0.1 fold) were significantly lower (p<0.001) than those from the LPS alone treatment group (3.8±0.1 fold and 2.8±0.2 fold). The results of this study demonstrated that the RSL-loaded 3D stents could exert anti-inflammatory activity via downregulation of the pro-inflammatory cytokine secretion.

To further examine the anti-inflammatory effects of the RSL-loaded stents, an acute-inflammatory model induced in zebrafish larvae at 48 hpf was examined (Figure 25c). As shown in Figure 25a, TNF-α expression levels were significantly upregulated in the LPS-injected larvae (8.1±2.3 fold) as compared to the PBS-injected larvae (3.1±0.4 fold). On the contrary, the LPS-injected larvae incubated with RSL-loaded 3D stents significantly lowered the mRNA expression (1.8±0.8 fold) (Figure 25a).

A similar trend was observed in IL-1β expression (Figure 25b) between the control, LPS-injected, PBS-injected, and RSL-loaded 3D stent groups. The LPS-injected larvae incubated with the RSL-loaded 3D stent significantly (p<0.01) downregulated IL-1β expression from 23.8±3.8 to 1.9±0.2 fold, demonstrating the anti-inflammatory activity of RSL-loaded 3D stents that supports its application in the treatment of CAD.
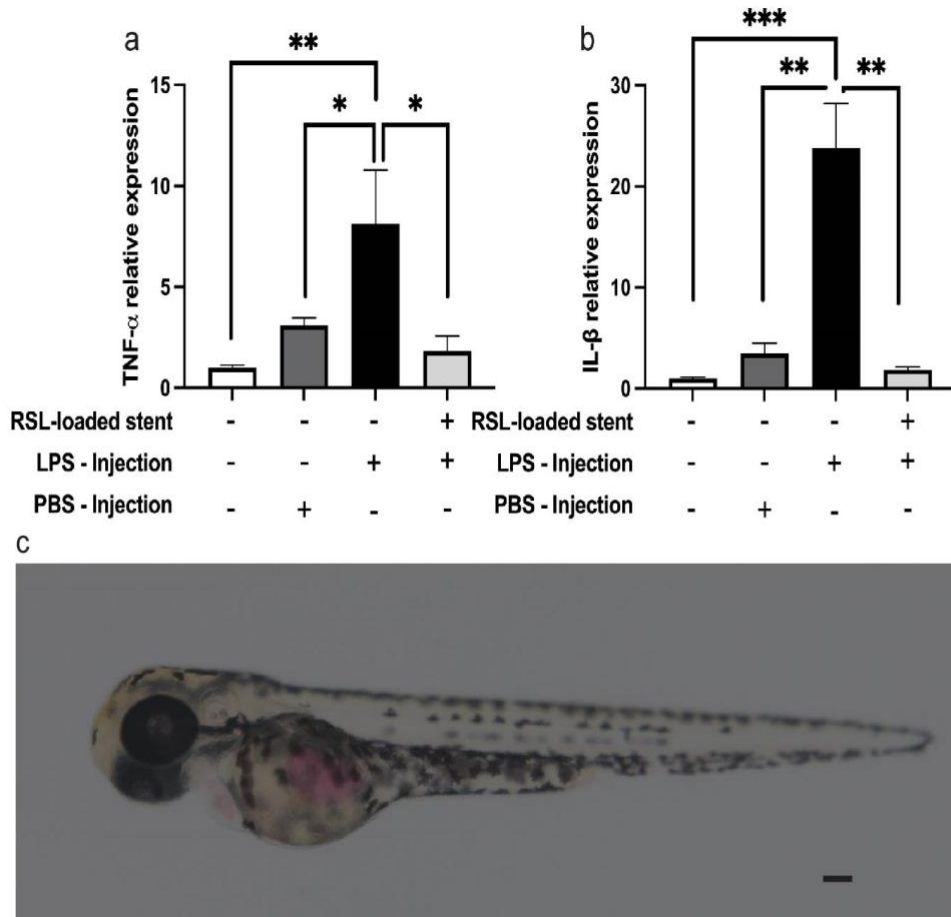
Figure 25. Assessment of (a) TNF-α and (b) IL-1β expression in zebrafish larvae, and (c) Zebrafish larvae injected with 1 nLof 5% solution of rhodamine dextran in 0.2 M KCl in the yolk sac. The data are presented as mean±SEM (n=10 embryos per condition. N=3 replicates per experiment). Scale bar represents 100 µm. *p<0.05, **p<0.01, and ***p<0.001 based on one-way (ANOVA) followed by Tukey's HSD analysis.

Assessment of Survival and Hatching Rate of Zebrafish Embryos

To evaluate the dose-dependent toxicity of the RSL-loaded 3D stents, zebrafish embryos were exposed to prototype stents (4 mm diameter and 6 mm length) which were loaded with three doses of RSL (0.5, 1, and 2 mM). The loading doses of RSL were selected based on the amount of RSL released from the hydrogel-based formulations and its therapeutic levels for the endothelial function recovery [140]. Subsequently, a multi-dose (0.5 mM, 1 mM, and 2 mM) experimental design was conducted to assess developmental abnormalities in the embryos.

The survival rate of zebrafish is considered as the critical marker of lethal toxicity. It was found that stents with 0.5 mM RSL (not included in Figure 26) and 1 mM RSL doses exerted no mortality during the developmental stages, but stents with 2 mM dose showed a slightly lower survival rate of zebrafish (93.3±3.3%) (Figure 26a).

To assess the initial developmental status of the zebrafish embryos, the number of embryos that successfully hatched from their protective chorions by 72 hpf were examined [168]. The embryos were incubated with the stent containing 0.5 mM (data not shown), 1 mM, and 2 mM RSL, respectively, for 72 hr and the corresponding hatching rates were determined. At 48 hpf, 80.0±5.8% hatching rate was observed for the stent groups loaded with 1 mM RSL, while 33.7±18.3% for the stent groups loaded with 2 mM RSL. As shown in Figure 26b, the stent loaded with the higher dose of RSL significantly lowered the hatching rate when compared with the control group.
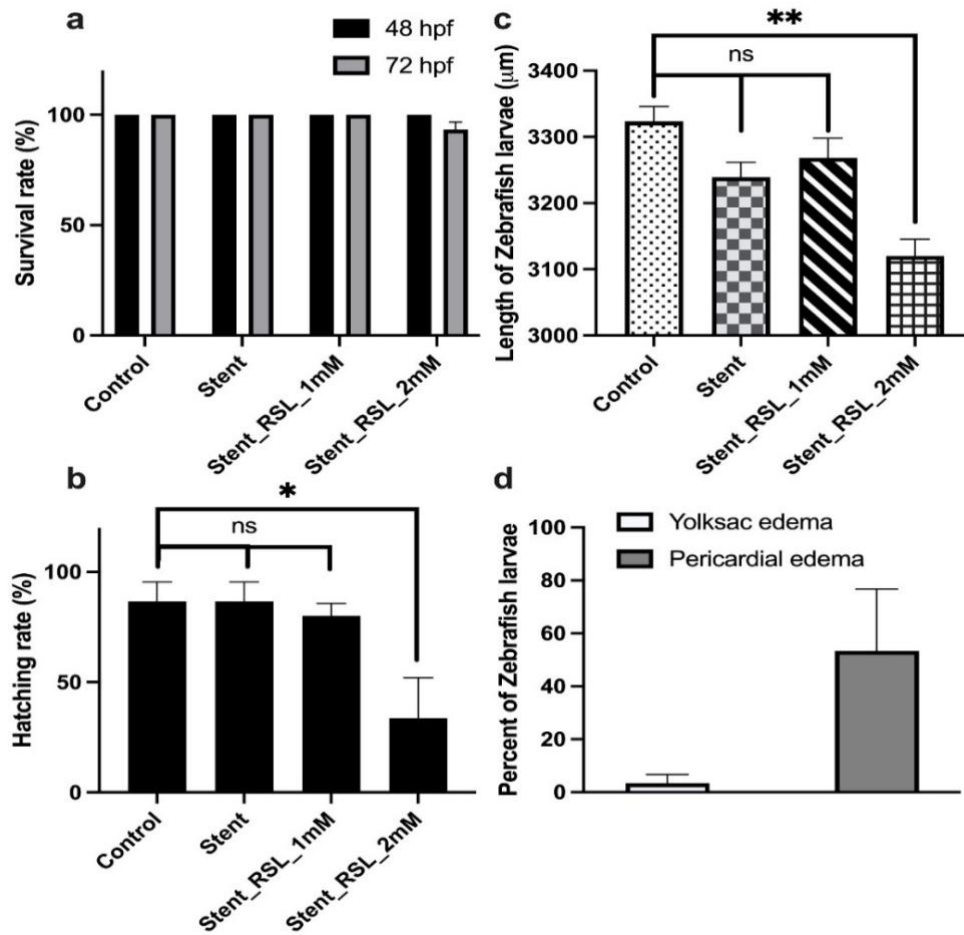
Figure 26. Assessment of biocompatibility of RSL-loaded 3D stents (1 mM and 2 mM of RSL) (a) Plot showing% survival rate over 72 hr, (b) Percentage hatching rate, (c) Length of the zebrafish larvae at 72 hpf, and (d) Percentage of zebrafish larvae displaying developmental abnormalities at 72 hpf. The data are presented as mean±SEM (n=10 embryos per condition, N=3 replicates per condition). *p<0.05 and **p<0.01 based on one-way (ANOVA) followed by Tukey's HSD analysis.

<u>Assessment of Developmental Abnormalities in Zebrafish Embryos</u>

The fish embryo toxicity (FET) studies were adapted as a suitable model to assess the toxicity of RSL-loaded 3D stents. As shown in Figures 27 and 28, the cardiovascular system is fully established in zebrafish embryos during the first 3 days, and heart beats and blood flow can be easily visualized by 72 hpf [169,170].

To assess any developmental abnormalities potentially induced by RSL-loaded 3D stents, 4 hpf wild-type zebrafish embryos placed in a standard 6-well plate at 28 °C containing 5 mL each of E3 media were exposed to RSL-loaded 3D stents. Developmental defects, such as hatching ratio, survival rate, yolk sac edema, pericardial edema, lack of somite formation, body length, malformation of head, and spine flexure were examined in the embryos at 72 hpf.

There were no differences in developmental abnormalities produced by the control group and stents with 0.5 mM and 1 mM RSL. However, at 72 hpf, mild to moderate developmental abnormalities were detected in embryos treated with the stent loaded with RSL (2 mM). As shown in Figure 26c, the length of zebrafish larvae decreased from 3323.5±22.2 μm to 3120.1±25.3 μm, as the dose of RSL in the stent increased from 1 to 2 mM. In addition, as shown in Figure 26d, pericardial and yolk sac edemas were displayed in zebrafish embryos for the stent groups loaded with 2 mM RSL (53.3±23.3% for 2 mL vs. 3.3±3.3% for 1 mL). Therefore, the dose of the RSL should be closely monitored to prevent any abnormal defects in the clinical applications.
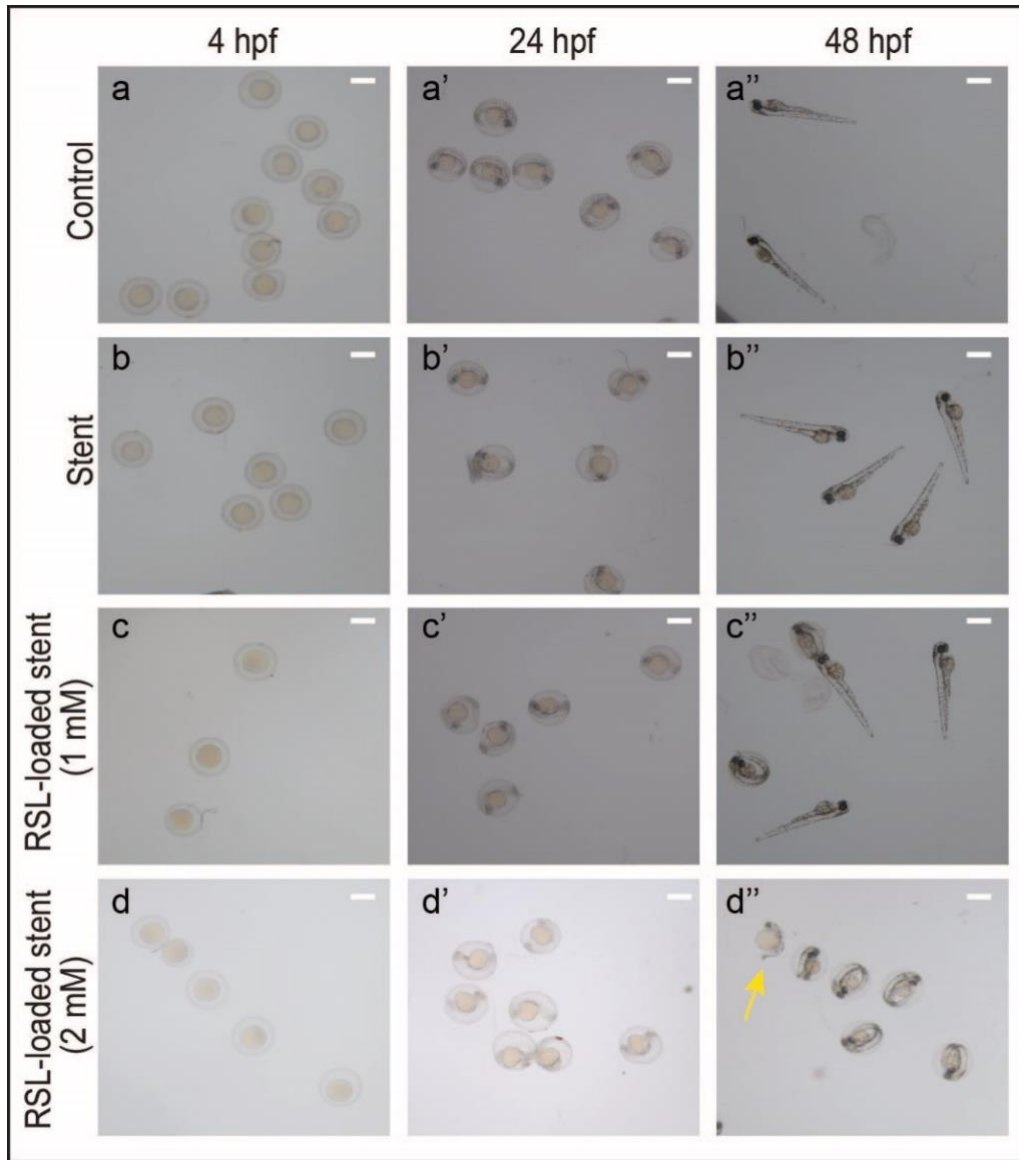
Figure 27. Microscopic images of zebrafish from embryotic to larval stages (4-48 hpf). (a-a'')
Control embryos, (b-b'') Embryos incubated with 3D stents, (c-c'') Embryos incubated with
RSL-loaded 3D stents (1 mM), and (d-d'') Embryos incubated with RSL-loaded 3D stents (2
mM) show instances of yolksac edema (yellow arrow). Scale bar represents 500 µm.
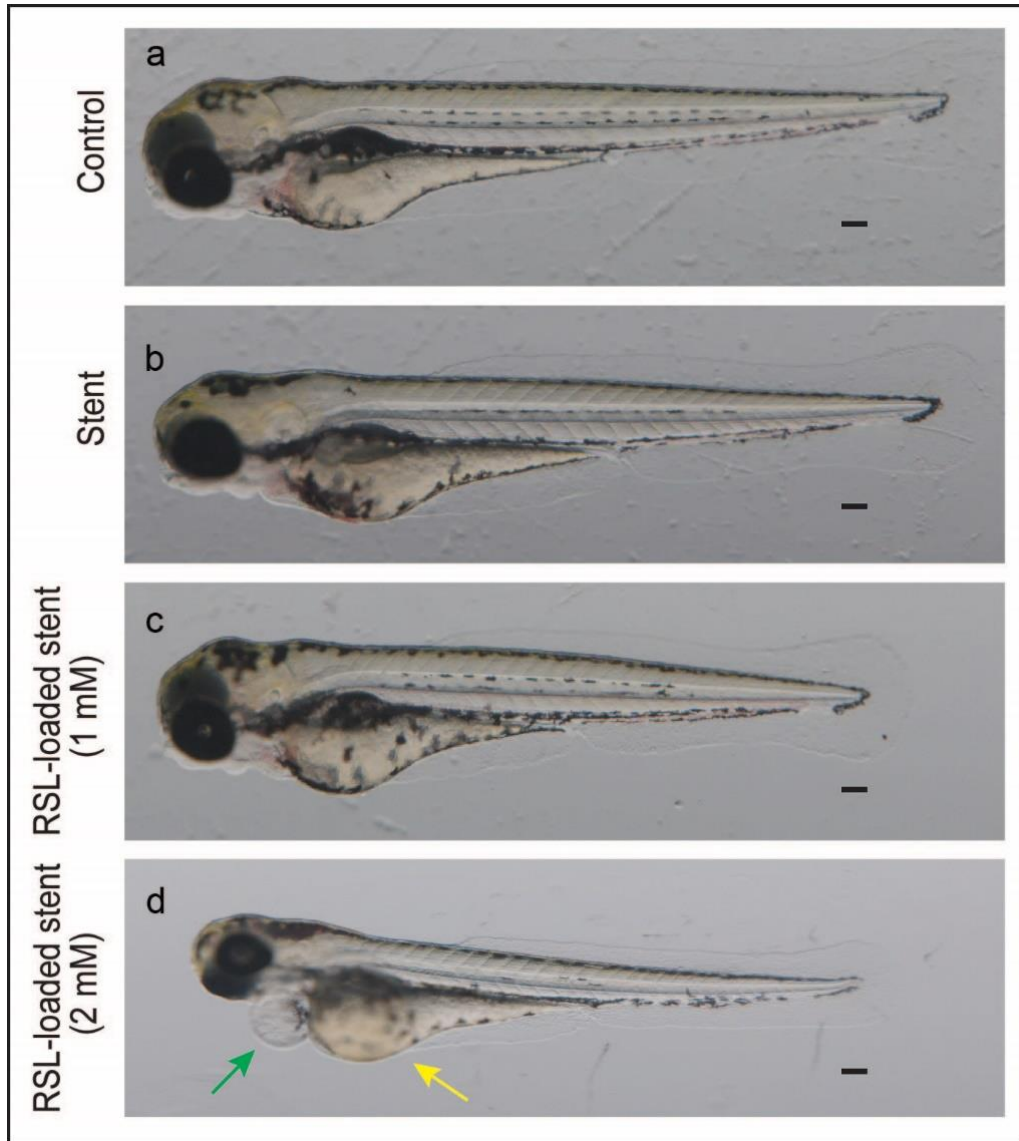
Figure 28. Microscopic images of zebrafish larvae (72 hpf). (a) Control embryos, (b) Embryos incubated with 3D stents, (c) Embryos incubated with RSL-loaded 3D stents (1 mM), and (d) Embryos incubated with RSL-loaded 3D stents (2 mM) displaying instances of pericardial (green arrow) and yolksac (yellow arrow) edemas. Scale bar represents 100 µm.

Assessment of RSL Treatment on Zebrafish Embryos

The concentration of the active compound and the duration of exposure could be critical in assessing the developmental toxicity in zebrafish embryo. To address these issues, embryos were directly incubated with varying concentrations of RSL (10 µM, 50 µM, 100 µM, and 150 µM). RSL treatments in the embryos did not result in any deaths (*i.e.*, zero mortality) in any of the groups. However, the highest concentration (150 µM) displayed a delayed hatching rate with no developmental defects and resulted in similar length of the larvae (3288 ±12 µm) to those from the control groups (3223 ±32 µm). In addition, the highest concentration (150 µM) of RSL displayed the lowered hatching rate of 20±6% at 48 hr as shown in Figure 29.

There was no significant difference in the incidence of developmental toxicities in zebrafish embryos incubated with all the tested doses of RSL. It was previously found that cumulative amount of RSL released from the biodegradable stents was about 150 µM in 24 hr [140] that did not cause any developmental abnormalities nor distinctive mortality [171]. The results of this study support an idea that the embryo-based assessment could serve as a principal model to assess the toxicity of raw materials for biomedical devices in early developmental studies.
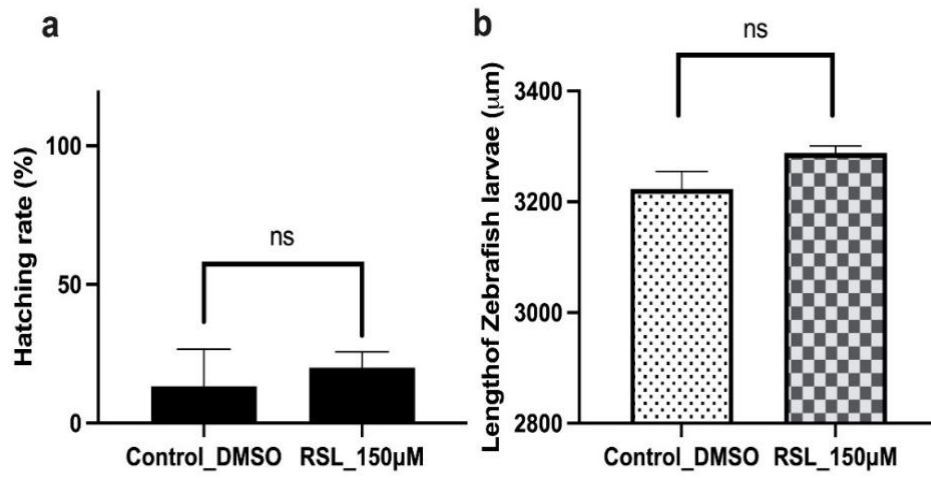
Figure 29. Assessment of RSL treatment on zebrafish embryos. (a) Plot showing the percentage of hatching rate and (b) Length of the zebrafish larvae at 72 hpf. The data are presented as mean±SEM (N=3).

<u>Assessment of Intracellular ROS in Zebrafish Model</u>

Oxidative stress is a major contributor to endothelial cell degeneration and the progression of inflammatory and immune responses in CAD [172]. To gain further insights into the effects of the RSL-loaded 3D stents on the levels of intracellular ROS, the oxidative stress in the zebrafish embryos was evaluated using the oxidation-indicator fluorescent dye, DCFDA. The zebrafish larvae were exposed to a wide range of H_2O_2 concentrations 0.1 mM, 0.5 mM, 1 mM, 2 mM, and 3 mM (data not shown for 0.5 mM to 3 mM) to examine their oxidative stress conditions.

As shown in Figure 30, the samples treated with 0.1 mM H_2O_2 displayed higher fluorescence intensity (0.38±0.07 RFU) than those treated with both RSL-loaded 3D stents and H_2O_2 (0.18±0.02 RFU $p<0.05$). The RSL-loaded 3D stent reduced the oxidative stress in the zebrafish embryos by attenuating the H_2O_2-induced ROS levels, improving the biocompatibility in the biological models. This study provides compelling evidence that the RSL-loaded 3D stent could be a promising therapeutic tool, and subsequent clinical trials are warranted to establish its potential efficacy and biocompatibility.
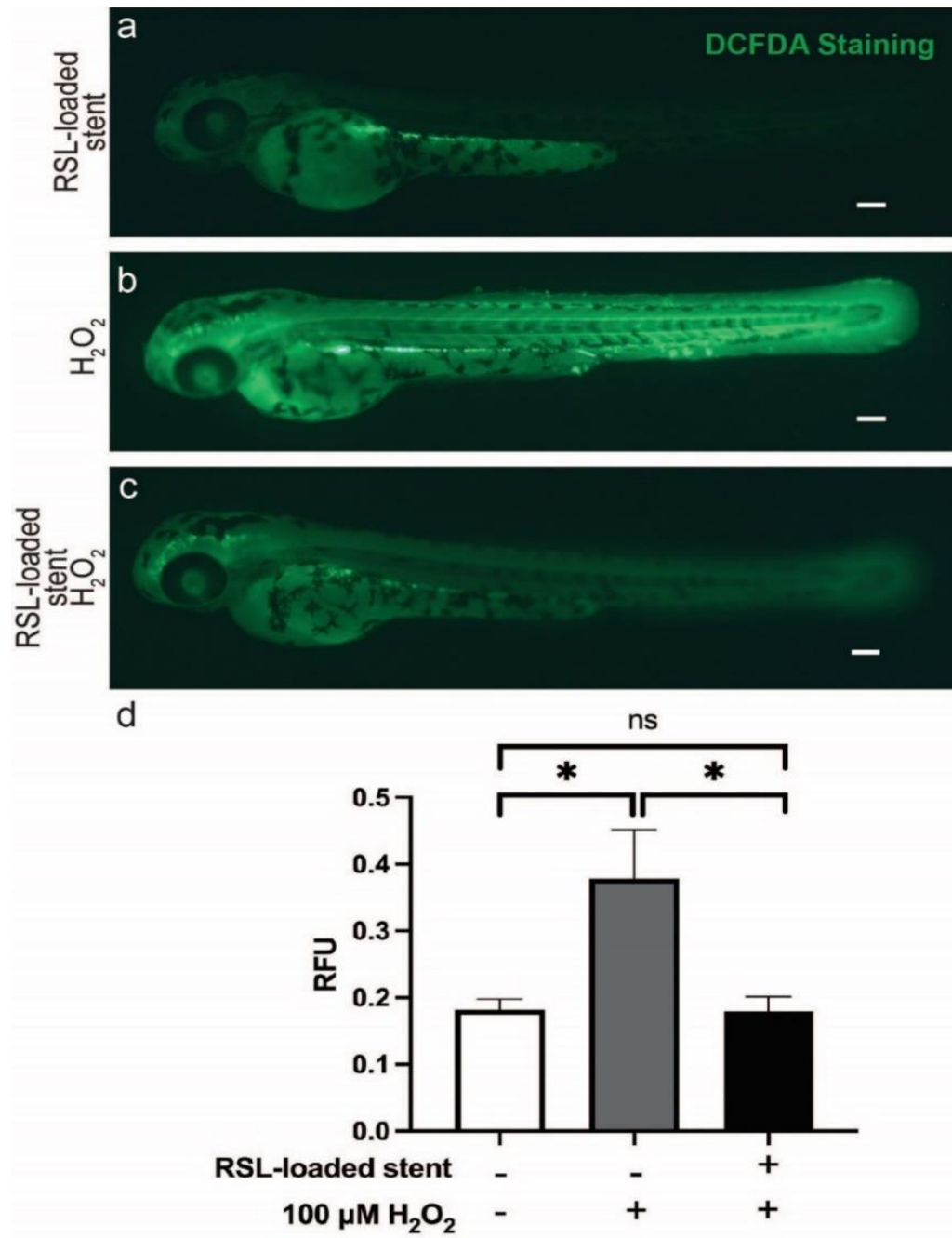
Figure 30. Fluorescent images of zebrafish larvae (72 hpf) stained with DCFDA. (a) Control embryo exposed to RSL-loaded 3D stent (1 mM), (b) 0.1 mM H_2O_2, and (c) 0.1 mM H_2O_2 in presence of RSL-loaded 3D stent (1 mM). The data are presented as mean±SEM (N= 3). Scale bar represents 100 µm. *p<0.05 based on one-way ANOVA followed by Tukey's HSD analysis.

Assessment of H_2O_2-Induced Developmental Defects in Zebrafish Embryos

To induce developmental defects in the zebrafish embryos, 4 hpf embryos were directly exposed to 3 mM of H_2O_2. Lower concentrations (0.1 mM, 0.5 mM, 1 mM, 2mM, and 2.5 mM) of H_2O_2 did not produce any developmental defects in zebrafish embryos (data not shown), however, when exposed to 3 mM H_2O_2 alone, significant abnormalities were observed at 72 hpf.

The treatment with 3 mM H_2O_2 did not induce mortality in the embryos (Figure 31a). As shown in Figure 31b, embryos incubated with 3 mM H_2O_2 for 72 hours had a lower hatching rate ($13.3\pm3.3\%$ at 48 hpf) as compared to those incubated with both 3 mM H_2O_2 and 1 mM RSL-loaded 3D stents ($43.3\pm8.8\%$). Embryonic length decreased, when exposed to 3 mM H_2O_2, but remained largely unchanged when incubated with 3 mM H_2O_2 in the presence of RSL-loaded 3D stents (2956 ± 35 μm to 3122 ± 30 μm, respectively) (Figure 31c).

Exposure to 3 mM H_2O_2 resulted in developmental abnormalities in embryos including yolk sac edema and spine flexure with $46.7\pm12.0\%$ ($p<0.05$) and $30.0\pm15.3\%$ ($p<0.05$), respectively, as shown in Figure 31d. However, embryos incubated with 3 mM H_2O_2 along with the RSL-loaded 3D stents displayed lower developmental abnormalities including pericardial edema from $20.0\pm10.0\%$ to $6.7\pm3.3\%$. The results of this study demonstrated that RSL-loaded 3D stents lowered H_2O_2-induced developmental abnormalities in the zebrafish embryos as shown in Figure 32.
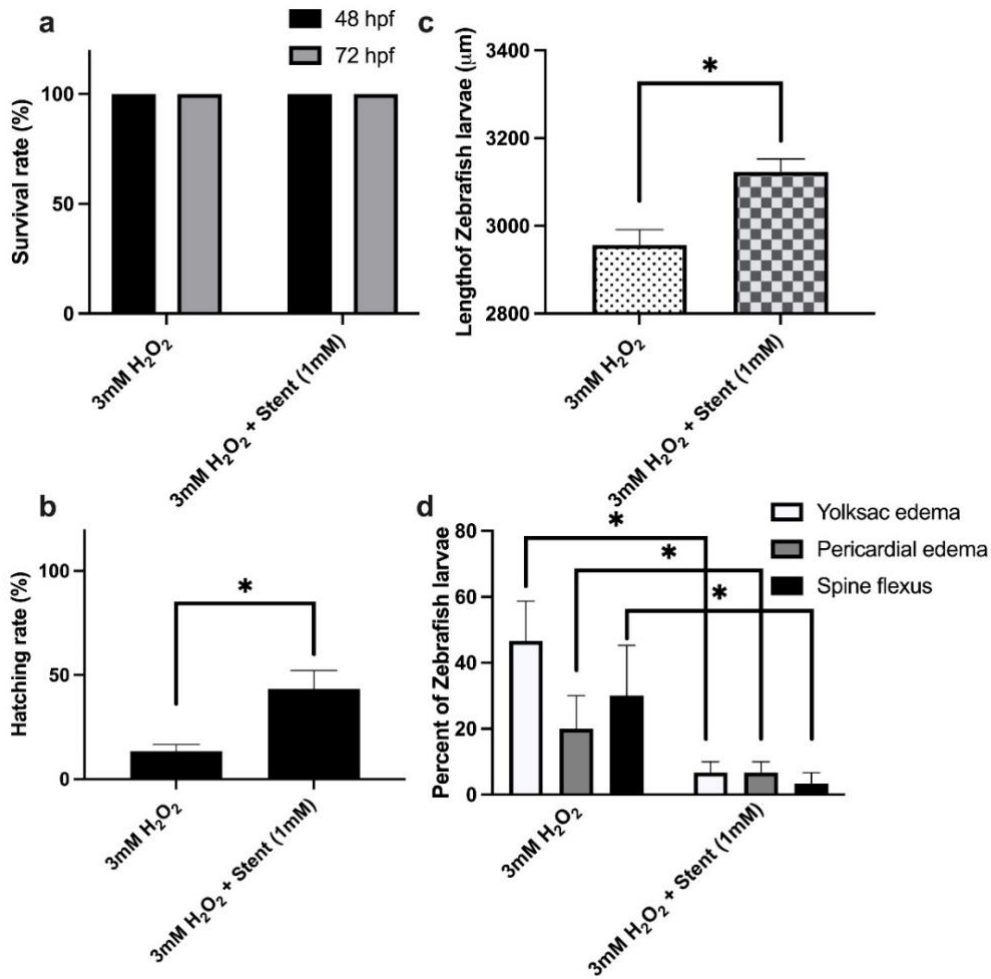
Figure 31. Evaluation of RSL-loaded 3D stents in presence of oxidative stress. (a) Plot showing the percentage survival rate over 72 hr, (b) percentage hatching rate, (c) length of the zebrafish larvae at 72 hpf, and (d) percentage of zebrafish larvae displaying developmental abnormalities at 72 hpf. The data are presented as mean±SEM (N=3) *p<0.05 based on one-way ANOVA followed by Tukey's HSD analysis.
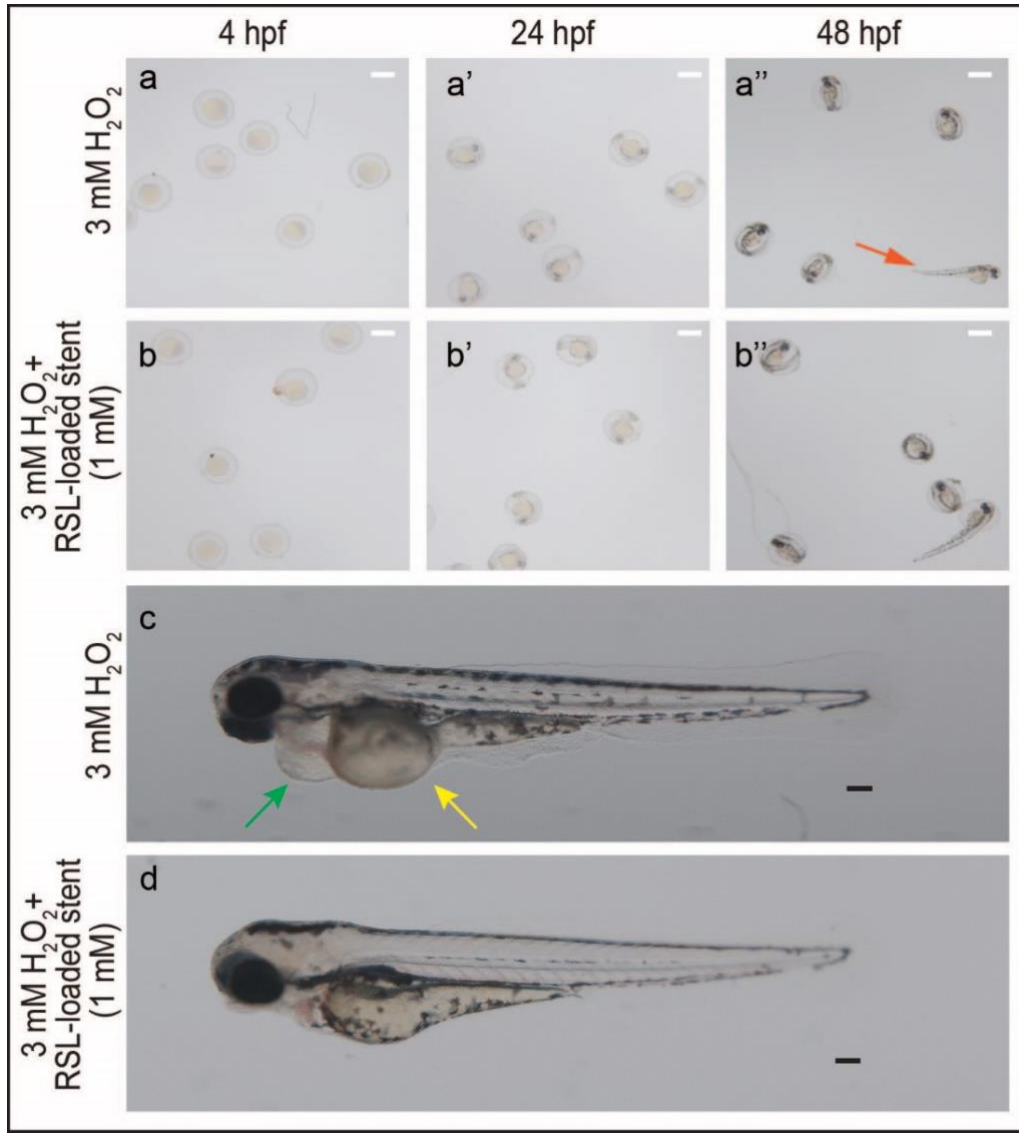
Figure 32. Microscopic images of zebrafish larvae (4-72 hpf). (a-a'') Embryos incubated with H_2O_2 (3 mM) show increased edema and spinal flexure (red arrow), (b-b'') Embryos incubated with H_2O_2 (3 mM) along with RSL-loaded 3D stents (1 mM) showed minimal developmental defects, (c) Embryos incubated with H_2O_2 (3 mM) showed instances of pericardial edema (green arrow), yolksac edema (yellow arrow), short heads, and smaller length, and (d) Embryos incubated with RSL-loaded 3D stents (1 mM) along with H_2O_2 (3 mM) showed normal development. Scale bar represents 500 µm (White) and 100 µm (Black).

4.4. Conclusion

The RSL-loaded 3D stents were developed and evaluated for biocompatibility using cell culture and zebrafish embryo models. The results of this study demonstrate that the RSL-loaded 3D stents did not exert any inflammatory responses in macrophages. The RSL-loaded 3D stents downregulated the secretion of the pro-inflammatory cytokines and lowered H_2O_2-induced developmental abnormalities in the zebrafish embryos. As RSL dose-dependent developmental abnormalities were displayed in the embryos, the dose of RSL in 3D stents should be closely monitored to avoid any potential cytotoxicity in clinical applications.

CHAPTER 5

SUMMARY AND RECOMENDATIONS

The current choice of treatment for CAD is implantation of permanent coronary artery stents loaded with a drug for short-term elution. The damaged blood vessels usually heal approximately within a year following stent implantation. Therefore, the metallic nature of the stent may no longer be necessary to maintain the integrity of the blood vessels once they have healed completely. In addition, the permanent nature of metallic stents may cause late-stage thrombosis, leading to re-blocking of the blood vessel [173,174]. The promising alternative to permanent stents could be biodegradable cardiovascular stents that would support arterial healing, degrade, and ultimately eliminate as metabolic byproducts. The research undertaken in this dissertation provides significant insights and approaches in personalized biodegradable stents for the advancement of CAD treatment.

The 3D printing approach demonstrated flexibility in terms of design, formulation optimization, and ensured consistent drug-loaded products that would be able to meet the needs of the patient. The identification of critical process parameters such as polymeric concentration, printing speed, printing height, and nozzle diameter facilitated necessary understanding of formulation and manufacturing variables on the stability and print quality of the 3D-printed products.

This research outlines the development and evaluation of 3D-printed stents that displayed optimum mechanical strength and necessary biodegradable properties. Hydrogel-based stent demonstrated improved swelling properties with incorporation of carbon nanoparticles. Surface modification with thiol group on alginate base polymer had a significant effect on the degradation rate. It was revealed that the comprehensive rheological assessments

of the hydrogel inks provided insights into necessary shear-thinning properties and viscoelastic nature of the hydrogel printing inks that were ideal for 3D printing applications.

The RSL-eluting cardiovascular stent protected endothelial cells from H_2O_2-induced oxidative stress conditions. The biocompatibility assays revealed that the RSL-eluting stent reduced the secretion of pro-inflammatory cytokines and lowered H_2O_2-induced developmental abnormalities in zebrafish embryos. This work could serve as a proof-of-concept to evaluate the RSL dose-dependent developmental toxicity in the embryos. The logical way forward would be to examine the potential causes of the observed developmental defects in embryos and approaches to minimize and/or delay them in long-term biocompatibility studies.

The future extension of this work would involve utilization of biomimetic platforms to study interactions between endothelial cells and 3D-printed scaffolds. The next phase would entail development of a novel fabrication method *via* 4D printing to produce carbon nanoparticle-based biomedical devices containing biosensors or theranostic agents. Such studies focus on the evaluation of new smart materials that can actively monitor of ox-LDL levels and expand their shape over time in response to environmental stimuli. Relevant information obtained from real-time data regarding the status of the stent implanted in patients may be used to improve clinical outcomes.

REFERENCES

[1] L. Ros, E.A.R. Al-Mahdi, J.M.M. Ruiz, J.L.Z. Gómez, Atherosclerosis, Medicine (Spain). 13 (2022) 2063–2070. https://doi.org/10.1016/j.med.2021.06.010.

[2] C.W. Tsao, A.W. Aday, Z.I. Almarzooq, A. Alonso, A.Z. Beaton, M.S. Bittencourt, A.K. Boehme, A.E. Buxton, A.P. Carson, Y. Commodore-Mensah, M.S.V. Elkind, K.R. Evenson, C. Eze-Nliam, J.F. Ferguson, G. Generoso, J.E. Ho, R. Kalani, S.S. Khan, B.M. Kissela, K.L. Knutson, D.A. Levine, T.T. Lewis, J. Liu, M.S. Loop, J. Ma, M.E. Mussolino, S.D. Navaneethan, A.M. Perak, R. Poudel, M. Rezk-Hanna, G.A. Roth, E.B. Schroeder, S.H. Shah, E.L. Thacker, L.B. Vanwagner, S.S. Virani, J.H. Voecks, N.Y. Wang, K. Yaffe, S.S. Martin, Heart Disease and Stroke Statistics-2022 Update: A Report from the American Heart Association, Circulation. 145 (2022) E153–E639. https://doi.org/10.1161/cir.0000000000001052.

[3] M.S. Chen, J.M. John, D.P. Chew, D.S. Lee, S.G. Ellis, D.L. Bhatt, Bare metal stent restenosis is not a benign clinical entity, Am Heart J. 151 (2006) 1260–1264. https://doi.org/10.1016/j.ahj.2005.08.011.

[4] D.L. Fischman, M.B. Leon, D.S. Baim, R.A. Schatz, M.P. Savage, I. Penn, K. Detre, L. Veltri, D. Ricci, M. Nobuyoshi, M. Cleman, R. Heuser, D. Almond, P.S. Teirstein, R.D. Fish, A. Colombo, J. Brinker, J. Moses, A. Shaknovich, J. Hirshfeld, S. Bailey, S. Ellis, R. Rake, S. Goldberg, A Randomized Comparison of Coronary-Stent Placement and Balloon Angioplasty in the Treatment of Coronary Artery Disease, N Engl J Med. 331 (1994) 496–501. https://doi.org/10.1056/nejm199408253310802.

[5] G. Nakazawa, F. Otsuka, M. Nakano, M. Vorpahl, S.K. Yazdani, E. Ladich, F.D. Kolodgie, A. V Finn, R. Virmani, The Pathology of Neoatherosclerosis in Human Coronary Implants, J Am Coll Cardiol. 57 (2011) 1314. https://doi.org/10.1016/j.jacc.2011.01.011.

[6] K. Veerubhotla, C.H. Lee, Emerging Trends in Nanocarbon-Based Cardiovascular Applications, Adv Ther (Weinh). (2020) 1900208. https://doi.org/10.1002/adtp.201900208.

[7] H.O. Steinberg, B. Bayazeed, G. Hook, A. Johnson, J. Cronin, A.D. Baron, Endothelial Dysfunction Is Associated With Cholesterol Levels in the High Normal Range in Humans, Circulation. 96 (1997) 3287–3293. https://doi.org/10.1161/01.cir.96.10.3287.

[8] S. Jebari-Benslaiman, U. Galicia-García, A. Larrea-Sebal, J.R. Olaetxea, I. Alloza, K. Vandenbroeck, A. Benito-Vicente, C. Martín, Pathophysiology of Atherosclerosis, Int J Mol Sci. 23 (2022) 3346. https://doi.org/10.3390/ijms23063346.

[9] K. Sakakura, M. Nakano, F. Otsuka, E. Ladich, F.D. Kolodgie, R. Virmani, Pathophysiology of atherosclerosis plaque progression, Heart Lung Circ. 22 (2013) 399–411. https://doi.org/10.1016/j.hlc.2013.03.001.

[10]   D.-M. Zălar, C. Pop, E. Buzdugan, D. Todea, C.I. Mogoșan, The Atherosclerosis-Inflammation Relationship-A Pathophysiological Approach, Farmacia. 67 (2019) 6. https://doi.org/10.31925/farmacia.2019.6.2.

[11]   M.R. Bennett, S. Sinha, G.K. Owens, Vascular smooth muscle cells in atherosclerosis, Circ Res. 118 (2016) 692. https://doi.org/10.1161/circresaha.115.306361.

[12]   Y. Gui, H. Zheng, R.Y. Cao, Foam Cells in Atherosclerosis: Novel Insights Into Its Origins, Consequences, and Molecular Mechanisms, Front Cardiovasc Med. 9 (2022). https://doi.org/10.3389/fcvm.2022.845942.

[13]   J. Tang, Y. Liu, B. Zhu, Y. Su, X. Zhu, Preparation of paclitaxel/chitosan co-assembled core-shell nanofibers for drug-eluting stent, Appl Surf Sci. 393 (2017) 299–308. https://doi.org/10.1016/j.apsusc.2016.10.015.

[14]   A. Polimeni, T. Gori, Bioresorbable vascular scaffold: a step back thinking of the future, Adv Interv Cardiol. 14 (2018) 117–119. https://doi.org/10.5114/aic.2018.76401.

[15]   J.M. Seitz, M. Durisin, J. Goldman, J.W. Drelich, Recent advances in biodegradable metals for medical sutures: a critical review, Adv Healthc Mater. 4 (2015) 1915–1936. https://doi.org/10.1002/adhm.201500189.

[16]   P.C. Smits, S. Hofma, M. Togni, N. Vázquez, M. Valdés, V. Voudris, T. Slagboom, J.-J. Goy, A. Vuillomenet, A. Serra, R.T. Nouche, P. den Heijer, M. van der Ent, Abluminal biodegradable polymer biolimus-eluting stent versus durable polymer everolimus-eluting stent (COMPARE II): a randomised, controlled, non-inferiority trial, The Lancet. 381 (2013) 651–660. https://doi.org/10.1016/S0140-6736(12)61852-2.

[17]   N. Hong, G.H. Yang, J. Lee, G. Kim, 3D bioprinting and its in vivo applications, J Biomed Mater Res B Appl Biomater. 106 (2018) 444–459. https://doi.org/10.1002/jbm.b.33826.

[18]   C. Danek, Recent Advances and Future Challenges in the Additive Manufacturing of Hydrogels, Polymers (Basel). 14 (2022). https://doi.org/10.3390/polym14030494.

[19]   J. Gopinathan, I. Noh, Recent trends in bioinks for 3D printing, Biomater Res. 22 (2018) 1–15. https://doi.org/10.1186/S40824-018-0122-1.

[20]   A. Schwab, R. Levato, M. D'Este, S. Piluso, D. Eglin, J. Malda, Printability and Shape Fidelity of Bioinks in 3D Bioprinting, Chem Rev. 120 (2020) 11028–11055. https://doi.org/10.1021/acs.chemrev.0c00084.

[21]   S. Ji, M. Guvendiren, Recent Advances in Bioink Design for 3D Bioprinting of Tissues and Organs, Front Bioeng Biotechnol. 5 (2017). https://doi.org/10.3389/fbioe.2017.00023.

[22] S. Soleymani Eil Bakhtiari, H.R. Bakhsheshi-Rad, S. Karbasi, M. Razzaghi, M. Tavakoli, A.F. Ismail, S. Sharif, S. RamaKrishna, X. Chen, F. Berto, 3-Dimensional Printing of Hydrogel-Based Nanocomposites: A Comprehensive Review on the Technology Description, Properties, and Applications, Adv Eng Mater. 23 (2021) 2100477. https://doi.org/10.1002/adem.202100477.

[23] Y. He, F. Yang, H. Zhao, Q. Gao, B. Xia, J. Fu, Research on the printability of hydrogels in 3D bioprinting, Sci Rep. 6 (2016). https://doi.org/10.1038/srep29977.

[24] S.J. Lee, H.H. Jo, K.S. Lim, D. Lim, S. Lee, J.H. Lee, W.D. Kim, M.H. Jeong, J.Y. Lim, I.K. Kwon, Y. Jung, J.-K. Park, S.A. Park, Heparin coating on 3D printed poly (l-lactic acid) biodegradable cardiovascular stent via mild surface modification approach for coronary artery implantation, Chem. Eng. J. 378 (2019) 122116. https://doi.org/10.1016/j.cej.2019.122116.

[25] Y. Lee, C.H. Lee, Augmented reality for personalized nanomedicines, Biotechnol Adv. 36 (2018) 335–343. https://doi.org/10.1016/j.biotechadv.2017.12.008.

[26] Y. Lee, K. Veerubhotla, M.H. Jeong, C.H. Lee, Deep Learning in Personalization of Cardiovascular Stents, J Cardiovasc Pharmacol Ther. 25 (2020) 110–120. https://doi.org/10.1177/1074248419878405.

[27] A. El Sabbagh, M.F. Eleid, M. Al-Hijji, N.S. Anavekar, D.R. Holmes, V.T. Nkomo, G.S. Oderich, S.D. Cassivi, S.M. Said, C.S. Rihal, J.M. Matsumoto, T.A. Foley, The Various Applications of 3D Printing in Cardiovascular Diseases, Curr Cardiol Rep. 20 (2018) 47. https://doi.org/10.1007/s11886-018-0992-9.

[28] S.A. Park, S.J. Lee, K.S. Lim, I.H. Bae, J.H. Lee, W.D. Kim, M.H. Jeong, J.-K. Park, In vivo evaluation and characterization of a bio-absorbable drug-coated stent fabricated using a 3D-printing system, Mater Lett. 141 (2015) 355–358. https://doi.org/10.1016/j.matlet.2014.11.119.

[29] R. Van Lith, E. Baker, H. Ware, J. Yang, A.C. Farsheed, C. Sun, G. Ameer, 3D-Printing Strong High-Resolution Antioxidant Bioresorbable Vascular Stents, Adv Mater Technol. 1 (2016) 1600138. https://doi.org/10.1002/admt.201600138.

[30] M.S. Cabrera, B. Sanders, O.J.G.M. Goor, A. Driessen-Mol, C.W.J. Oomens, F.P.T. Baaijens, Computationally Designed 3D Printed Self-Expandable Polymer Stents with Biodegradation Capacity for Minimally Invasive Heart Valve Implantation: A Proof-of-Concept Study, 3D Print Addit Manuf. 4 (2017) 19–29. https://doi.org/10.1089/3dp.2016.0052.

[31] F. Mahmood, K. Owais, C. Taylor, M. Montealegre-Gallegos, W. Manning, R. Matyal, K.R. Khabbaz, Three-Dimensional Printing of Mitral Valve Using Echocardiographic Data, JACC Cardiovasc Imaging. 8 (2015) 227. https://doi.org/10.1016/j.jcmg.2014.06.020.

[32] M. Vukicevic, B. Mosadegh, J.K. Min, S.H. Little, Cardiac 3D Printing and its Future

Directions, JACC Cardiovasc Imaging. 10 (2017) 171.
https://doi.org/10.1016/j.jcmg.2016.12.001.

[33]   I. Valverde, Three-dimensional Printed Cardiac Models: Applications in the Field of
Medical Education, Cardiovascular Surgery, and Structural Heart Interventions, Rev
Esp Cardiol (Engl Ed). 70 (2017) 282–291. https://doi.org/10.1016/j.rec.2017.01.012.

[34]   D. Shi, K. Liu, X. Zhang, H. Liao, X. Chen, Applications of three-dimensional
printing technology in the cardiovascular field, Intern Emerg Med. 10 (2015) 769–780.
https://doi.org/10.1007/s11739-015-1282-9.

[35]   J.W. Stansbury, M.J. Idacavage, 3D printing with polymers: Challenges among
expanding options and opportunities, Dent Mater. 32 (2016) 54–64.
https://doi.org/10.1016/j.dental.2015.09.018.

[36]   X. Wang, M. Jiang, Z. Zhou, J. Gou, D. Hui, 3D printing of polymer matrix
composites: A review and prospective, Compos B Eng. 110 (2017) 442–458.
https://doi.org/10.1016/j.compositesb.2016.11.034.

[37]   N. Contessi Negrini, N. Celikkin, P. Tarsini, S. Farè, W. Święszkowski, Three-
dimensional printing of chemically crosslinked gelatin hydrogels for adipose tissue
engineering, Biofabrication. 12 (2020) 25001. https://doi.org/10.1088/1758-
5090/ab56f9.

[38]   T.-S. Jang, H.-D. Jung, H.M. Pan, H. Tun, S. Chen, J. Song, 3D printing of hydrogel
composite systems: Recent advances in technology for tissue engineering, Int J
Bioprint. 4 (2018). https://doi.org/10.18063/ijb.v4i1.126.

[39]   E. Prince, E. Kumacheva, Design and applications of man-made biomimetic fibrillar
hydrogels, Nat Rev Mater. 4 (2019) 99–115. https://doi.org/10.1038/s41578-018-
0077-9.

[40]   A.L. Rutz, K.E. Hyland, A.E. Jakus, W.R. Burghardt, R.N. Shah, A Multimaterial
Bioink Method for 3D Printing Tunable, Cell-Compatible Hydrogels, Adv Mater. 27
(2015) 1607–1614. https://doi.org/10.1002/adma.201405076.

[41]   H.N. Chan, Y. Shu, Q. Tian, Y. Chen, Y. Chen, H. Wu, Replicating 3D printed
structures into hydrogels, Mater Horiz. 3 (2016) 309–313.
https://doi.org/10.1039/c6mh00058d.

[42]   J.M. Lee, W.Y. Yeong, Design and Printing Strategies in 3D Bioprinting of Cell-
Hydrogels: A Review, Adv Healthc Mater. 5 (2016) 2856–2865.
https://doi.org/10.1002/adhm.201600435.

[43]   B. Oh, R.B. Melchert, C.H. Lee, Biomimicking Robust Hydrogel for the
Mesenchymal Stem Cell Carrier, Pharm Res. 32 (2015) 3213–3227.
https://doi.org/10.1007/s11095-015-1698-y.

[44]   Y. Liang, W. Liu, B. Han, C. Yang, Q. Ma, F. Song, Q. Bi, An in situ formed biodegradable hydrogel for reconstruction of the corneal endothelium, Colloids Surf B Biointerfaces. 82 (2011) 1–7. https://doi.org/10.1016/j.colsurfb.2010.07.043.

[45]   B. Sarker, D.G. Papageorgiou, R. Silva, T. Zehnder, F. Gul-E-Noor, M. Bertmer, J. Kaschta, K. Chrissafis, R. Detsch, A.R. Boccaccini, Fabrication of alginate–gelatin crosslinked hydrogel microcapsules and evaluation of the microstructure and physico-chemical properties, J Mater Chem B. 2 (2014) 1470–1482. https://doi.org/10.1039/c3tb21509a.

[46]   K.H. Chun, I.C. Kwon, Y.H. Kim, S.B. La, Y.T. Sohn, S.Y. Jeong, Preparation of sodium alginate microspheres containing hydrophilic β-lactam antibiotics, Arch Pharm Res. 19 (1996) 106–111. https://doi.org/10.1007/BF02976843.

[47]   F. Meng, W.E. Hennink, Z. Zhong, Reduction-sensitive polymers and bioconjugates for biomedical applications., Biomaterials. 30 (2009) 2180–2198. https://doi.org/10.1016/j.biomaterials.2009.01.026.

[48]   L. Li, C. Lu, L. Wang, M. Chen, J. White, X. Hao, K.M. McLean, H. Chen, T.C. Hughes, Gelatin-Based Photocurable Hydrogels for Corneal Wound Repair., ACS Appl Mater Interfaces. 10 (2018) 13283–13292. https://doi.org/10.1021/acsami.7b17054.

[49]   J. Griesser, G. Hetényi, A. Bernkop-Schnürch, Thiolated Hyaluronic Acid as Versatile Mucoadhesive Polymer: From the Chemistry Behind to Product Developments-What Are the Capabilities?, Polymers (Basel). 10 (2018) 243. https://doi.org/10.3390/polym10030243.

[50]   X. Zhang, W. Megone, T. Peijs, J.E. Gautrot, Functionalization of electrospun PLA fibers using amphiphilic block copolymers for use in carboxy-methyl-cellulose hydrogel composites, Nanocomposites. 6 (2020) 85–98. https://doi.org/10.1080/20550324.2020.1784600.

[51]   F. Olate-Moya, L. Arens, M. Wilhelm, M.A. Mateos-Timoneda, E. Engel, H. Palza, Chondroinductive Alginate-Based Hydrogels Having Graphene Oxide for 3D Printed Scaffold Fabrication, ACS Appl Mater Interfaces. 12 (2020) 4343–4357. https://doi.org/10.1021/acsami.9b22062.

[52]   C. Cha, S.R. Shin, X. Gao, N. Annabi, M.R. Dokmeci, X.S. Tang, A. Khademhosseini, Controlling mechanical properties of cell-laden hydrogels by covalent incorporation of graphene oxide, Small. 10 (2014) 514–523. https://doi.org/10.1002/smll.201302182.

[53]   M.E. Mackay, T.T. Dao, A. Tuteja, D.L. Ho, B. van Horn, H.-C. Kim, C.J. Hawker, Nanoscale effects leading to non-Einstein-like decrease in viscosity., Nat Mater. 2 (2003) 762–766. https://doi.org/10.1038/nmat999.

[54]   S. Jain, J.G.P. Goossens, G.W.M. Peters, M. van Duin, P.J. Lemstra, Strong decrease in viscosity of nanoparticle-filled polymer melts through selective adsorption, Soft

Matter. 4 (2008) 1848–1854. https://doi.org/10.1039/b802905a.

[55] A.B. Jindal, M.N. Wasnik, H.A. Nair, Synthesis of thiolated alginate and evaluation of mucoadhesiveness, cytotoxicity and release retardant properties, Indian J Pharm Sci. 72 (2010) 766–774. https://doi.org/10.4103/0250-474X.84590.

[56] E. des Ligneris, L.F. Dumée, L. Kong, Nanofibers for heavy metal ion adsorption: Correlating surface properties to adsorption performance, and strategies for ion selectivity and recovery, Environ Nanotechnol Monit Manag. 13 (2020) 100297. https://doi.org/https://doi.org/10.1016/j.enmm.2020.100297.

[57] M. Mohammadian, H. A.K., Systematic parameter study for nano-fiber fabrication via electrospinning process, Bulg Chem Commun. 46 (2014) 545–555.

[58] S. Palmieri, M. Pierpaoli, L. Riderelli, S. Qi, M. Letizia Ruello, Preparation and characterization of an electrospun PLA-cyclodextrins composite for simultaneous high-efficiency PM and VOC removal, J Compos Sci. 4 (2020). https://doi.org/10.3390/jcs4020079.

[59] Y. Li, C.T. Lim, M. Kotaki, Study on structural and mechanical properties of porous PLA nanofibers electrospun by channel-based electrospinning system, Polymer (Guildf). 56 (2015) 572–580. https://doi.org/10.1016/j.polymer.2014.10.073.

[60] K. Issaadi, A. Habi, Y. Grohens, I. Pillin, Maleic anhydride-grafted poly(lactic acid) as a compatibilizer in poly(lactic acid)/graphene oxide nanocomposites, Polym Bull. 73 (2016). https://doi.org/10.1007/s00289-015-1593-z.

[61] B.D. Coleman, H. Markovitz, W. Noll, Viscometric flows of non-Newtonian fluids; theory and experiment, Springer-Verlag, New York, 1966.

[62] H. Miyanaji, N. Momenzadeh, L. Yang, Effect of printing speed on quality of printed parts in Binder Jetting Process, Addit Manuf. 20 (2018) 1–10. https://doi.org/10.1016/j.addma.2017.12.008.

[63] Q. Gao, Y. He, J. Fu, A. Liu, L. Ma, Coaxial nozzle-assisted 3D bioprinting with built-in microchannels for nutrients delivery, Biomaterials. 61 (2015) 203–215. https://doi.org/10.1016/j.biomaterials.2015.05.031.

[64] K. Gnanasekaran, T. Heijmans, S. van Bennekom, H. Woldhuis, S. Wijnia, G. de With, H. Friedrich, 3D printing of CNT- and graphene-based conductive polymer nanocomposites by fused deposition modeling, Appl Mater Today. 9 (2017) 21–28. https://doi.org/10.1016/j.apmt.2017.04.003.

[65] Y. Han, C. Wei, J. Dong, Super-resolution electrohydrodynamic (EHD) 3D printing of micro-structures using phase-change inks, Manuf Lett. 2 (2014) 96–99. https://doi.org/10.1016/j.mfglet.2014.07.005.

[66] F. Yang, M. Zhang, B. Bhandari, Y. Liu, Investigation on lemon juice gel as food

material for 3D printing and optimization of printing parameters, LWT. 87 (2018) 67–76. https://doi.org/10.1016/j.lwt.2017.08.054.

[67] C.K. Kuo, P.X. Ma, Maintaining dimensions and mechanical properties of ionically crosslinked alginate hydrogel scaffolds in vitro, J Biomed Mater Res A. 84A (2008) 899–907. https://doi.org/10.1002/jbm.a.31375.

[68] G. Guan, C. Yu, M. Xing, Y. Wu, X. Hu, H. Wang, L. Wang, Hydrogel Small-Diameter Vascular Graft Reinforced with a Braided Fiber Strut with Improved Mechanical Properties, Polymers (Basel). 11 (2019) 810. https://doi.org/10.3390/polym11050810.

[69] W. Liu, Y. Dong, D. Liu, Y. Bai, X. Lu, Polylactic Acid (PLA)/Cellulose Nanowhiskers (CNWs) Composite Nanofibers: Microstructural and Properties Analysis, J Compos Sci. 2 (2018). https://doi.org/10.3390/jcs2010004.

[70] C. Wang, K. Wu, G.G. Scott, A.R. Akisanya, Q. Gan, Y. Zhou, A New Method for Pore Structure Quantification and Pore Network Extraction from SEM Images, Energy Fuels. 34 (2020) 82–94. https://doi.org/10.1021/acs.energyfuels.9b02522.

[71] C. Cheng, F. Helderman, D. Tempel, D. Segers, B. Hierck, R. Poelmann, A. van Tol, D.J. Duncker, D. Robbers-Visser, N.T.C. Ursem, R. van Haperen, J.J. Wentzel, F. Gijsen, A.F.W. van der Steen, R. de Crom, R. Krams, Large variations in absolute wall shear stress levels within one species and between species, Atherosclerosis. 195 (2007) 225–235. https://doi.org/10.1016/j.atherosclerosis.2006.11.019.

[72] J.-P. Nuutinen, C. Clerc, R. Reinikainen, P. Törmälä, Mechanical properties and in vitro degradation of bioabsorbable self-expanding braided stents., J Biomater Sci Polym Ed. 14 (2003) 255–266. https://doi.org/10.1163/156856203763572707.

[73] J. Charonko, S. Karri, J. Schmieg, S. Prabhu, P. Vlachos, In Vitro, Time-Resolved PIV Comparison of the Effect of Stent Design on Wall Shear Stress, Ann Biomed Eng. 37 (2009) 1310–1321. https://doi.org/10.1007/s10439-009-9697-y.

[74] S. Shinohara, T. Kihara, S. Sakai, M. Matsusaki, M. Akashi, M. Taya, J. Miyake, Fabrication of in vitro three-dimensional multilayered blood vessel model using human endothelial and smooth muscle cells and high-strength PEG hydrogel, J Biosci Bioeng. 116 (2013) 231–234. https://doi.org/10.1016/j.jbiosc.2013.02.013.

[75] T. Seo, L.G. Schachter, A.I. Barakat, Computational Study of Fluid Mechanical Disturbance Induced by Endovascular Stents, Ann Biomed Eng. 33 (2005) 444–456. https://doi.org/10.1007/s10439-005-2499-y.

[76] M. Matyash, F. Despang, C. Ikonomidou, M. Gelinsky, Swelling and Mechanical Properties of Alginate Hydrogels with Respect to Promotion of Neural Growth, Tissue Eng Part C Methods. 20 (2013) 401–411. https://doi.org/10.1089/ten.tec.2013.0252.

[77] B.K. Satheeshababu, I. Mohamed, Synthesis and Characterization of Sodium Alginate

Conjugate and Study of Effect of Conjugation on Drug Release from Matrix Tablet, Indian J Pharm Sci. 77 (2015) 579–585. https://doi.org/10.4103/0250-474x.169045.

[78]	B. Balakrishnan, A. Jayakrishnan, Self-cross-linking biopolymers as injectable in situ forming biodegradable scaffolds, Biomaterials. 26 (2005) 3941–3951. https://doi.org/10.1016/j.biomaterials.2004.10.005.

[79]	Y. Qian Zhang, F. Tian, J. Song Chen, Y. Dai Chen, Y. Zhou, B. Li, Q. Ma, Y. Zhang, Delayed reendothelialization with rapamycin is rescued by the addition of nicorandil in balloon-injured rat carotid arteries, Oncotarget; Vol 7, No 46. (2016). https://doi.org/10.18632/oncotarget.12444.

[80]	A. Schwab, R. Levato, M. D'Este, S. Piluso, D. Eglin, J. Malda, Printability and Shape Fidelity of Bioinks in 3D Bioprinting, Chem Rev. 120 (2020) 11028–11055. https://doi.org/10.1021/acs.chemrev.0c00084.

[81]	L. Zhang, G.-J. Zheng, Y.-T. Guo, L. Zhou, J. Du, H. He, Preparation of novel biodegradable pHEMA hydrogel for a tissue engineering scaffold by microwave-assisted polymerization, Asian Pac J Trop Med. 7 (2014) 136–140. https://doi.org/10.1016/S1995-7645(14)60009-2.

[82]	A.-I. Cocarta, R. Hobzova, M. Trchova, K. Svojgr, M. Kodetova, P. Pochop, J. Uhlik, J. Sirc, 2-Hydroxyethyl Methacrylate Hydrogels for Local Drug Delivery: Study of Topotecan and Vincristine Sorption/Desorption Kinetics and Polymer-Drug Interaction by ATR-FTIR Spectroscopy, Macromol Chem Phys. n/a (2021) 2100086. https://doi.org/10.1002/macp.202100086.

[83]	A. Ghamkhari, S. Abbaspour-Ravasjani, M. Talebi, H. Hamishehkar, M.R. Hamblin, Development of a graphene oxide-poly lactide nanocomposite as a Smart Drug Delivery System, Int J Biol Macromol. 169 (2021) 521–531. https://doi.org/10.1016/j.ijbiomac.2020.12.084.

[84]	M. Kazemi Ashtiani, M. Zandi, P. Shokrollahi, M. Ehsani, H. Baharvand, Surface modification of poly(2-hydroxyethyl methacrylate) hydrogel for contact lens application, Polym Adv Technol. 29 (2018) 1227–1233. https://doi.org/10.1002/pat.4233.

[85]	A.K. Rossos, C.N. Banti, A.G. Kalampounias, C. Papachristodoulou, K. Kordatos, P. Zoumpoulakis, T. Mavromoustakos, N. Kourkoumelis, S.K. Hadjikakou, pHEMA@AGMNA-1: A novel material for the development of antibacterial contact lens, Mater Sci Eng C. 111 (2020) 110770. https://doi.org/10.1016/j.msec.2020.110770.

[86]	M.F. Passos, N.M.S. Carvalho, A.A. Rodrigues, V.P. Bavaresco, A.L. Jardini, M.R.W. Maciel, R. Maciel Filho, PHEMA Hydrogels Obtained by Infrared Radiation for Cartilage Tissue Engineering, Int J Chem Eng. 2019 (2019) 4249581. https://doi.org/10.1155/2019/4249581.

[87]   H. Macková, Z. Plichta, H. Hlídková, O. Sedláček, R. Konefal, Z. Sadakbayeva, M. Dušková-Smrčková, D. Horák, Š. Kubinová, Reductively Degradable Poly(2-hydroxyethyl methacrylate) Hydrogels with Oriented Porosity for Tissue Engineering Applications, ACS Appl Mater Interfaces. 9 (2017) 10544–10553. https://doi.org/10.1021/acsami.7b01513.

[88]   O. Grytsenko, L. Dulebova, O. Suberlyak, V. Skorokhoda, E. Spišák, I. Gajdoš, Features of Structure and Properties of pHEMA-gr-PVP Block Copolymers, Obtained in the Presence of Fe2+, Materials. 13 (2020). https://doi.org/10.3390/ma13204580.

[89]   T.J. Hinton, A. Hudson, K. Pusch, A. Lee, A.W. Feinberg, 3D Printing PDMS Elastomer in a Hydrophilic Support Bath via Freeform Reversible Embedding, ACS Biomater Sci Eng. 2 (2016) 1781–1786. https://doi.org/10.1021/acsbiomaterials.6b00170.

[90]   V. Ozbolat, M. Dey, B. Ayan, I.T. Ozbolat, Extrusion-based printing of sacrificial Carbopol ink for fabrication of microfluidic devices, Biofabrication. 11 (2019) 34101. https://doi.org/10.1088/1758-5090/ab10ae.

[91]   L. Friedrich, M. Begley, Corner accuracy in direct ink writing with support material, Bioprinting. 19 (2020) e00086. https://doi.org/10.1016/j.bprint.2020.e00086.

[92]   A.M. Compaan, K. Song, Y. Huang, Gellan Fluid Gel as a Versatile Support Bath Material for Fluid Extrusion Bioprinting, ACS Appl Mater Interfaces. 11 (2019) 5714–5726. https://doi.org/10.1021/acsami.8b13792.

[93]   A. Lee, A.R. Hudson, D.J. Shiwarski, J.W. Tashman, T.J. Hinton, S. Yerneni, J.M. Bliley, P.G. Campbell, A.W. Feinberg, 3D bioprinting of collagen to rebuild components of the human heart, Science (1979). 365 (2019) 482–487. https://doi.org/10.1126/science.aav9051.

[94]   E. Mirdamadi, N. Muselimyan, P. Koti, H. Asfour, N. Sarvazyan, Agarose Slurry as a Support Medium for Bioprinting and Culturing Freestanding Cell-Laden Hydrogel Constructs, 3D Print Addit Manuf. 6 (2019) 158–164. https://doi.org/10.1089/3dp.2018.0175.

[95]   F. Afghah, M. Altunbek, C. Dikyol, B. Koc, Preparation and characterization of nanoclay-hydrogel composite support-bath for bioprinting of complex structures, Sci Rep. 10 (2020) 5257. https://doi.org/10.1038/s41598-020-61606-x.

[96]   H. Ding, R.C. Chang, Printability Study of Bioprinted Tubular Structures Using Liquid Hydrogel Precursors in a Support Bath, Appl Sci. 8 (2018). https://doi.org/10.3390/app8030403.

[97]   J.E. Rauschendorfer, K.M. Thien, M. Denz, S. Köster, F. Ehlers, P. Vana, Tuning the Mechanical Properties of Poly(Methyl Acrylate) via Surface-Functionalized Montmorillonite Nanosheets, Macromol Mater Eng. 306 (2021) 2000595. https://doi.org/10.1002/mame.202000595.

[98]   W. Huang, J. Shen, N. Li, M. Ye, Study on a new polymer/graphene oxide/clay double network hydrogel with improved response rate and mechanical properties, Polym Eng Sci. 55 (2015) 1361–1366. https://doi.org/10.1002/pen.24076.

[99]   S. Liu, A.K. Bastola, L. Li, A 3D Printable and Mechanically Robust Hydrogel Based on Alginate and Graphene Oxide, ACS Appl Mater Interfaces. 9 (2017) 41473–41481. https://doi.org/10.1021/acsami.7b13534.

[100] Z. Feng, Y. Li, C. Xin, D. Tang, W. Xiong, H. Zhang, Fabrication of Graphene-Reinforced Nanocomposites with Improved Fracture Toughness in Net Shape for Complex 3D Structures via Digital Light Processing, Carbon (Basel). 5 (2019). https://doi.org/10.3390/c5020025.

[101] V. Tolva, S. Mazzola, P. Zerbi, R. Casana, M. Albertini, L. Calvillo, F. Selmin, F. Cilurzo, A successful experimental model for intimal hyperplasia prevention using a resveratrol-delivering balloon, J Vasc Surg. 63 (2016) 788–794. https://doi.org/10.1016/j.jvs.2014.09.035.

[102] Z. Ungvari, Z. Orosz, A. Rivera, N. Labinskyy, Z. Xiangmin, S. Olson, A. Podlutsky, A. Csiszar, Resveratrol increases vascular oxidative stress resistance, Am J Physiol - Heart Circ Physiol. 292 (2007) H2417–H2424. https://doi.org/10.1152/ajpheart.01258.2006.

[103] J.J. Kleinedler, J.D. Foley, E.A. Orchard, T.R. Dugas, Novel nanocomposite stent coating releasing resveratrol and quercetin reduces neointimal hyperplasia and promotes re-endothelialization, J Control Release. 159 (2012) 27–33. https://doi.org/10.1016/j.jconrel.2012.01.008.

[104] A. Csiszar, K. Smith, N. Labinskyy, Z. Orosz, A. Rivera, Z. Ungvari, Resveratrol attenuates TNF-α-induced activation of coronary arterial endothelial cells: role of NF-κB inhibition, Am J Physiol - Heart Circ Physiol. 291 (2006) H1694–H1699. https://doi.org/10.1152/ajpheart.00340.2006.

[105] J. Zhang, J. Chen, J. Yang, C.W. Xu, P. Pu, J.W. Ding, H. Jiang, Resveratrol Attenuates Oxidative Stress Induced by Balloon Injury in the Rat Carotid Artery Through Actions on the ERK1/2 and NF-Kappa B Pathway, Cell Physiol Biochem. 31 (2013) 230–241. https://doi.org/10.1159/000343364.

[106] D.O. Kennedy, E.L. Wightman, J.L. Reay, G. Lietz, E.J. Okello, A. Wilde, C.F. Haskell, Effects of resveratrol on cerebral blood flow variables and cognitive performance in humans: a double-blind, placebo-controlled, crossover investigation., Am J Clin Nutr. 91 (2010) 1590–1597. https://doi.org/10.3945/ajcn.2009.28641.

[107] J.J. Kleinedler, I. Pjescic, K.K. Bullock, A. Khaliq, J.D. Foley, T.R. Dugas, Arterial pharmacokinetics of red wine polyphenols: implications for novel endovascular therapies targeting restenosis., J Pharm Sci. 101 (2012) 1917–1931. https://doi.org/10.1002/jps.23074.

[108] U. Förstermann, T. Münzel, Endothelial nitric oxide synthase in vascular disease: from marvel to menace., Circulation. 113 (2006) 1708–1714. https://doi.org/10.1161/circulationaha.105.602532.

[109] T. Wallerath, G. Deckert, T. Ternes, H. Anderson, H. Li, K. Witte, U. Förstermann, Resveratrol, a polyphenolic phytoalexin present in red wine, enhances expression and activity of endothelial nitric oxide synthase., Circulation. 106 (2002) 1652–1658. https://doi.org/10.1161/01.cir.0000029925.18593.5c.

[110] H. Li, N. Xia, S. Hasselwander, A. Daiber, Resveratrol and Vascular Function, Int J Mol Sci. 20 (2019). https://doi.org/10.3390/ijms20092155.

[111] J.M. Breuss, A.G. Atanasov, P. Uhrin, Resveratrol and Its Effects on the Vascular System, Int J Mol Sci. 20 (2019). https://doi.org/10.3390/ijms20071523.

[112] D. Moris, M. Spartalis, E. Spartalis, G.-S. Karachaliou, G.I. Karaolanis, G. Tsourouflis, D.I. Tsilimigras, E. Tzatzaki, S. Theocharis, The role of reactive oxygen species in the pathophysiology of cardiovascular diseases and the clinical significance of myocardial redox, Ann Transl Med. 5 (2017) 326. https://doi.org/10.21037/atm.2017.06.27.

[113] H. Cai, D.G. Harrison, Endothelial dysfunction in cardiovascular diseases: the role of oxidant stress, Circ Res. 87 (2000) 840–844. https://doi.org/10.1161/01.res.87.10.840.

[114] Z. Yang, Y. Yang, K. Xiong, X. Li, P. Qi, Q. Tu, F. Jing, Y. Weng, J. Wang, N. Huang, Nitric oxide producing coating mimicking endothelium function for multifunctional vascular stents, Biomaterials. 63 (2015) 80–92. https://doi.org/10.1016/j.biomaterials.2015.06.016.

[115] G. Acharya, Y. Lee, C.H. Lee, Optimization of Cardiovascular Stent against Restenosis: Factorial Design-Based Statistical Analysis of Polymer Coating Conditions, PLoS One. 7 (2012) e43100. https://doi.org/10.1371/journal.pone.0043100.

[116] A. Vashist, A. Kaushik, A. Ghosal, J. Bala, R. Nikkhah-Moshaie, W. A Wani, P. Manickam, M. Nair, Nanocomposite Hydrogels: Advances in Nanofillers Used for Nanomedicine, Gels. 4 (2018) 75. https://doi.org/10.3390/gels4030075.

[117] N.I. Zaaba, K.L. Foo, U. Hashim, S.J. Tan, W.-W. Liu, C.H. Voon, Synthesis of Graphene Oxide using Modified Hummers Method: Solvent Influence, Procedia Eng. 184 (2017) 469–477. https://doi.org/10.1016/j.proeng.2017.04.118.

[118] B. Oh, C.H. Lee, Development of Man-rGO for Targeted Eradication of Macrophage Ablation, Mol Pharm. 12 (2015) 3226–3236. https://doi.org/10.1021/acs.molpharmaceut.5b00181.

[119] K. Veerubhotla, Y. Lee, C.H. Lee, Parametric Optimization of 3D Printed Hydrogel-Based Cardiovascular Stent, Pharm Res. (2021). https://doi.org/10.1007/s11095-021-

03049-1.

[120] R. Schipani, D.R. Nolan, C. Lally, D.J. Kelly, Integrating finite element modelling and 3D printing to engineer biomimetic polymeric scaffolds for tissue engineering, Connect Tissue Res. 61 (2020) 174–189. https://doi.org/10.1080/03008207.2019.1656720.

[121] C.A. Schneider, W.S. Rasband, K.W. Eliceiri, NIH Image to ImageJ: 25 years of image analysis, Nature Methods 2012 9:7. 9 (2012) 671–675. https://doi.org/10.1038/nmeth.2089.

[122] E. Seo, S. Kumar, J. Lee, J. Jang, J.H. Park, M.C. Chang, I. Kwon, J.-S. Lee, Y. Huh, Modified hydrogels based on poly(2-hydroxyethyl methacrylate) (pHEMA) with higher surface wettability and mechanical properties, Macromol Res. 25 (2017) 704–711. https://doi.org/10.1007/s13233-017-5068-y.

[123] H. Wang, L. Wang, S. Meng, H. Lin, M. Correll, Z. Tong, Nanocomposite of Graphene Oxide Encapsulated in Polymethylmethacrylate (PMMA): Pre-Modification, Synthesis, and Latex Stability, J Compos Sci. 4 (2020). https://doi.org/10.3390/jcs4030118.

[124] G. Lorenzo, N. Zaritzky, A. Califano, Rheological analysis of emulsion-filled gels based on high acyl gellan gum, Food Hydrocoll. 30 (2013) 672–680. https://doi.org/10.1016/j.foodhyd.2012.08.014.

[125] P. R. Varges, C. M. Costa, B. S. Fonseca, M. F. Naccache, P.R. De Souza Mendes, Rheological Characterization of Carbopol® Dispersions in Water and in Water/Glycerol Solutions, Fluids. 4 (2019). https://doi.org/10.3390/fluids4010003.

[126] F. Yang, V. Tadepalli, B.J. Wiley, 3D Printing of a Double Network Hydrogel with a Compression Strength and Elastic Modulus Greater than those of Cartilage, ACS Biomater Sci Eng. 3 (2017) 863–869. https://doi.org/10.1021/acsbiomaterials.7b00094.

[127] L. Ferreira, M.M. Vidal, M.H. Gil, Evaluation of poly(2-hydroxyethyl methacrylate) gels as drug delivery systems at different pH values, Int J Pharm. 194 (2000) 169–180. https://doi.org/https://doi.org/10.1016/S0378-5173(99)00375-0.

[128] M. Rizwan, R. Yahya, A. Hassan, M. Yar, A.D. Azzahari, V. Selvanathan, F. Sonsudin, C.N. Aboulola, pH Sensitive Hydrogels in Drug Delivery: Brief History, Properties, Swelling, and Release Mechanism, Material Selection and Applications, Polymers (Basel). 9 (2017). https://doi.org/10.3390/polym9040137.

[129] M. Zare, A. Bigham, M. Zare, H. Luo, E. Rezvani Ghomi, S. Ramakrishna, pHEMA: An Overview for Biomedical Applications, Int J Mol Sci. 22 (2021). https://doi.org/10.3390/ijms22126376.

[130] A. Khosrozadeh, R. Rasuli, H. Hamzeloopak, Y. Abedini, Wettability and sound

absorption of graphene oxide doped polymer hydrogel, Sci Rep. 11 (2021) 15949. https://doi.org/10.1038/s41598-021-95641-z.

[131] J. Li, D.J. Mooney, Designing hydrogels for controlled drug delivery, Nat Rev Mater. 1 (2016) 16071. https://doi.org/10.1038/natrevmats.2016.71.

[132] J.C. Brown, T.E. Gerhardt, E. Kwon, Risk Factors For Coronary Artery Disease., in: Treasure Island (FL), 2022.

[133] X. Guo, Y. Guo, Z. Wang, B. Cao, C. Zheng, Z. Zeng, Y. Wei, Reducing the Damage of Ox-LDL/LOX-1 Pathway to Vascular Endothelial Barrier Can Inhibit Atherosclerosis, Oxid Med Cell Longev. 2022 (2022) 7541411. https://doi.org/10.1155/2022/7541411.

[134] L. Hang, Y. Peng, R. Xiang, X. Li, Z. Li, Ox-LDL Causes Endothelial Cell Injury Through ASK1/NLRP3-Mediated Inflammasome Activation via Endoplasmic Reticulum Stress, Drug Des Devel Ther. 14 (2020) 731–744. https://doi.org/10.2147/dddt.s231916.

[135] A.R. Fatkhullina, I.O. Peshkova, E.K. Koltsova, The Role of Cytokines in the Development of Atherosclerosis, Biochemistry (Mosc). 81 (2016) 1358–1370. https://doi.org/10.1134/S0006297916110134.

[136] M.L. Buckley, D.P. Ramji, The influence of dysfunctional signaling and lipid homeostasis in mediating the inflammatory responses during atherosclerosis, Biochim Biophys Acta - Mol Basis Dis. 1852 (2015) 1498–1510. https://doi.org/https://doi.org/10.1016/j.bbadis.2015.04.011.

[137] J.W.E. Moss, D.P. Ramji, Cytokines: Roles in atherosclerosis disease progression and potential therapeutic targets, Future Med Chem. 8 (2016) 1317–1330. https://doi.org/10.4155/fmc-2016-0072.

[138] O. Soehnlein, P. Libby, Targeting inflammation in atherosclerosis — from experimental insights to the clinic, Nat Rev Drug Discov. 20 (2021) 589–610. https://doi.org/10.1038/s41573-021-00198-1.

[139] T. Hu, C. Yang, S. Lin, Q. Yu, G. Wang, Biodegradable stents for coronary artery disease treatment: Recent advances and future perspectives, Mater Sci Eng C. 91 (2018) 163–178. https://doi.org/https://doi.org/10.1016/j.msec.2018.04.100.

[140] K. Veerubhotla, C.H. Lee, Design of biodegradable 3D-printed cardiovascular stent, Bioprinting. 26 (2022) e00204. https://doi.org/10.1016/j.bprint.2022.e00204.

[141] M. Zare, A. Bigham, M. Zare, H. Luo, E. Rezvani Ghomi, S. Ramakrishna, pHEMA: An Overview for Biomedical Applications, Int J Mol Sci. 22 (2021). https://doi.org/10.3390/ijms22126376.

[142] H. Massaro, L.F.A. Zambelli, A.A. de Britto, R.P. Vieira, A.P. Ligeiro-de-Oliveira,

D.C. Andia, M.T. Oliveira, A.F. Lima, Solvent and HEMA Increase Adhesive Toxicity and Cytokine Release from Dental Pulp Cells., Materials (Basel). 12 (2019). https://doi.org/10.3390/ma12172750.

[143] S.M. Oskui, G. Diamante, C. Liao, W. Shi, J. Gan, D. Schlenk, W.H. Grover, Assessing and Reducing the Toxicity of 3D-Printed Parts, Environ Sci Technol Lett. 3 (2016) 1–6. https://doi.org/10.1021/acs.estlett.5b00249.

[144] M. Bernard, E. Jubeli, M.D. Pungente, N. Yagoubi, Biocompatibility of polymer-based biomaterials and medical devices – regulations, in vitro screening and risk-management, Biomater Sci. 6 (2018) 2025–2053. https://doi.org/10.1039/C8BM00518D.

[145] N.-K. Hwangbo, N.-E. Nam, J.-H. Choi, J.-E. Kim, Effects of the Washing Time and Washing Solution on the Biocompatibility and Mechanical Properties of 3D Printed Dental Resin Materials, Polymers (Basel). 13 (2021). https://doi.org/10.3390/polym13244410.

[146] T.H. Lücking, F. Sambale, B. Schnaars, D. Bulnes-Abundis, S. Beutel, T. Scheper, 3D-printed individual labware in biosciences by rapid prototyping: In vitro biocompatibility and applications for eukaryotic cell cultures, Eng Life Sci. 15 (2015) 57–64. https://doi.org/https://doi.org/10.1002/elsc.201400094.

[147] F. Alifui-Segbaya, R. George, Biocompatibility of 3D-Printed Methacrylate for Hearing Devices, Inventions. 3 (2018) 52. https://doi.org/10.3390/inventions3030052.

[148] M. Walpitagama, M. Carve, A.M. Douek, C. Trestrail, Y. Bai, J. Kaslin, D. Wlodkowic, Additives migrating from 3D-printed plastic induce developmental toxicity and neuro-behavioural alterations in early life zebrafish (Danio rerio), Aquat Toxicol. 213 (2019) 105227. https://doi.org/https://doi.org/10.1016/j.aquatox.2019.105227.

[149] M. Carve, D. Wlodkowic, 3D-Printed Chips: Compatibility of Additive Manufacturing Photopolymeric Substrata with Biological Applications, Micromachines (Basel). 9 (2018) 91. https://doi.org/10.3390/mi9020091.

[150] T.S.P. Rothenbücher, J. Ledin, D. Gibbs, H. Engqvist, C. Persson, G. Hulsart-Billström, Zebrafish embryo as a replacement model for initial biocompatibility studies of biomaterials and drug delivery systems, Acta Biomater. 100 (2019) 235–243. https://doi.org/10.1016/j.actbio.2019.09.038.

[151] C. Chakraborty, A.R. Sharma, G. Sharma, S.-S. Lee, Zebrafish: A complete animal model to enumerate the nanoparticle toxicity, J Nanobiotechnology. 14 (2016) 65. https://doi.org/10.1186/s12951-016-0217-6.

[152] A.J. Hill, H. Teraoka, W. Heideman, R.E. Peterson, Zebrafish as a Model Vertebrate for Investigating Chemical Toxicity, Toxicol Sci. 86 (2005) 6–19. https://doi.org/10.1093/toxsci/kfi110.

[153] A.M. Chahardehi, H. Arsad, V. Lim, Zebrafish as a Successful Animal Model for Screening Toxicity of Medicinal Plants, Plants (Basel). 9 (2020) 1345. https://doi.org/10.3390/plants9101345.

[154] C. Hart, C.M. Didier, F. Sommerhage, S. Rajaraman, Biocompatibility of Blank, Post-Processed and Coated 3D Printed Resin Structures with Electrogenic Cells, Biosensors (Basel). 10 (2020) 152. https://doi.org/10.3390/bios10110152.

[155] I.G. Siller, A. Enders, T. Steinwedel, N.-M. Epping, M. Kirsch, A. Lavrentieva, T. Scheper, J. Bahnemann, Real-Time Live-Cell Imaging Technology Enables High-Throughput Screening to Verify in Vitro Biocompatibility of 3D Printed Materials, Materials. 12 (2019). https://doi.org/10.3390/ma12132125.

[156] L.-L. Yang, G.-Q. Wang, L.-M. Yang, Z.-B. Huang, W.-Q. Zhang, L.-Z. Yu, Endotoxin molecule lipopolysaccharide-induced zebrafish inflammation model: a novel screening method for anti-inflammatory drugs, Molecules. 19 (2014) 2390–2409. https://doi.org/10.3390/molecules19022390.

[157] C.B. Kimmel, W.W. Ballard, S.R. Kimmel, B. Ullmann, T.F. Schilling, Stages of embryonic development of the zebrafish., Dev Dyn. 203 (1995) 253–310. https://doi.org/10.1002/aja.1002030302.

[158] M. Westerfield, The Zebrafish Book. A Guide for the Laboratory Use of Zebrafish (Danio rerio), 4th ed., University of Oregon Press, Eugene, 2000.

[159] J. Schindelin, I. Arganda-Carreras, E. Frise, V. Kaynig, M. Longair, T. Pietzsch, S. Preibisch, C. Rueden, S. Saalfeld, B. Schmid, J.-Y. Tinevez, D.J. White, V. Hartenstein, K. Eliceiri, P. Tomancak, A. Cardona, Fiji: an open-source platform for biological-image analysis, Nat Methods. 9 (2012) 676–682. https://doi.org/10.1038/nmeth.2019.

[160] Y. Liu, X. Chen, J. Li, Resveratrol protects against oxidized low-density lipoprotein-induced human umbilical vein endothelial cell apoptosis via inhibition of mitochondrial-derived oxidative stress, Mol Med Rep. 15 (2017) 2457–2464. https://doi.org/10.3892/mmr.2017.6304.

[161] Y. Zhang, X. Cao, W. Zhu, Z. Liu, H. Liu, Y. Zhou, Y. Cao, C. Liu, Y. Xie, Resveratrol Enhances Autophagic Flux and Promotes Ox-LDL Degradation in HUVECs via Upregulation of SIRT1, Oxid Med Cell Longev. 2016 (2016) 7589813. https://doi.org/10.1155/2016/7589813.

[162] Y. Zhang, J. Sun, X. Yu, L. Shi, W. Du, L. Hu, C. Liu, Y. Cao, SIRT1 regulates accumulation of oxidized LDL in HUVEC via the autophagy-lysosomal pathway, Prostaglandins Other Lipid Mediat. 122 (2016) 37–44. https://doi.org/10.1016/j.prostaglandins.2015.12.005.

[163] J. Chen, Y. Liu, Y. Liu, J. Peng, Resveratrol protects against ox-LDL-induced endothelial dysfunction in atherosclerosis via depending on circ_0091822/miR-106b-

5p-mediated upregulation of TLR4, Immunopharmacol Immunotoxicol. (2022) 1–10. https://doi.org/10.1080/08923973.2022.2093740.

[164] S.H. Tsai, S.Y. Lin-Shiau, J.K. Lin, Suppression of nitric oxide synthase and the down-regulation of the activation of NFkappaB in macrophages by resveratrol, Br J Pharmacol. 126 (1999) 673–680. https://doi.org/10.1038/sj.bjp.0702357.

[165] Y.S. Lin, C.F. Lin, H.Y. Lei, H.S. Liu, T.M. Yeh, S.H. Chen, C.C. Liu, Antibody-Mediated Endothelial Cell Damage Via Nitric Oxide, Curr Pharm Des. 10 (2005) 213–221. https://doi.org/10.2174/1381612043453469.

[166] C.A. Adiabouah Achy-Brou, B. Billack, A comparative assessment of the cytotoxicity and nitric oxide reducing ability of resveratrol, pterostilbene and piceatannol in transformed and normal mouse macrophages, Drug Chem Toxicol. 40 (2017) 36–46. https://doi.org/10.3109/01480545.2016.1169542.

[167] A.A. Qureshi, X.Q. Guan, J.C. Reis, C.J. Papasian, S. Jabre, D.C. Morrison, N. Qureshi, Inhibition of nitric oxide and inflammatory cytokines in LPS-stimulated murine macrophages by resveratrol, a potent proteasome inhibitor, Lipids Health Dis. 11 (2012) 76. https://doi.org/10.1186/1476-511X-11-76.

[168] C.B. Kimmel, W.W. Ballard, S.R. Kimmel, B. Ullmann, T.F. Schilling, Stages of embryonic development of the zebrafish, Dev Dyn. 203 (1995) 253–310. https://doi.org/10.1002/AJA.1002030302.

[169] J. Bakkers, Zebrafish as a model to study cardiac development and human cardiac disease, Cardiovasc Res. 91 (2011) 279–288. https://doi.org/10.1093/cvr/cvr098.

[170] J.M. González-Rosa, Zebrafish Models of Cardiac Disease: From Fortuitous Mutants to Precision Medicine, Circ Res. 130 (2022) 1803–1826. https://doi.org/10.1161/circresaha.122.320396.

[171] D. Pardal, M. Caro, I. Tueros, A. Barranco, V. Navarro, Resveratrol and Piceid Metabolites and Their Fat-Reduction Effects in Zebrafish Larvae, Zebrafish. 11 (2013) 32–40. https://doi.org/10.1089/zeb.2013.0893.

[172] S. Steven, K. Frenis, M. Oelze, S. Kalinovic, M. Kuntic, M.T.B. Jimenez, K. Vujacic-Mirski, J. Helmstädter, S. Kröller-Schön, T. Münzel, A. Daiber, Vascular Inflammation and Oxidative Stress: Major Triggers for Cardiovascular Disease, Oxid Med Cell Longev. 2019 (2019). https://doi.org/10.1155/2019/7092151.

[173] K. Somszor, O. Bas, F. Karimi, T. Shabab, N.T. Saidy, A.J. O'Connor, A. v. Ellis, D. Hutmacher, D.E. Heath, Personalized, Mechanically Strong, and Biodegradable Coronary Artery Stents via Melt Electrowriting, ACS Macro Lett. 9 (2020) 1732–1739. https://doi.org/10.1021/acsmacrolett.0c00644.

[174] A. Kalra, H. Rehman, S. Khera, B. Thyagarajan, D.L. Bhatt, N.S. Kleiman, R.W. Yeh, New-Generation Coronary Stents: Current Data and Future Directions, Curr

Atheroscler Rep. 19 (2017) 1–10. https://doi.org/10.1007/s11883-017-0654-1.

VITA

Krishna Veerubhotla is a PhD candidate in Pharmaceutical Sciences at the School of Pharmacy (SOP), University of Missouri-Kansas City (UMKC). Prior to this, he received his bachelor's degree in pharmacy from Acharya Nagarjuna University, India. The knowledge gained about formulation of various dosage forms during practical sessions and academic project at the undergraduate level augmented his interest in pharmaceutical research. After graduation, he joined Granules India as a project assistant and worked on pre-formulation aspects, formulation development and analytical testing of various oral solid dosage forms.

Subsequently, he immigrated to South Africa to pursue postgraduate research at Rhodes University (RU), where he was awarded the prestigious and highly competitive National Research Foundation (NRF) scholarship to conduct research on an age-appropriate formulation using the principles of quality by design (QbD). It is noteworthy that only 4% of the NRF scholarships are granted to applicants from non-African countries.

Krishna's doctoral research focuses on the design, development, and characterization of novel biomaterials for cardiovascular applications. His seminal work has been published in various peer-reviewed journals including Advanced Therapeutics, Pharmaceutical Research, and Bioprinting. He has earned several scholarships and accolades such as SOP Scholarships, School of Graduate Studies Travel Grants, Best Abstract Award at the American Association of Pharmaceutical Scientists (AAPS) PharmSci 360 Conference, and Best Graduate Student Award from the American Association of Indian Pharmaceutical Scientists (AAiPS).

COPYRIGHT CLEARANCE

JOHN WILEY AND SONS LICENSE
TERMS AND CONDITIONS

This Agreement between Mr. Hari Mani Krishna Veerubhotla ("You") and John Wiley and Sons ("John Wiley and Sons") consists of your license details and the terms and conditions provided by John Wiley and Sons and Copyright Clearance Center.

License Number	5427301065014
License date	Nov 13, 2022
Licensed Content Publisher	John Wiley and Sons
Licensed Content Publication	ADVANCED THERAPEUTICS
Licensed Content Title	Emerging Trends in Nanocarbon-Based Cardiovascular Applications
Licensed Content Author	Chi H. Lee, Krishna Veerubhotla
Licensed Content Date	Apr 17, 2020
Licensed Content Volume	3
Licensed Content Issue	7
Licensed Content Pages	14
Type of Use	Dissertation/Thesis
Requestor type	Author of this Wiley article
Format	Print and electronic
Portion	Full article
Will you be translating?	No
Title	Development and Evaluation of 3D-Printed Cardiovascular Stents
Institution name	University of Missouri-Kansas City
Expected presentation date	Nov 2022
Requestor Location	Mr. Hari Mani Krishna Veerubhotla 3403 Campbell Street
	Kansas City, MO 64109 United States Attn: Mr. Hari Mani Krishna Veerubhotla
Publisher Tax ID	EU826007151
Total	**0.00 USD**
Terms and Conditions	

CCC
RightsLink

🏠 Home | ❓ Help ⌄ | ✉ Email Support | 👤 Hari Mani Krishna Veerubhotla ⌄

Design of biodegradable 3D-printed cardiovascular stent

Author: Krishna Veerubhotla,Chi H. Lee

Publication: Bioprinting

Publisher: Elsevier

Date: June 2022

Published by Elsevier B.V.

Journal Author Rights

Please note that, as the author of this Elsevier article, you retain the right to include it in a thesis or dissertation, provided it is not published commercially. Permission is not required, but please ensure that you reference the journal as the original source. For more information on this and on your other retained rights, please visit: https://www.elsevier.com/about/our-business/policies/copyright#Author-rights

BACK   CLOSE WINDOW